Doctoral Dissertation
Doctoral Program in Chemical Engineering (38^{th}cycle)

Enhancing Thermal Efficiency Assessment in High-Altitude Footwear

By

Eleonora Bianca

******

Supervisor(s):
Prof. A. Ferri, Supervisor
Prof. M. Vanni, Co-Supervisor
Prof. A. Buffo, Co-Supervisor

Doctoral Examination Committee:
Prof. J. Waller, Referee, Mid Sweden University
Prof. S. Schwanitz, Referee, Chemnitz University of Technology

Politecnico di Torino
2026

Declaration

I hereby declare that, the contents and organization of this dissertation constitute my own original work and does not compromise in any way the rights of third parties, including those relating to the security of personal data.

The doctoral thesis was written at the end of the doctoral program, funded by PNRR Mission 4, Component 2 “Dalla Ricerca all’Impresa” – Investimento 3.3 “Introduzione di dottorati innovativi che rispondono ai fabbisogni di innovazione delle imprese e promuovono l’assunzione dei ricercatori dalle imprese”, through Ministerial Decree no. 352 of 9 April 2022.

Eleonora Bianca
2026

* This dissertation is presented in partial fulfillment of the requirements for **Ph.D. degree** in the Graduate School of Politecnico di Torino (ScuDo).

Finanziato dall'Unione europea
NextGenerationEU

Ministero dell'Università e della Ricerca

Italiadomani
PIANO NAZIONALE DI RIPRESA E RESILIENZA

A Dike e Baloo, entrambi al giusto spaziosi

Abstract

High-altitude footwear can be more appropriately classified as Personal Protective Equipment (PPE) rather than simply sports equipment. However, there are currently no strict or reliable standards available to accurately assess the thermal performance of cold-protective footwear, apart from the general guidelines defined in ISO 20344:2021. Another possible method for determining footwear insulation is the thermal manikin test (ISO 15831:2004). Although this procedure provides precise and reproducible results, it is expensive and not easily applicable in industrial contexts. Moreover, both of these tests rely on the physical production of the samples that should be tested.

This thesis aims to develop an improved methodology for assessing the thermal performance of cold-protective footwear. To achieve this, three complementary approaches were adopted: experimental, physics-based, and data-driven.

In the experimental approach, the study followed the five-level testing framework, focusing on the first three levels (namely, laboratory testing). This includes apparative tests and in-vivo experiments.

The apparative phase involved characterising the thermal and physical properties of the materials and garments according to ISO 9920:2007 (thermal resistance, R_{cT}), ISO 5084:1997 (thickness), and ISO 15831:2004 (thermal insulation of clothing ensembles). The in-vivo tests, conducted in controlled cold environments, focused on understanding human thermophysiological responses. A key finding was the confirmation of big toe temperature as a reliable indicator of foot thermal comfort, consistent with previous literature, and the identification of a critical safety threshold of 15 °C to prevent frostbite risk. Moreover, a strong zero-lag correlation was observed between mean skin temperature and big toe temperature, enabling the latter to be predicted from the former. These results also contributed to the creation of a comprehensive dataset of body temperature time series under varying ambient, activity, and insulation conditions, an essential foundation for subsequent modelling

efforts.

Building on this knowledge, the physics-based approach focused on replicating and validating one of the experimental test protocols through a realistic digital twin of a boot provided by the industrial partner. The model was divided into distinct regions reproducing the actual materials and thicknesses, and was validated against experimental R_{cT} data from the manikin tests. A user-defined material database was developed to ensure accurate input parameters. This approach enabled the virtual estimation of a prototype's R_{cT} value prior to physical production, thus providing the company with a valuable tool to assess footwear thermal performance based on material composition and design.

Finally, the data-driven approach used the dataset obtained from the human tests to develop predictive models of peripheral temperature dynamics. Two different algorithms were compared: a statistical autoregressive model (SARIMAX) and a neural network architecture employing Long Short-Term Memory (LSTM) layers. Both were trained using categorical inputs such as ambient temperature, activity level, and footwear insulation (derived from Computational Fluid Dynamics results or from the physical thermal manikin tests R_{cT} estimation or from the physical thermal manikin tests). The models aimed to predict big toe temperature, used as an indicator of foot thermal comfort, over time. Specifically, the time in minutes taken by the big toe temperature curve to reach 15 °C was defined as the Duration of Safe Exposure, forming the second evaluation parameter for footwear thermal properties. The LSTM-based model demonstrated higher accuracy and generalisation capability, highlighting the potential of integrating experimental, computational, and data-driven methods into a unified framework for footwear thermal performance assessment.

Contents

List of Figures

List of Tables

Nomenclature

Abbreviations

AH	Absolute humidity
AIC	Akaike Information Criterion
BMI	Body Mass Index
BSA	Body Surface Area
CFD	Computational Fluid Dynamics
CIVC	Cold-Induced Vasoconstriction
CIVD	Cold-Induced Vasodilation
DL	Deep Learning
DSE	Duration of Safe Exposure
DTC	Differentiable Threshold-Crossing
HR	Heart rate
IREQ	Insulation Required
LSTMs	Long Short-Term Memory networks
MAE	Mean Absolute Error
MET	Metabolic Equivalent of Task, defined as $58\,\mathrm{W} \cdot \mathrm{m}^{-2}$
ML	Machine Learning

MR	Metabolic rate
MWC	Maximum Work Capacity
RH	Relative humidity
RM	Relationship between heart rate and metabolic rate (slope factor in the HR-based method)
RMSE	Root Mean Square Error
RNNs	Recurrent Neural Networks
SARIMAX	Seasonal AutoRegressive Integrated Moving Average with eXogenous variables
TNZ	Thermoneutral Zone

Symbols

ε	Surface emissivity $[-]$
η_{app}	Apparent evaporative efficiency, defined as the ratio between apparent and mass-based evaporative heat losses $[-]$
λ	Latent heat of evaporation $[\mathrm{J \cdot g^{-1}}]$
WVA	Water vapour accumulation rate $[\mathrm{g \cdot h^{-1}}]$
ρ	Density $[\mathrm{kg \cdot m^{-3}}]$
σ	Stefan–Boltzmann constant $[\mathrm{W \cdot m^{-2} \cdot K^{-4}}]$
A_{DU}	DuBois body surface area $[\mathrm{m^2}]$
Age	Age [yr]
C	Convective heat flow $[\mathrm{W \cdot m^{-2}}]$
C	Mass concentration $[\mathrm{kg \cdot m^{-3}}]$
c	Specific heat capacity $[\mathrm{J \cdot kg^{-1} \cdot K^{-1}}]$
D	Mass diffusion coefficient $[\mathrm{m^2 \cdot s^{-1}}]$
D	Seasonal differencing order $[-]$
E	Evaporative heat loss from the skin $[\mathrm{W \cdot m^{-2}}]$
E_{app}	Apparent evaporative heat loss, computed as $H_{\text{wet}} - H_{\text{dry}}$ $[\mathrm{W \cdot m^{-2}}]$
E_{mass}	Evaporative heat flux derived from mass loss $[\mathrm{W \cdot m^{-2}}]$
$E_{\text{RES}}, C_{\text{RES}}$	Respiratory evaporative and convective heat losses $[\mathrm{W \cdot m^{-2}}]$
G	Walking gradient (slope) $[-]$
H	Net heat flow rate other than diffusion $[\mathrm{W \cdot m^{-3}}]$
h_{c}	Convective heat transfer coefficient $[\mathrm{W \cdot m^{-2} \cdot K^{-1}}]$
H_{dry}	Dry heat loss from the thermal zone $[\mathrm{W \cdot m^{-2}}]$

HR_0	Resting heart rate [bpm]
$HR_{\max}$	Maximum heart rate [bpm]
HR_m	Measured heart rate during activity [bpm]
I_{cl}	Clothing insulation [clo]
i_{m}	Moisture permeability index, defined as the ratio between total thermal and evaporative resistances [$-$]
J	Mass flux [$\mathrm{kg \cdot m^{-2} \cdot s^{-1}}$]
K	Conductive heat flow [$\mathrm{W \cdot m^{-2}}$]
k	Thermal conductivity [$\mathrm{W \cdot m^{-1} \cdot K^{-1}}$]
L	External load [kg]
M	Metabolic rate [$\mathrm{W \cdot m^{-2}}$]
M	Metabolic rate [$\mathrm{W \cdot m^{-2}}$]
M_0	Baseline metabolic rate [$\mathrm{W \cdot m^{-2}}$]
M_{men}	Metabolic rate for men [$\mathrm{W \cdot m^{-2}}$]
M_{women}	Metabolic rate for women [$\mathrm{W \cdot m^{-2}}$]
M_m	Metabolic rate estimated from heart rate [$\mathrm{W \cdot m^{-2}}$]
MWC	Maximum work capacity [$\mathrm{W \cdot m^{-2}}$]
N_{rungs}	Number of ladder rungs negotiated [as defined in the adopted formulation]
Nu	Nusselt number [$-$]
P	Seasonal autoregressive order [$-$]
Q	Seasonal moving average order [$-$]
Q_{D}	Dry heat flux supplied to the manikin [$\mathrm{W \cdot m^{-2}}$]
Q_{E}	Evaporative heat flux [$\mathrm{W \cdot m^{-2}}$]

Q_r	Radiative heat flux [$\mathrm{W \cdot m^{-2}}$]
$Q_\mathrm{W+D}$	Combined wet and dry heat flux supplied to the manikin [$\mathrm{W \cdot m^{-2}}$]
R	Radiative heat flow [$\mathrm{W \cdot m^{-2}}$]
R_cT	Total thermal resistance [$\mathrm{m^2 \cdot K \cdot W^{-1}}$]
$R_\mathrm{eT,\,heat\,loss}$	Total evaporative resistance derived from heat loss [$\mathrm{kPa \cdot m^2 \cdot W^{-1}}$]
$R_\mathrm{eT,\,mass\,loss}$	Total evaporative resistance derived from mass loss [$\mathrm{kPa \cdot m^2 \cdot W^{-1}}$]
Re	Reynolds number [$-$]
RM	Slope factor relating heart rate and metabolic rate in the HR- based method [$\mathrm{bpm\,(W \cdot m^{-2})^{-1}}$]
S	Rate of body heat storage [$\mathrm{W \cdot m^{-2}}$]
s	Length of the seasonal period [min]
T	Temperature [K]
T_sk	Mean skin temperature [°C]
U_D	Dry energy supplied to the manikin over the observation period [$\mathrm{kJ \cdot m^{-2}}$]
$U_\mathrm{E+K+C}$	Energy contribution due to evaporative, conductive, and condensation heat losses [$\mathrm{kJ \cdot m^{-2}}$]
U_E	Energy associated with evaporative heat loss [$\mathrm{kJ \cdot m^{-2}}$]
$U_\mathrm{K+C}$	Energy associated with conductive heat loss and condensation effects [$\mathrm{kJ \cdot m^{-2}}$]
$U_\mathrm{W+D}$	Total energy supplied under wet and dry conditions [$\mathrm{kJ \cdot m^{-2}}$]
v_w	Walking speed [as defined in the adopted formulation]
W	Effective mechanical power [$\mathrm{W \cdot m^{-2}}$]
W_bl	Body mass used in the HR-based formulation [kg]
W_b	Body mass [kg]

Chapter 1

Introduction

1.1 Background and context

1.1.1 Human thermoregulation

From the glossary of thermophysiological terms, the thermoneutral zone (TNZ) is defined as “the range of ambient temperature at which temperature regulation is achieved only by the control of sensible (dry) heat loss, i.e. without regulatory changes in metabolic heat production or evaporative heat loss” (J Bligh, 1973). This definition focuses exclusively on autonomous thermoregulation and neglects the contribution of behavioural thermoregulation (Kingma et al., 2014). Thermal comfort is the state in which body temperatures remain within narrow limits, skin moisture is low, and the physiological effort required for thermoregulation is minimal. Indeed, according to its definition, thermal comfort is "*a condition of mind which expresses satisfaction with the surrounding environment*" (ASHRAE, 2023). However, thermal comfort also results from behavioural adjustments (such as changing clothes, performing activities, changing posture, changing location, or adapting the environment), aimed at avoiding the feeling of discomfort.

The first attempts to characterise heat exchange and thermoregulatory balance in humans date back to the late 1770s, when British military physiologist Sir Charles Blagden conducted descriptive studies on humans, dogs, and even beef steaks in heated rooms (Blagden, 1775). Remarkably, these early physiological investigations preceded the formal development of thermodynamic theory, reflecting the fundamental importance of understanding heat exchange in living organisms. Later, with the establishment of thermodynamic laws, it became possible to quantify heat transfer processes more precisely. In particular, Fourier's law (Fourier, 1822) provides a mathematical framework for describing heat dynamics in solids, often simplified as:

$$\rho \cdot \mathrm{c} \cdot \frac{\partial \mathrm{T}}{\partial \mathrm{t}} = \nabla \mathrm{k} \nabla \mathrm{T} + \mathrm{H} \tag{1.1}$$

where:
ρ is the density expressed in $\mathrm{kg} \cdot \mathrm{m}^{-3}$;
c is the specific heat expressed in $\mathrm{J} \cdot \mathrm{K}^{-1} \cdot \mathrm{kg}^{-1}$;
k is the heat conductance expressed in $\mathrm{W} \cdot \mathrm{m}^{-1} \cdot \mathrm{K}^{-1}$;
T is the temperature expressed in K;
t is the time expressed in hours;
H is the heat net flow rate other than diffusion in $\mathrm{W} \cdot \mathrm{m}^{-3}$.

The first formal description of human-environment heat exchange was provided by Lefevre in 1911 (Lefevre, 1911), who modelled the human body as a sphere with an internal core exchanging heat through a surrounding shell. Later, in 1934, Burton (Burton, 1934) approximated the human body as a cylinder and applied Fourier's law to describe heat exchange mathematically, laying the foundation for what is widely considered the first conceptual model of human thermal regulation. The human body is a homeothermic organism capable of maintaining thermal balance even in harsh and extreme environments. Physical activity is the most obvious strategy the body uses to generate heat, but it also requires efficient heat dissipation mechanisms. Insufficient heat dissipation leads to overheating (hyperthermia), while excessive heat dissipation leads to cooling (hypothermia). According to Hardy (Hardy et al., 1952), skin temperatures above 45 °C or below 18 °C trigger pain. During sedentary activity, the skin temperatures associated with well-being are typically 33–34 °C and decrease with increasing activity (Fanger, 1967).

Most of the heat produced by the body is exchanged with the environment via the skin. For this reason, the reference unit for metabolic heat production at rest is expressed per unit of body surface area: 58 $\mathrm{W} \cdot \mathrm{m}^{-2}$ (defined as 1 met).[1] This unit has become a standard reference in human thermal comfort studies.

---

[1] This value is based on an average European male with a body surface area of approximately 1.8 m^2 (ASHRAE, 2017). There may be differences between ethnic, geographical, and gender groups.

As extensively described in the literature (Parsons, 2014), the heat exchanged between the human body and the environment can be expressed through the General Heat Balance Equation:

$$\mathrm{M} - \mathrm{W} = \mathrm{E}_{\mathrm{RES}} + \mathrm{C}_{\mathrm{RES}} + \mathrm{E} + \mathrm{K} + \mathrm{C} + \mathrm{R} + \mathrm{S} \tag{1.2}$$

The left-hand side of the equation represents the internal heat production, given by the metabolic rate (M) minus the effective mechanical work (W). The right-hand side represents the sum of the heat exchanges occurring through respiration and at the skin surface, together with the energy storage in the body. Specifically:

M Metabolic rate, in $\mathrm{W} \cdot \mathrm{m}^{-2}$.
W Effective mechanical power, in $\mathrm{W} \cdot \mathrm{m}^{-2}$.
E_{RES}, C_{RES} Respiratory evaporative and convective heat losses, in $\mathrm{W} \cdot \mathrm{m}^{-2}$.
E Evaporative heat loss from the skin, in $\mathrm{W} \cdot \mathrm{m}^{-2}$.
K Conductive heat flow, in $\mathrm{W} \cdot \mathrm{m}^{-2}$.
C Convective heat flow, in $\mathrm{W} \cdot \mathrm{m}^{-2}$.
R Radiative heat flow, in $\mathrm{W} \cdot \mathrm{m}^{-2}$.
S Rate of body heat storage, in $\mathrm{W} \cdot \mathrm{m}^{-2}$.

As described in detail by Hensel (Hensel and Schafer, 1984), the hypothalamus acts as a control centre for body temperature. This small but important brain region integrates thermal inputs and coordinates physiological responses, while also playing a role in circadian cycles and other homeostatic drives. Autonomic mechanisms of thermoregulation include vasodilation, vasoconstriction, sweating, and shivering, while behavioural thermoregulation relies on voluntary actions to maintain thermal equilibrium. Thanks to these two levels of regulation, humans are able to maintain their homeostasis under a variety of environmental conditions.

1.1.2 Thermoregulation in extreme environments

The internal equilibrium of the body is known as homeostasis. In some cases, the autonomic mechanisms alone are not sufficient to maintain this state. Cold can be defined as a temperature below a certain threshold or as a loss of performance due to low physiological temperatures (e.g., cold fingers), the perception of an uncomfortable condition, the need for additional protective clothing worn (with increased energy expenditure and restricted movement), or a combination of these factors (Kuklane and Kaced, 2021). In such situations, the protective role of clothing becomes crucial.

Under the conditions discussed in this thesis (i.e., in cold environments), cold-induced vasoconstriction (CIVC) occurs in people exposed to cold, leading to a reduction in blood flow. This reduces convective heat transfer between the body core and surrounding tissues (skin, subcutaneous fat, and skeletal muscle), effectively increasing the insulation provided by the body shell (Castellani and Young, 2016). However, in a harsh environment, heat loss can exceed heat production, resulting in a drop in skin temperature.

CIVC begins when the skin temperature falls below a certain level, usually around 35 °C (ASHRAE, 2017), and reaches a maximum when the skin temperature falls to 31 °C or below (Veicsteinas et al., 1982). Peripheral blood flow is reduced the most to protect the body's core, making the extremities (such as the hands and feet) particularly vulnerable.

Below this set point (van Ooijen, 2008), muscle shivering is triggered to generate additional heat, which can increase metabolic heat production at rest by up to 4.5 met (Eyolfson et al., 2001; Haman, 2006).

In addition to these immediate mechanisms, cold exposure can also cause a paradoxical acute increase in local cutaneous blood flow, which increases tissue temperature and potentially protects the extremities from cold injuries. This phenomenon, known as known as cold-induced vasodilation (CIVD) (Cheung and Daanen, 2012; Flouris et al., 2008; Youssef et al., 2019) occurs after a period of decreased skin temperature and blood flow in the extremities, followed by a brief rewarming and increased blood perfusion. CIVD is usually characterised by a cyclical rise and fall in skin temperature. This response is mediated by the opening and closing of arteriovenous anastomoses (AVAs), which are direct connections between small arteries and veins without intervening capillaries.

1.1.3 Role of clothing

Clothing provides additional protection for a wide range of environmental conditions. However, its design and selection must be tailored to the specific context in which it is used: for example, the insulation needed by a person working in a cold room differs significantly from that needed by an alpinist. The effective selection of a garment ensemble requires a comprehensive understanding of how the wearer's physiological and anthropometric characteristics, activity level, environment, and garment properties interact in each scenario (Potter et al., 2020). The most reliable way to assess the impact of clothing under these conditions is to directly measure its thermal and biophysical properties.

The most commonly used method for assessing the thermal and evaporative properties of textiles is the guarded hot plate method, according to ISO 11092:2014 (ISO, 2014) [2] and ISO 9920:2007 (ISO, 2007) [3]. This method provides a more comprehensive framework for evaluating clothing systems. It includes tabulated values for the thermal insulation of standard clothing ensembles, recommendations for estimating the thermal performance of multi-layered garments, and procedures for in vivo testing to assess the insulation of the complete ensemble. Figure 1.1 shows the stepwise approach to determine clothing insulation shown in the aforementioned standard [4].

However, while these methods offer valuable guidance, they do not fully account for the detailed heat transfer interactions or zonal variations within the garment, which has motivated the development of thermal manikins. To overcome this limitation, thermal (and sweating) manikins were developed (Xu et al., 2016). Thermal manikin testing allows the measurement of dry and evaporative heat transfer of a garment worn by a heated, sweating manikin in a controlled climatic chamber. The relevant standard for these tests is ISO 15831:2004 (ISO, 2004) [5]. According to the standard procedure, the manikin is dressed in the complete ensemble, with each garment positioned as it would be used in practice.

The main advantage of the manikin test compared to the guarded hot plate is that the heat transfer properties of the entire ensemble as worn are assessed, taking into account not only the properties of the individual textiles, but also the design, fit, and

---

[2] Textiles - Physiological effects - Measurement of thermal and water vapour resistance under steady-state conditions (sweating guarded-hotplate test)

[3] Ergonomics of the thermal environment - Estimation of thermal insulation and water vapour resistance of a clothing ensemble

[4] In Figure 1.1, the terms **clothing ensemble** and **garments in the database** refer to the tabulated values of thermal insulation provided for common clothing configurations. These tables report insulation both in clo and in m^2KW^{-1}, and can be used directly when the clothing worn corresponds to one of the listed ensembles.

[5] Clothing - Physiological effects - Measurement of thermal insulation by means of a thermal manikin

drape of the garment on the body (O'Brien et al., 2011).

Another important parameter that influences thermal comfort is air permeability. An accurate estimation of this property requires consideration of wind speed and its impact on the biophysical performance of the ensemble. The standard method for measuring air permeability is described in ISO 9237:1995 (ISO, 1995) [6].

In addition to thermal resistance and air permeability, moisture management plays a crucial role in determining comfort and protection in cold environments. The ability of footwear and clothing systems to wick sweat and water vapour away from the skin directly affects heat loss, the risk of condensation, and ultimately the perception of dryness and comfort. For this reason, moisture transport properties, also assessed through ISO 11092:2014 (ISO, 2014), should be considered alongside thermal insulation and air permeability when evaluating the overall performance of protective clothing.

1.2 Thermal comfort in footwear

1.2.1 Cold-protective footwear

The feet are highly active thermoregulatory body regions that can function as effective heat exchangers in both hot and cold environments (Taylor et al., 2014; Youssef et al., 2019). Similar to the hands, they exhibit a relatively large surface area compared to their volume (Williamson et al., 1984), which promotes heat dissipation but also results in substantial heat loss under cold exposure due to an unfavourable surface-to-mass ratio. In addition, the feet are in continuous contact with the ground, making them particularly susceptible to conductive heat transfer (Holmér, 1993), while containing only a limited amount of muscle mass capable of generating metabolic heat. As a result, the human foot is physiologically predisposed to heat dissipation rather than heat conservation, and its local heat storage is typically negative, with heat losses exceeding local heat production.

Despite accounting for approximately 7% of the total body surface area (West, 2019), the feet rely predominantly on blood perfusion from the body core to maintain thermal balance. However, unlike the core, which is tightly regulated to preserve vital organ function, the extremities are subject to pronounced peripheral vasomotor

---

[6] Textiles - Determination of the permeability of fabrics to air

control. In cold conditions, vasoconstriction markedly reduces cutaneous blood flow to the feet, limiting convective heat transfer from the core and causing local skin temperature to decrease rapidly, even when core temperature remains within a thermoneutral range. This physiological strategy prioritises whole-body thermal homeostasis at the expense of peripheral thermal comfort.

Thermal comfort at the foot is therefore governed primarily by local skin temperature and blood perfusion rather than by the overall thermal state of the body. Toe temperature has been widely adopted as a reliable indicator of local foot comfort (Kuklane, 1999; Kuklane et al., 1998). When toe temperatures lie between 20 and 25 °C, the foot is generally perceived as thermally comfortable. As temperature decreases below this range, discomfort progressively increases, and when local temperatures approach approximately 15 °C, reduced blood perfusion combined with heightened activation of cold receptors leads to pain sensation and an increased risk of cold-related injury. For this reason, 15 °C can be considered a conservative safety threshold for the foot, distinct from whole-body thermal comfort criteria.

Skin temperature alone, however, does not fully determine thermal well-being. Under warm conditions, sweat production at the feet can reach 30–50 $\mathrm{g \cdot h^{-1}}$ (Fogarty et al., 2007; Taylor et al., 2006). In cold environments, perspiration rates are lower, but moisture accumulation at the interface between the foot and the inner surface of the footwear can still significantly reduce skin temperature and impair the insulating performance of the system. While cold-weather footwear is often equipped with impermeable or semi-permeable membranes to prevent external water ingress (e.g., rain or snow), these layers may hinder the outward transport of water vapour generated by sweat, thereby adversely affecting local thermal comfort.

Cold-protective footwear is generally categorised according to the ambient temperature and functional requirements (Kuklane, 1999):

- **Above +5 °C**: No special requirements for insulation; the main focus is on preventing the penetration of moisture from the environment.
- **Between +5 °C and -10 °C**: The requirements for insulation are increasing. In addition to preventing the ingress of moisture from outside, a higher level of insulation is required to maintain foot comfort. For example, snow on the surface (above 0 °C) can melt and increase the heat load if it is not treated properly.

- **Below -10 °C**: Both external and internal moisture management become critical. Condensation can form on the inside of the boots, so materials with high insulation and effective moisture transport properties are required to maintain comfort and prevent cold injuries.

1.2.2 Current challenges and limitations

Despite advances in cold-protective footwear, several challenges remain in assessing thermal comfort and performance. One major difficulty deals with the complex geometry and multi-layer construction of modern boots. The combination of different materials, different insulation properties, and the presence of impermeable or semi-permeable membranes results in a heterogeneous system that is difficult to characterise and predict accurately.

Limitations of the test methods also pose a challenge. While tests on a guarded hot plate and on a thermal manikin provide valuable data, they cannot fully capture the dynamic interactions between the foot and the shoe during actual use, such as cyclic loading, localised pressure or different activity levels. In addition, the inter-individual differences in foot size, shape, and physiology make it difficult to generalise the results from a single subject or manikin.

Predictive modelling of thermal foot comfort in extreme environments remains limited. Computational methods, such as CFD (Computational Fluid Dynamics) and machine learning, face major challenges due to the multi-scale nature of heat and moisture transport, the dynamic physiological responses of the human body, and the limited availability of reliable experimental data in extreme cold conditions. These limitations motivate the development of hybrid approaches that combine experimental measurements, physics-based simulations, and data-driven modelling to more accurately predict the thermal performance of footwear.

Furthermore, the current standardised tests for cold-protective footwear have significant limitations. ISO 20344:2011 (ISO, 2011) [7] defines footwear as suitable for cold protection if a shoe placed in a cold chamber at -17 °C with heated steel balls shows a temperature drop of less than 10 °C at the plantar surface of the foot within 30 minutes. While this method provides a simple pass/fail criterion, it is not specific enough to discriminate between different levels of insulation or to describe the performance characteristics required for specific conditions (see Section 1.2.1).

---

[7] Personal protective equipment - Test methods for footwear

Therefore, two models may pass the test but differ significantly in practice in their specific performance.
This standard has been criticized in the literature (Kuklane et al., 1999, 2009) for several reasons:

- **Lack of real-world assessment**: The test mainly considers conductive heat transfer at the sole or insole and neglects other heat and moisture transport mechanisms that occur during actual use.
- **Lack of discrimination**: The criterion gives no indication of the relative insulating performance of footwear and thus provides limited information for manufacturers or consumers.
- **Deceptive feeling of safety**: In extreme conditions, such as work or mountaineering, footwear that passes this test could be considered personal protective equipment (PPE) rather than a comfort-oriented sports accessory. Relying solely on this pass/fail definition does not ensure adequate protection for the intended use.

1.3 State of the art and research gaps

1.3.1 Experimental studies

Due to their critical role in thermoregulation, extremities such as the hands and feet have been the subject of numerous experimental studies under cold exposure.
Most previous research focused on the thermoregulatory response (Bergersen et al., 1999; Massey et al., 2018; Mekjavic I. B., 2013) passive conditions and attempted to link cooling and rewarming dynamics to subjective perceptions of comfort and discomfort as well as physiological markers. In several studies, cold-induced vasodilation (CIVD) was further investigated using water immersion protocols (Chuansi et al., 2015; Kingma et al., 2019; Tyler et al., 2015). These studies showed how quickly CIVD can manifest after the onset of cold stress (an effect that is accentuated by the high thermal conductivity of water) and highlighted its potential protective role against cold-related injuries.
Other studies have focused specifically on the feet (Dobnikar et al., 2009; Li et al.,

2023; Reynolds et al., 2007; Weller et al., 2025), demonstrating not only the influence of local thermal responses on whole-body thermal comfort, but also providing valuable physiological data on the relationship between foot temperature ranges and subjective comfort. These results emphasise the importance of the foot for overall thermal perception, especially during cold stress.

While these studies have provided important theoretical foundations for understanding extremity thermoregulation, they also share common limitations. Most of them targeted either isolated phenomena (such as CIVD) or specific exposure protocols (e.g., hand or foot immersion) without developing a reproducible and integrative experimental framework. In particular, none of the existing protocols systematically links different aspects of heat production, insulation, and thermoregulatory responses in a way that allows a direct assessment of footwear performance and its physiological consequences. Closing this gap is a central motivation of the present work. Table 1.1 shows a resume of the goals, methods, and results of the most relevant experimental studies considered in the literature review.

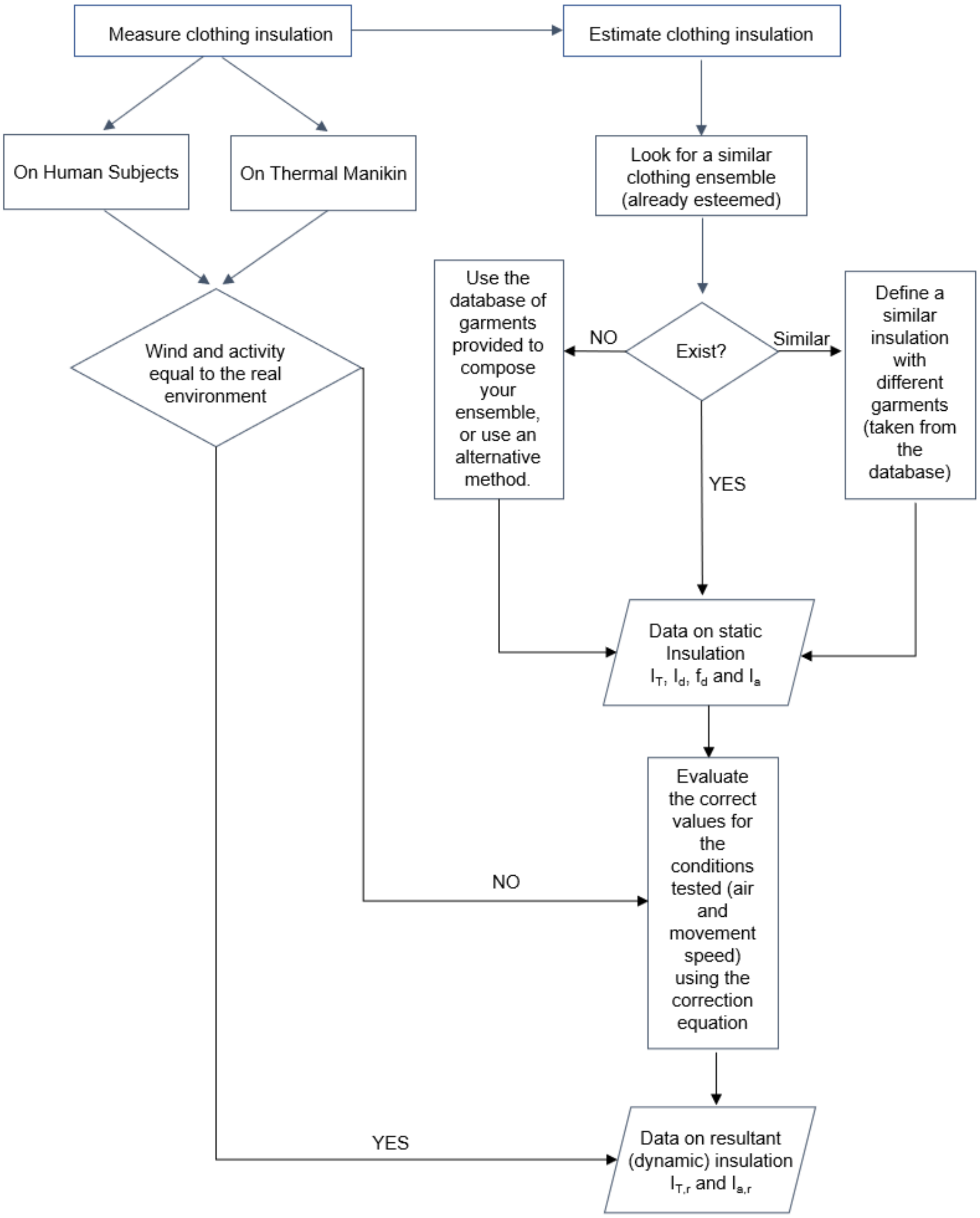

Fig. 1.1 Stepwise approach to determine clothing insulation adapted from ISO 9920:2007 (ISO, 2007).

Table 1.1 Comparison of experimental cold exposure studies

Study	Sample	Environment	Main Measurements	Activity	Focus
Li et al., 2023	16 (8M, 8F), 21 ± 2 yr	Climate chamber, 8–14°C	Foot skin temperature, thermal sensation, overall comfort	No	Feet
Massey et al., 2018	14 (8M, 6F), 23 ± 2 yr	Climate chamber, controlled cooling/rewarming, normoxia/hypoxia	Skin temp. hands/feet, rectal temp., laser Doppler, HR	Yes	Hands
Bergersen et al., 1999	21 (10F, 11M), 21 ± 3 yr	Climate chamber, 25±3°C	Arterial blood flow, laser-doppler flux, fingertip skin temp.	No	Hands
Daanen, 2003	9 males, 25 ± 5 yr	Hand immersion, 5–15°C	Finger skin temp., comfort, sensation	No	Hands
Weller et al., 2025	39 (20M, 19F), 24 ± 3 yr	Thermoneutral room, 22°C	Finger skin temp., CIVD parameters (Tmin, Tmax, Tmean, Tonset, waves)	No	Hands and feet
Reynolds et al., 2007	10 (5M, 5F), 22 ± 3 yr	Climate chamber	Foot skin temp., CIVD	No	Feet
Dobnikar et al., 2009	8 males 25 ± 5 yr	Climate chamber	Foot skin temp., CIVD	Yes	Feet
Tyler et al., 2015	30 (15M, 15F), 18 ± 3 30 yr	Hand immersion, 0°C and 8°C	Finger skin temp., CIVD onset, amplitude	No	Fingers
Kingma et al., 2018	12 (5M, 7F), 22 ± 2 yr	Ice water immersion	Finger skin temp., rewarming speed	No	Fingers
Gao et al., 2015	4 males	Extreme cold air (-30.6°C), treadmill exercise	Finger skin temp., CIVD, core temp. during exercise	Yes	Fingers

1.3.2 Physics-based approaches

Several attempts have been made to model heat transfer in footwear and evaluate its thermal performance under different conditions. A number of studies have focused on the role of footwear insulation in protecting the extremities. For instance, Kuklane et al. (Kuklane et al., 1998) carried out an extensive experimental campaign with human subjects in which the protective effect of insulating layers on skin temperature and thermal sensation was demonstrated. However, this approach remained strictly experimental and did not provide a modelling framework.

In other studies, numerical methods were used to simulate heat transfer. (Su et al., 2024) and (Jor et al., 2018; Puszkarz and Usupov, 2019) relied on simplified geometries and material representations, which limited their ability to account for the heterogeneous role of different areas of the footwear in heat and mass transfer.

A more sophisticated framework was proposed in (Nemati et al., 2021), where a detailed bio-thermal model was validated with experimental data during activity. However, the model was limited to mild environments and neglected the particular challenges of extreme cold. Again, the shoe geometry was greatly simplified compared to actual prototypes.

Other approaches relied on physical devices such as thermal manikins. (Bergquist and Holmér, 1997) and (West et al., 2020) have shown how measurements on manikins can provide objective insulation values and are useful for product development. However, manikins are expensive and not widely available.

Finally, optimisation-based models have also been proposed, such as (Nikbakht and Ahmadikia, 2024). Although this approach shows promise, it is still at an early stage and lacks extensive validation.

Compared to these approaches, the modelling framework presented in this thesis reproduces footwear geometry realistically and in detail, taking into account both the composition and regional differentiation of the boot. In addition, the model was validated using both in vivo experiments and manikin tests, which enabled the development of a digital twin of the thermal manikin test standard. This makes it possible to evaluate the thermal insulation of prototype shoe designs based on their material composition and construction, even before physical production. Table 1.2 presents a summary of the goals, methods, and results of the most relevant computational studies considered in the literature review.

Table 1.2 Comparison of physics-based footwear studies

Study	**Approach**	**Geometry**	**Environment**	**Validation**	**Limitations**
Kuklane et al., 1998	Experimental	Realistic (human subjects)	Cold environment	Human subjects	No modelling framework
Su et al., 2024	Numerical simulation	Simplified geometry	Cold environment	None or simplified comparison	Simplified geometry, limited regional differentiation
Puszkarz & Usupov, 2019	Numerical (FVM + Thermography)	Simplified geometry	Controlled conditions	Thermography	Simplified footwear geometry, limited regional accuracy
Nemati et al., 2021	Mathematical modelling	Simplified geometry	Mild environments	Experimental data during activity	Simplified geometry, not extreme cold
Bergquist & Holmér, 1997	Manikin measurement	Realistic (manikin)	Controlled conditions	Thermal manikin	High cost, no physiological response
West et al., 2020	Manikin measurement	Realistic (manikin)	Controlled conditions	Thermal manikin	Expensive, lacks physiological response
Nikbakht & Ahmadikia, 2024	Optimization + modelling	Geometrically parametric	Cold exposure (simulated)	Limited validation	Early-stage, limited experimental validation

1.3.3 Data-driven approaches

Recent advances have shown that combining statistical methods with methods with machine learning (ML) and deep learning (DL) techniques can significantly improve forecasting performance (Wolff et al., 2020). Several comparative studies have highlighted the superiority of ML-based models over traditional approaches in predicting air, ground and sea surface temperatures under a wide range of environmental conditions (Cifuentes et al., 2020; Saa and Ranathunga, 2020; Xiao et al., 2019; Zhang et al., 2017). Data-driven models are particularly valuable when it comes to capturing non-linear dependencies, processing large data sets and adapting to dynamic patterns, making them suitable for complex prediction tasks.

In the field of physiological applications, the use of machine learning for temperature prediction has increased significantly due to its versatility and generalisability (Nketiah et al., 2023). Recurrent Neural Networks (RNNs), and in particular Long Short-Term Memory networks (LSTMs) (Hochreiter and Schmidhuber, 1997) have proven to be extremely effective in modelling temporal processes. LSTMs solve the vanishing gradient problem that limits standard RNNs and allow them to capture long-term dependencies in time series data. Their ability to handle multivariate inputs supports their application in physiological monitoring and prediction tasks.

The first applications of LSTM networks in the neurological field demonstrated their ability to model complex temporal sequences such as speech signals (Graves and Schmidhuber, 2005). Soon after, LSTM architectures were used in physiological contexts to model time series data, including electrocardiogram (ECG) signals, blood pressure, and other vital signs. More recently, these networks have been used extensively to predict local or general human skin temperature (Cortes et al., 2024; Han et al., 2024; Katić et al., 2020; Liang et al., 2021; Liu et al., 2020; Morishima et al., 2021; Rida et al., 2023). Such approaches exploit the ability of LSTM models to learn temporal patterns in physiological signals, which makes them particularly suitable for the personalised prediction of thermal comfort and energy consumption.

Overall, data-driven methods complement physical and experimental approaches by providing predictive models that can be generalised across conditions and individuals, and provide a flexible framework for integrating large experimental datasets with real-time monitoring or simulation results. Table 1.3 presents a summary of the goals, methods, and results of the most relevant data-driven studies considered in the literature review.

Table 1.3 Comparison of data-driven studies on human temperature/thermal prediction

Study	Input data	Model	Task	Validation
Liu et al., 2020	Local skin temperatures	ML	Predict outdoor thermal comfort	Experimental validation with human subjects
Cortes et al., 2024	Vital signs, activity	LSTM	Personalized energy expenditure prediction	Time series validation, multivariate inputs
Morishima et al., 2021	Skin temperatures	ML regression	Skin temperature prediction	Human data
Katić et al., 2020	Skin temperatures, occupant behavior	ML	Personal thermal comfort prediction	Experimental dataset
Rida et al., 2023	Skin temperatures + video (CV)	ML + CV augmentation	Contactless thermal state estimation	Human subject data, CV augmentation
Han et al., 2024	Core + skin temperatures	LSTM	Forecast core and skin temperatures	Long-term time series validation
Liang et al., 2021	Body temperatures	RNN/LSTM	Body temperature prediction	Benchmark datasets
Tanwar et al., 2022	Thermal images	CNN	Predict skin temperature distribution	Image-based model, augmentation applied
Acikmese et al., 2019	Sensor time series	ML/LSTM	Predict core temperature	Multivariate physiological inputs, experimental validation
Karim et al., 2017	Time series (physiological)	LSTM	Multivariate time series prediction	Benchmark and synthetic datasets

1.4 Research motivation and objectives

1.4.1 Rationale for a hybrid approach

Thermoregulation of the human foot is influenced by complex interactions between environmental conditions, footwear design, and individual physiology. Experimental studies provide precious data on physiological responses, but are often limited in terms of reproducibility, environmental control or accessibility of extreme conditions. Physics-based models allow detailed investigation of heat transfer processes in footwear, but are often based on simplified geometries or do not fully capture physiological variability. Data-driven models, on the other hand, are characterised by learning complex temporal patterns from experimental datasets, but require reliable input data and may not be sufficiently interpretable.

A hybrid approach that combines experimental validation, physics-based modelling, and machine learning increases the strengths of each method. This integration is particularly valuable for applications in extreme environments where reproducing in vivo conditions may be tough.

1.4.2 Integration of methods

In this thesis, the hybrid methodology is realised through three interconnected concepts. Firstly, experimental campaigns on human subjects and thermal manikins provide data for model validation and knowledge on physiological phenomena in action. Secondly, physically based simulations of footwear reproduce the detailed geometry and material composition of the boot, enabling the investigation of thermal insulation under controlled conditions. Thirdly, machine learning models, particularly LSTMs, utilise time series of skin temperature and environmental measurements to predict local thermal responses of the foot under different scenarios. The integration of these methods ensures that the predictions are both physiologically plausible and based on realistic footwear properties. This strategy makes it possible to achieve two different objectives:

- A more "material-based" one regarding the thermal resistance of a prototype based on its composition.

- A more "physiology-based" one that takes into account human physiology and simulates real environmental conditions, such as the Duration of Safe Exposure.

1.5 Thesis Overview

This thesis investigates the thermal comfort and thermoregulation of humans in extreme environments, with a particular focus on evaluating the thermal insulation efficiency of cold-weather footwear. The central aim is to integrate experimental, physics-based, and data-driven approaches to gain a comprehensive understanding of the mechanisms governing heat transfer in footwear and their effects on human foot thermoregulation. The work is divided into three main parts.

The first part (Chapter 1) presents the state of the art and a literature review. This section provides an overview of the physiological processes that occur when humans are exposed to hostile environments such as cold and extremely cold climates, as considered in this project. In addition, the key challenges associated with the development and evaluation of footwear for cold weather are addressed. Particular attention is given to previous research using experimental, computational, and data-driven methods in order to highlight the strengths and limitations of each approach and identify the knowledge gaps that motivate the present work.

In the second part (Chapters 2 to 4), the methodological framework of the thesis is developed and applied. Three complementary approaches are implemented, and their results are presented:

Experimental approach: Tests with a thermal manikin and controlled experiments with human subjects were conducted to quantify and evaluate physiological reactions to cold exposure. This methodology follows the first three levels of the five-step system for analysing the physiological properties of textiles and garments (Figure 1.2), adapted from Umbach (1986).

The experimental workflow adopts a progressive, bottom-up strategy. It begins with the biophysical characterisation of the textile skin model (Level 1). Its thermal and physical properties are presented in Section 3.4.1 to maintain narrative continuity, while remaining critical for the CFD modelling setup. After this preliminary material analysis, the investigation proceeds to the evaluation of the garment as part of the complete clothing ensemble (Level 2). This step, conducted through thermal manikin tests, also addresses the lack of fitting assessment previously highlighted in Appendix A.

Once these two “apparative” tests were completed, the approach advanced to the in vivo configuration (Level 3), carrying out a series of controlled experiments with hu-

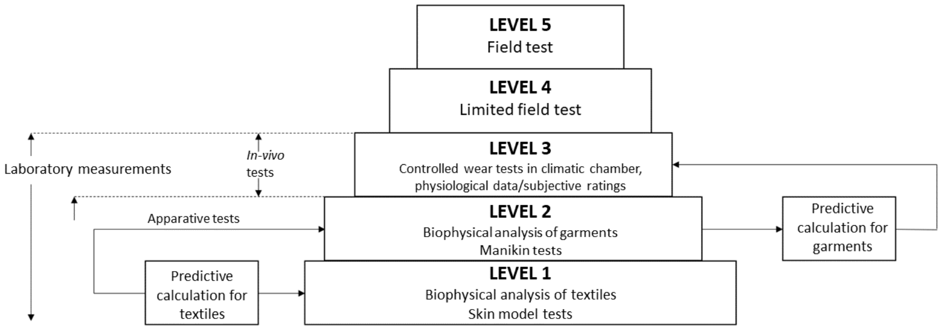

Fig. 1.2 Five-level system for the analysis of the physiological properties of textiles and garments, adapted from (Umbach, 1986).

man subjects to observe the thermo-physiological response under realistic conditions.

Physics-based modelling: Numerical simulations were conducted to replicate the footwear geometry and material composition, enabling the estimation of thermal insulation properties and the analysis of heat transfer mechanisms in a controlled virtual environment. This step allowed the creation of a digital twin of the foot thermal manikin, which was used to evaluate the thermal resistance of a prototype before production. This outcome was crucial for the assessment of the first evaluation parameter, the thermal resistance $\mathrm{R_{cT}}$.

Data-driven modelling: Two predictive approaches were compared: a statistical auto-regressive model (SARIMAX) and a neural network-based model primarily built on LSTM and fully connected architectures. Both methods were trained on datasets collected during the human trials and were designed to predict big toe temperature, which was selected as a benchmark indicator of foot thermal comfort. The prediction relies on a combination of inputs, both numerical and categorical, such as ambient temperature, physical activity level, and the thermal resistance of the considered boot. The latter parameter is obtained from the computational model developed in Chapter 2. However, as the target variable is a time-dependent physiological signal, the models also require a time series input rather than only

static features. For this purpose, the mean skin temperature time series generated by the JOS-3 thermoregulation model was used. JOS-3 produces this signal based on the same categorical inputs employed during training, ensuring consistency. The feasibility of predicting big toe temperature from mean skin temperature was supported by the strong correlation between these two variables observed in the experimental campaign.
This enables the achievement of the second evaluation parameter: the Duration of Safe Exposure (i.e., the time in minutes of exposure before the big toe reaches the critical threshold of 15 °C).

These three pillars are not treated in isolation but are integrated into a hybrid methodology where each component informs and validates the others.
Finally, the third part (Chapter 5) contains the conclusions of this work. It summarises the main contributions, reflects on the methodological advances made and discusses perspectives for future research, including the possible extension of the digital twin framework developed in this work to other types of protective clothing systems.

References

ASHRAE, 2017. ANSI/ASHRAE Standard 55-2017: Thermal Environmental Conditions for Human Occupancy. American Society of Heating, Refrigerating and Air-Conditioning Engineers, Atlanta, GA.

ASHRAE, 2023. Thermal Environmental Conditions for Human Occupancy. Technical Report. American Society of Heating, Refrigerating and Air-Conditioning Engineers. New York.

Bergersen, T.K., Hisdal, J., Walløe, L., 1999. Perfusion of the human finger during cold-induced vasodilatation. American Journal of Physiology-Regulatory, Integrative and Comparative Physiology 276, R731–R737. doi:10.1152/ajpregu.1999.276.3.R731.

Bergquist, K., Holmér, I., 1997. A method for dynamic measurement of the resistance to dry heat exchange by footwear. Applied Ergonomics 28, 383–388. doi:10.1016/s0003-6870(96)00079-8.

Blagden, C., 1775. Xii. experiments and observations in an heated room. Philosophical transactions of the Royal Society of London , 111–123.

Burton, A.C., 1934. The application of the theory of heat flow to the study of energy metabolism: Five figures. The Journal of Nutrition 7, 497–533.

Castellani, J.W., Young, A.J., 2016. Human physiological responses to cold exposure: Acute responses and acclimatization to prolonged exposure. Autonomic Neuroscience 196, 63–74.

Cheung, S.S., Daanen, H.A.M., 2012. Dynamic adaptation of the peripheral circulation to cold exposure. Microcirculation 19, 65–77. URL: https://doi.org/10.1111/j.1549-8719.2011.00126.x, doi:10.1111/j.1549-8719.2011.00126.x.

Chuansi, G., Lin, L.Y., Halder, A., Kuklane, K., 2015. Cold-induced vasodilation during continuous exercise in the extreme cold air (-30.6 °c). Extreme Physiology Medicine 4, A58. doi:10.1186/2046-7648-4-S1-A58.

Cifuentes, J., Bravo, C., Martínez, A., Bustamante, J., 2020. Air temperature forecasting using machine learning techniques: A review. Energies 13, 4215. doi:10.3390/en13164215.

Cortes, V.M.P., Chatterjee, A., Khovalyg, D., 2024. Dynamic personalized human body energy expenditure: Prediction using time series forecasting lstm models. Biomedical Signal Processing and Control 87, 105381. doi:10.1016/j.bspc.2024.105381.

Dobnikar, U., Kounalakis, S.N., Mekjavic, I.B., 2009. The effect of exercise-induced elevation in core temperature on cold-induced vasodilatation response in toes. European Journal of Applied Physiology 106, 457–464. doi:10.1007/s00421-009-1046-1.

Eyolfson, D.A., Tikuisis, P., Xu, X., Weseen, G., Giesbrecht, G.G., 2001. Measurement and prediction of peak shivering intensity in humans. European journal of applied physiology 84, 100–106.

Fanger, P.O., 1967. Calculation of thermal comfort: Introduction of a basic comfort equation. ASHRAE Transactions 73, III.4.1.

Flouris, A.D., Westwood, D.A., Mekjavic, I.B., Cheung, S.S., 2008. Effect of body temperature on cold induced vasodilation. European Journal of Applied Physiology 104, 491–499. URL: https://doi.org/10.1007/s00421-008-0798-3, doi:10.1007/s00421-008-0798-3.

Fogarty, A.L., Barlett, R., Ventenar, V., Havenith, G., 2007. Upper body sweat distribution during and after a 60 minute training run in male and female runners, in: Mekjavic, I.B., Kounalakis, S.N., Taylor, N.A.S. (Eds.), Proceedings of the 12th International Conference on Environmental Ergonomics, Biomed d.o.o., Ljubljana, Piran, Slovenia. pp. 270–272.

Fourier, J., 1822. Theorie analytique de la chaleur, par M. Fourier. Chez Firmin Didot, père et fils.

Graves, A., Schmidhuber, J., 2005. Framewise phoneme classification with bidirectional lstm and other neural network architectures. Neural Networks 18, 602–610. doi:10.1016/j.neunet.2005.06.042.

Haman, F., 2006. Shivering in the cold: from mechanisms of fuel selection to survival. Journal of Applied Physiology 100, 1702–1708.

Han, X., Zhang, L., Xu, S., Li, Y., 2024. Forecasting human core and skin temperatures: A long-term series approach. Big Data and Cognitive Computing 8, 197. doi:`10.3390/bdcc8120197`.

Hardy, J.D., Wolff, H.G., Goodell, H., 1952. Pain sensations and reactions. Williams & Wilkins.

Hensel, H., Schafer, K., 1984. Thermoreception and temperature regulation in man. Springer.

Hochreiter, S., Schmidhuber, J., 1997. Long short-term memory. Neural Computation 9, 1735–1780. doi:`10.1162/neco.1997.9.8.1735`.

Holmér, I., 1993. Tlv in cold environments. Journal of Thermal Biology 18, 643–646. doi:`10.1016/0306-4565(93)90106-4`.

ISO, 1995. Textiles – determination of permeability of fabrics to air. URL: https://www.iso.org/standard/18928.html.

ISO, 2004. Clothing – physiological effects – measurement of thermal insulation by means of a thermal manikin. URL: https://www.iso.org/standard/37956.html.

ISO, 2007. Ergonomics of the thermal environment – estimation of thermal insulation and water vapour resistance of a clothing ensemble. URL: https://www.iso.org/standard/38776.html.

ISO, 2011. Personal protective equipment – test methods for footwear. URL: https://www.iso.org/standard/51447.html.

ISO, 2014. Textiles – physiological effects – measurement of thermal and water-vapour resistance under steady-state conditions (sweating guarded-hotplate test).

J Bligh, K.G.J., 1973. Glossary of terms for thermal physiology. Journal of Applied Physiology Biol 35, 941–961. doi:`10.1152/jappl.1973.35.6.941.`

Jor, A., Hashar, M.R., Arefin, M.S., 2018. Study of thermal distribution and comfort in shoe through cfd technique. Global Journal of Science Frontier Research 18, 37–43. URL: https://journalofscience.org/index.php/GJSFR/article/view/2332.

Katić, K., Li, R., Zeiler, W., 2020. Machine learning algorithms applied to a prediction of personal overall thermal comfort using skin temperatures and occupants' heating behavior. Applied Ergonomics 85, 103078. doi:10.1016/j.apergo.2020.103078.

Kingma, B.R., Frijns, A.J., Schellen, L., van Marken Lichtenbelt, W.D., 2014. Beyond the classic thermoneutral zone: including thermal comfort. Temperature 1, 142–149.

Kingma, C.F., Hofman, I.I., Daanen, H.A.M., 2019. Relation between finger cold-induced vasodilation and rewarming speed after cold exposure. European Journal of Applied Physiology 119, 171–180. doi:10.1007/s00421-018-4012-y.

Kuklane, K., 1999. Footwear for cold environments: Thermal properties, performance and testing. Ph.D. thesis. Lund University of Technology. Lund, Sweden. URL: https://portal.research.lu.se/en/publications/footwear-for-cold-environments-thermal-properties-performance-and.

Kuklane, K., Geng, Q., Holmér, I., 1998. Effect of footwear insulation on thermal responses in the cold. International Journal of Occupational Safety and Ergonomics 4, 137–152. doi:10.1080/10803548.1998.11076386.

Kuklane, K., Holmer, I., Afanasieva, R., 1999. A comparison of two methods of determining thermal properties of footwear. International Journal of Occupational Safety and Ergonomics 5, 477–484.

Kuklane, K., Kaced, Y., 2021. Footwear for cold weather conditions.

Kuklane, K., Ueno, S., ichi Sawada, S., Holmér, I., 2009. Testing cold protection according to en iso 20344: Is there any professional footwear that does not pass? Annals of Occupational Hygiene 53, 63–68. URL: https://doi.org/10.1093/annhyg/men074, doi:10.1093/annhyg/men074.

Lefevre, J., 1911. Chaleur animale et bioéeenergétique. Masson et cie.

Li, Q., Liu, H., Wu, Y., Kosonen, R., Li, B., 2023. Effects of constant and fluctuating temperature modes of foot heating on human thermal responses in cold environments. Building and Environment 238, 110364. doi:10.1016/j.buildenv.2023.110364.

Liang, Z., Wang, X., Li, H., Li, J., 2021. Body temperature prediction with recurrent neural network and its variants, in: 2021 11th International Conference on Intelligent Control and Information Processing (ICICIP), IEEE. pp. 281–286. doi:10.1109/ICICIP53737.20.

Liu, K., Liu, Y., Wang, C., Wang, J., Chen, Y., 2020. A machine learning approach to predict outdoor thermal comfort using local skin temperatures. Sustainable Cities and Society 59, 102216. doi:10.1016/j.scs.2020.102216.

Massey, H.C., House, J.R., Tipton, M.J., 2018. Cutaneous vascular responses of the hands and feet to cooling, rewarming, and hypoxia in humans. Wilderness & Environmental Medicine 29, 45–55. doi:10.1016/j.wem.2017.10.004.

Mekjavic I. B., Dobnikar U., K.S.N., 2013. Cold-induced vasodilatation response in the fingers at 4 different water temperatures. Appl Physiol Nutr Metab 38, 14–20. doi:10.1139/apnm-2012-0118.

Morishima, S., Fujimoto, Y., Yamaguchi, T., Saito, K., 2021. Human body skin temperature prediction based on machine learning. Artificial Life and Robotics 26, 103–108. doi:10.1007/s10015-020-00617-5.

Nemati, H., Moghimi, M.A., Naemi, R., 2021. A mathematical model to investigate heat transfer in footwear during walking and jogging. Journal of Thermal Biology 97, 102778. doi:10.1016/j.jtherbio.2021.102778.

Nikbakht, A., Ahmadikia, H., 2024. Designing suitable shoes to prevent foot frostbite through optimization of the geometric dimensions of the shoe and sock model. Computer Methods in Biomechanics and Biomedical Engineering 27, 775–784. doi:10.1080/10255842.2023.2202791.

Nketiah, E.A., Agyeman, M.G., Oppong, A.K., 2023. Recurrent neural network modeling of multivariate time series and its application in temperature forecasting. PLoS ONE 18, e0285713. doi:10.1371/journal.pone.0285713.

van Ooijen, A., 2008. Human thermoregulation: individual differences in cold-induced thermogenesis. Ph.D. thesis.

O'Brien, C., Blanchard, L.A., Cadarette, B.S., Endrusick, T.L., Xu, X., Berglund, L.G., Sawka, M.N., Hoyt, R.W., 2011. Methods of evaluating protective clothing relative to heat and cold stress: Thermal manikin, biomedical modeling, and human testing. Journal of Occupational and Environmental Hygiene 8, 588–599. doi:10.1080/15459624.2011.613291.

Parsons, K.C., 2014. Human Thermal Environments: The Effects of Hot, Moderate, and Cold Environments on Human Health, Comfort, and Performance. 3rd ed., CRC Press, Boca Raton, FL. URL: https://doi.org/10.1201/b16750, doi:10.1201/b16750.

Potter, A.W., Looney, D.P., Xu, X., Santee, W.R., Srinivasan, S., 2020. Modeling thermoregulatory responses to cold environments, in: Sadaka, F. (Ed.), Autonomic Nervous System Monitoring: Heart Rate Variability. IntechOpen. URL: https://doi.org/10.5772/intechopen.81238, doi:10.5772/intechopen.81238.

Puszkarz, A.K., Usupov, A., 2019. The study of footwear thermal insulation using thermography and the finite volume method. International Journal of Thermophysics 40. doi:10.1007/s10765-019-2509-1.

Reynolds, L.F., Mekjavic, I.B., Cheung, S.S., 2007. Cold-induced vasodilatation in the foot is not homogenous or trainable over repeated cold exposure. European Journal of Applied Physiology 102, 73–78.

Rida, M., Darwish, A., Duarte, F., Haddad, R., 2023. Toward contactless human thermal monitoring: A framework for machine learning-based human thermophysiology modeling augmented with computer vision. Building and Environment 245, 110850. doi:10.1016/j.buildenv.2023.110850.

Saa, E.D., Ranathunga, L., 2020. Comparison between arima and deep learning models for temperature forecasting. arXiv preprint arXiv:2011.04452 URL: https://arxiv.org/abs/2011.04452.

Su, Y., Wang, H., Liu, G., Wang, Y., Liu, J., Tian, M., 2024. Numerical study of thermal comfort and energy efficiency about electrically heated footwear under a cold environment. International Journal of Clothing Science and Technology 36. doi:10.1108/IJCST-11-2023-0173.

Taylor, N.A.S., Galdwell, J.N., Mekjavic, I.B., 2006. The sweating foot: local differences in sweat secretion during exercise-induced hyperthermia. Aviation, Space, and Environmental Medicine 77, 1020–1027.

Taylor, N.A.S., Machado-Moreira, C.A., van den Heuvel, A.M.J., Caldwell, J.N., 2014. Hands and feet: physiological insulators, radiators and evaporators. European Journal of Applied Physiology 114, 2037–2060. URL: https://pubmed.ncbi.nlm.nih.gov/25011493/, doi:`10.1007/s00421-014-2940-8`.

Tyler, C.J., Reeve, T., Cheung, S.S., 2015. Correction: Cold-induced vasodilation during single digit immersion in 0°c and 8°c water in men and women. PLoS ONE 10. doi:`10.1371/journal.pone.0275188`.

Umbach, K., 1986. European Textile Research: Competitiveness Through Innovation.. Springer. chapter Evaluation of Textile and Garment Comfort. doi:`10.1007/978-94-009-4323-0_5`.

Veicsteinas, A., Ferretti, G., Rennie, D.W., 1982. Superficial shell insulation in resting and exercising men in cold water. Journal of Applied Physiology 52, 1557–1564.

Weller, R.S., Govaerts, J., Akkermans, R., Jones, D.M., Daanen, H.A., 2025. Influence of body dimensions and sex on cold-induced vasodilation. European Journal of Applied Physiology 125, 1385–1393.

West, A., 2019. Physiological and perceptual responses of the foot: interactions with footwear and the impact on comfort. Doctoral dissertation. Loughborough University.

West, A.M., Oberst, F., Tarrier, J., et al., 2020. A thermal foot manikin as a tool for footwear evaluation and development. Proceedings of the Institution of Mechanical Engineers, Part P: Journal of Sports Engineering and Technology 237, 34–46. doi:`10.1177/1754337120952229`.

Williamson, D.K., Chrenko, F.A., Hamley, E.J., 1984. A study of exposure to cold in cold stores. Applied Ergonomics 15, 25–30. URL: https://doi.org/10.1016/0003-6870(84)90005-4, doi:`10.1016/0003-6870(84)90005-4`.

Wolff, S., O'Donncha, F., Chenb, B., 2020. Statistical and machine learning ensemble modelling to forecast sea surface temperature. Journal of Marine Systems 208, 103347.

Xiao, C., Zhu, J., Fang, Y., Wu, L., 2019. Short and mid-term sea surface temperature prediction using time-series satellite data and lstm-adaboost combination approach. Remote Sensing of Environment 233, 111358. doi:10.1016/j.rse.2019.111358.

Xu, X., Gonzalez, J.A., Karis, A.J., Rioux, T.P., Potter, A.W., 2016. Use of thermal mannequins for evaluation of heat stress imposed by personal protective equipment, in: Shiels, B., Lehtonen, K. (Eds.), Performance of Protective Clothing and Equipment: 10th Volume, Risk Reduction through Research and Testing, ASTM STP1593. ASTM International, West Conshohocken, PA, pp. 286–296.

Youssef, A., Verachtert, A., De Bruyne, G., Aerts, J.M., 2019. Reverse engineering of thermoregulatory cold-induced vasoconstriction/vasodilation during localized cooling. Applied Sciences 9. URL: https://www.mdpi.com/2076-3417/9/16/3372, doi:10.3390/app9163372.

Zhang, Q., Zhang, Y., Zhao, J., Zhang, L., 2017. Prediction of sea surface temperature using long short-term memory. IEEE Geoscience and Remote Sensing Letters 14, 1745–1749. doi:10.1109/LGRS.2017.2731959.

Chapter 2

Experimental Approach

This chapter describes the experimental approach adopted for both the human and manikin tests. The research design included five experimental campaigns with human subjects (Section 2.1) and one experimental campaign with a thermal manikin (Section 2.2), each conducted under a range of controlled environmental and activity conditions.

The campaigns with human subjects were important to capture the physiological thermoregulatory responses to cold exposure, particularly in peripheral areas such as the toes, and to quantify how ambient temperature, physical activity and footwear insulation interact in real-life scenarios. These data not only enabled a deeper understanding of cold-induced mechanisms such as vasoconstriction and vasodilation, but also provided the reference time series and statistical data required for the subsequent phases of the project.

On the other hand, the tests on the thermal manikin served a complementary purpose: they enabled the insulation and controlled evaluation of specific physical phenomena, in particular the effects of moisture on the insulation of footwear. The systematic measurements obtained from the manikin campaigns were used to calibrate and validate the physical component of the project and ultimately contributed to the development of the digital twin tool.

2.1 Human Tests

2.1.1 Purpose of the study

The experimental campaigns with human subjects were designed with a twofold main objective. Firstly, to assess the reliability and consistency of the data available in the literature on the perception of thermal comfort of the feet in specific contexts. To this end, these perceptions had to be compared with the actual physiological responses of humans observed during cold tests. This preliminary investigation was crucial to provide a solid empirical basis for the subsequent analyses. The second objective was to create a robust and comprehensive database of experimental measurements. This database serves a dual purpose: it provides the necessary boundary conditions and validation data for the physics-based footwear models, and it provides high-quality training data for the development of data-driven models, including machine learning approaches such as LSTMs. By combining these two objectives, the experimental work ensures both physiological relevance and computational utility for subsequent modelling efforts.

According to the existing literature (Kuklane, 2009), it is assumed that the pain receptors override the cold receptors when the big toe reaches a threshold of 15 °C. This is often referred to as the critical point. This threshold is often regarded as the body's last significant warning to avoid potentially dangerous situations and was therefore adopted as the physiological reference threshold in this study. Based on this assumption, one of the aims of the experimental investigation was to observe if, how, and when participants reached this point under different boundary conditions, namely footwear insulation, ambient temperature, and physical activity. This approach allowed us to introduce a new discriminatory parameter for the insulation performance of footwear, defined as "*Duration of Safe Exposure*" (DSE), i.e., the time (in minutes) for which a person can be safely exposed to the investigated environment while wearing a specific footwear model.

The five test campaigns were therefore designed to thoroughly analyze the influence of these key factors on human thermoregulation. The systematic analysis of environmental conditions, insulation levels, and activity intensities enabled a detailed understanding of their interaction and their effects on the thermophysiological responses of participants, while providing the empirical basis for subsequent modelling and discussion.

Part of the work described in this chapter has been previously published in Bianca et al. (2024).

2.1.2 Materials and Methods

2.1.2.1 Ethical Approval

The experimental protocol with human subjects was reviewed and approved by the Ethics Committee of the Politecnico di Torino (Authorisation ID: 87212/2025) and conducted following the principles of the Declaration of Helsinki. All participants gave written informed consent before participating in the study. In addition, personal data were anonymised and treated in accordance with the applicable data protection regulations.

2.1.2.2 Sampling Methods and Enrollment

Participants were eligible for participation if they met the following inclusion criteria: male gender, age between 18 and 55 years, good physical fitness confirmed by a valid medical sports certificate, and regular exposure to cold environments. All subjects had to be within a normal weight range (i.e., neither underweight nor overweight with a Body Mass Index (BMI) between 18.5 and 24.9). Exclusion criteria included a history of cardiovascular, pulmonary, or musculoskeletal disease and previous frostbite.

2.1.2.3 Overview of the Experimental Campaign

Five different experimental campaigns were conducted in a controlled climate chamber to thoroughly investigate human thermoregulation in cold environments under different boundary conditions. These conditions included different ambient temperatures, activity levels and footwear insulation systems. Whilst the basic approach to monitoring physiology and environmental conditions remained the same, the experimental design evolved across the campaigns. This evolution was crucial to address increasingly specific research questions, ranging from initial exploratory studies to field-like simulations and carefully controlled parametric assessments. Each campaign varied in terms of the number of participants, the specific test conditions (e.g., static vs. dynamic activities), and the boot models tested.

1. **Explorative campaign**: Three initial test protocols were developed to represent typical alpine conditions: two models simulating normal mountaineering and ice climbing activities, and one model representing an extreme high-altitude expedition. A key objective was to evaluate the body's thermoregulatory response under these scenarios and to verify whether the levels of physical activity achieved during the tests were consistent with those expected in real-life alpine conditions. In addition, the experimental setup enabled the validation of the test procedures and ensured repeatability for future campaigns.

2. **Real Expedition**: After validating the protocols in the exploratory campaign, a second set of tests was conducted with a larger sample size. The same three boot models were used to replicate the previous scenarios. A main objective of this campaign was to evaluate inter-subject variability and monitor toe temperatures, in particular to verify that the big toe is indeed the area most sensitive to cold exposure.

3. **Worst case scenario**: Building on the metabolic and temperature data collected in previous campaigns, this campaign was designed to simulate a worst-case scenario in which the test subjects remained completely motionless during the entire exposure. The aim was to observe more closely the speed and extent of cooling in the absence of physical activity. As previous data showed that models A and B performed similarly, only the least insulating (model A) and most insulating (model C) boots were tested.

4. **Ambient temperature and activity influence**: This campaign focused on the combined effects of ambient temperature and physical activity on thermoregulation of the feet. Subjects either walked very slowly at a speed of 3 km/h (to prevent shivering) or stood still while being exposed to two different ambient temperatures. Only model A was used to maintain consistency and isolate the effects of environmental and behavioural variables.

5. **Boot insulation**: In the last campaign, the influence of boot insulation on thermoregulation was investigated under both static and dynamic conditions.

The ambient temperature was kept constant, while two newly introduced boot models (model D and model E) with differing insulation levels were tested. This allowed a parametric evaluation of the role of footwear in maintaining thermal comfort of the feet.

2.1.2.4 Experimental Protocols

The various experimental protocols used in all campaigns were meticulously designed to simulate a range of conditions and activity levels relevant to cold environments. The level of physical activity within each protocol was systematically categorised as follows: 0 for stillness, 1 for light activity, and 2 for high exertion.
The protocols, which were designed to simulate realistic alpine scenarios, were developed in close collaboration with experienced athletes to ensure that they accurately reflected the sequence and nature of activities in high-altitude expeditions. These "*alpinism*" protocols, three in number (each originally associated with a specific boot model), were structured as an alternating sequence of activities such as standing still, walking, or climbing. It is important to note that Protocol C, which was designed to simulate very high altitude conditions, generally did not include the climbing phase in the same way as the other two protocols did (i.e., with crampons and ice axes) but more simulating a slow ascent in a ladder or in high steps.
A detailed diagram illustrating the duration and sequence of the individual phases in these protocols is shown in Figure 2.1.

While the pictographic representation of the activity protocols provides an intuitive visual overview of the temporal structure of the tests, direct comparison between protocols may be challenging when relying on the figure alone. For this reason, Table 2.1 summarises the sequence, type, and duration of each activity phase for Protocols A, B, and C. This consolidated description is intended to support rapid comparison across trials and to facilitate interpretation of the experimental results presented in the following sections.

Fig. 2.1 Detailed temporal sequence of activities for the ’alpinism’ protocols. The figure depicts the alternating phases of stillness, walking, and climbing, along with their respective durations, as designed to simulate high-altitude expedition scenarios.

Table 2.1 Summary of the experimental activity protocols adopted in the human tests. W = walking at 3 km/h, S = stillness, C = climbing.

Protocol	**Phase 1**	**Phase 2**	**Phase 3**	**Phase 4**	**Phase 5**	**Phase 6**	**Phase 7**
A	W (10)	S (10)	C (10)	S (20)	C (10)	S (10)	–
B	W (10)	S (5)	C (10)	S (20)	W (15)	S (10)	–
C	W (10)	S (5)	C (10)	W (10)	S (20)	C (10)	S (5)

2.1.2.5 Common Methodological Aspects

This section details the primary instrumentation and methods consistently employed across the experimental campaigns to ensure robust and comparable data acquisition. While the specific parameters varied slightly between campaigns based on their distinct objectives, the core set of equipment remained consistent.

- **Climate chamber**: All experimental tests were conducted within a controlled climatic chamber, which allowed for precise regulation of ambient temperature and relative humidity. The chamber was capable of simulating a wide range of

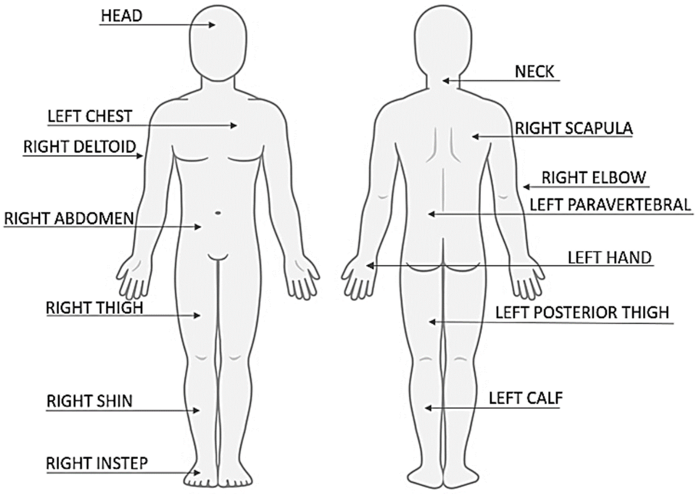

Fig. 2.2 Body areas defined by the norm ISO 9886:2008 to evaluate mean skin temperature.

cold conditions, with ambient temperatures varying from a minimum of -10°C to a maximum of -30°C. For all conducted tests, a constant wind speed of 0.5 m/s was maintained within the chamber to ensure consistent convective heat transfer conditions.

- **Skin temperature and humidity measurements**: Mean skin temperature and local humidity were measured in accordance with International Standard ISO 9886:2004: "*Ergonomics: Evaluation of thermal strain by physiological measurements*" (ISO, 2008). This involved the placement of fourteen probes (I-Button DS19239, Maxim Integrated, California, USA) at predetermined body sites specified by the standard (details in Figure 2.2. These probes offered a correctable accuracy of ±0.5 °C within their operational temperature range.

  The mean skin temperature was assessed according to the specified standard ISO 9886:2004, using the following formula:

$$\mathrm{T_{sk}} = \sum_{\mathrm{i}=1}^{14} 0.07143 * \mathrm{T_i} \tag{2.1}$$

  For more granular data, particularly concerning specific body parts such as the toes, temperatures were additionally monitored using dedicated probes connected to an external data logger MSR 147 (MSR-Electronics GmbH, Switzerland). These sensors provided a higher correctable accuracy of ±0.2

°C within their relevant temperature range. The humidity sensors utilized across the setup maintained an accuracy of $\pm 1.8\%$ in the temperature and humidity range in which they were used.

- **Heart and Metabolic Rate**: The participants' activity levels were assessed and controlled through a combination of physiological monitoring tools. Heart rate (HR) was continuously monitored using a Garmin Forerunner 230 connected to a compatible chest strap. This provided an estimation of physiological exertion. Complementing this, metabolic rate (MR) was measured using a Cosmed K5 metabolimeter (Cosmed, Rome, Italy), which allowed for the quantification of energy expenditure and a more precise evaluation of activity intensity.

  Wether the direct measurement of the MR was not possible, the value of the different activities involved was assessed according to the standard BS EN ISO 8996:2021: "*Ergonomics of the thermal environment Determination of metabolic rate*" (ISO, 2021). Following the standard, the MR of a single activity was first estimated according to the procedure *"Evaluation of the metabolic rate at level 2, Observation"*.

  According to the different activities considered, the metabolic rate (MR) was assessed using activity-specific formulations, in line with the hierarchical approach proposed in the relevant standards. The adopted equations account for the distinct physiological contributions to energy expenditure associated with static postures, locomotion, and vertical displacement, allowing a more realistic estimation of the metabolic demand under each condition.

  For low-activity conditions, the metabolic rate was estimated as a function of the body surface area $\mathrm{A_{DU}}$, with sex-specific coefficients reflecting average differences in basal metabolic demand:

$$\begin{aligned} \mathrm{M_{men}} &= 60 \cdot \mathrm{A_{DU}} \\ \mathrm{M_{women}} &= 55 \cdot \mathrm{A_{DU}} \end{aligned} \tag{2.2}$$

  During walking at speeds below 6 km/h, the metabolic rate was evaluated by explicitly accounting for the mechanical work associated with horizontal displacement and terrain slope. In this formulation, the walking speed $\mathrm{v_w}$ and the gradient G modulate the energetic cost, which is scaled by the total carried mass, given by the sum of body mass $\mathrm{W_b}$ and external load L:

$$\mathrm{M} = (0.5 + 0.37 \cdot \mathrm{v_w} + 0.2 \cdot \mathrm{v_w} \cdot \mathrm{G})(\mathrm{W_b} + \mathrm{L}) \tag{2.3}$$

For ladder ascent and descent, the metabolic rate was estimated based on the number of rungs negotiated per unit time, which serves as a proxy for vertical mechanical work. Separate formulations were adopted for ascending and descending conditions to reflect their different muscular and energetic demands:

$$\begin{aligned} \mathrm{M} &= (2.78 + \frac{\mathrm{N_{rungs}}}{4})(\mathrm{W_b} + \mathrm{L}) \\ \mathrm{M} &= (1.98 + \frac{\mathrm{N_{rungs}}}{23})(\mathrm{W_b} + \mathrm{L}) \end{aligned} \tag{2.4}$$

However, for climbing activities, the standard analytical formulations were not applicable due to the complex and highly individual nature of the task, which involves intermittent effort, upper- and lower-limb coordination, and variable pacing. For this reason, the metabolic rate was assessed using the Level 3 “Analysis” procedure, which estimates energy expenditure based on cardiovascular response. In this approach, the metabolic rate $\mathrm{M_m}$ is derived from the measured heart rate $\mathrm{HR_m}$ relative to the resting heart rate $\mathrm{HR_0}$, assuming a linear relationship between heart rate and metabolic demand within the considered intensity range:

$$\mathrm{M_m} = \mathrm{M_0} + \frac{\mathrm{HR_m} - \mathrm{HR_0}}{\mathrm{RM}} \tag{2.5}$$

The proportionality factor RM was calculated from subject-specific maximum work capacity MWC and heart rate reserve, as follows:

$$\begin{aligned} \mathrm{RM} &= \frac{\mathrm{HR_{max}} - \mathrm{HR_0}}{\mathrm{MWC} - \mathrm{M_0}} \\ \mathrm{MWC_{men}} &= (19.45 - 0.133 \cdot \mathrm{Age}) \cdot \mathrm{W_{bl}} \\ \mathrm{MWC_{women}} &= (17.51 - 0.150 \cdot \mathrm{Age}) \cdot \mathrm{W_{bl}} \end{aligned} \tag{2.6}$$

This multi-level approach allows the metabolic rate estimation to be adapted to the physiological and mechanical characteristics of each activity, improving the representativeness of the input data used in subsequent thermal and comfort analyses. Factors such as BSA, lean body mass and HR (at rest and during the single activity) of the participants were considered.

- **Thermal images**: To visually document and analyze thermal patterns, thermal images of the sides and soles of the footwear were acquired at constant intervals throughout the tests. This was achieved using a FLIR A310f thermal camera (FLIR, Wilsonville, Oregon, USA), which provided non-contact temperature distribution data crucial for assessing footwear insulation performance. The results achieved with the detection of these thermal images are discussed in Chapter 3, Section 3.4.1.
- **Subjective perceptions**: Participants' subjective evaluations of thermal comfort and perceived thermal sensations were systematically collected at constant intervals during the experimental sessions. These perceptions were recorded using a 13-point scale, in accordance with the guidelines outlined in International Standard ISO 10551:2019: "*Ergonomics of the physical environment. Subjective judgement scales for assessing physical environments*" (ISO, 2019). This allowed for a qualitative assessment of the participants' thermal experiences.

2.1.2.6 Differences Between Campaign

While several parameters were recorded consistently across the campaigns, including mean skin temperature, big toe temperature, and heart rate, other measurements varied depending on the specific objectives of each experiment. A detailed overview of the experimental protocols is provided in Table 2.2.
An illustration of the five tested footwear models can be seen in Figure 2.3.

Campaign 1 served as the first exploratory study with a small sample size (n=3). In this campaign, comprehensive metabolic data and thermal images were collected to allow initial comparisons with the existing literature.
Campaign 2 involved a larger group of participants during a simulated alpine expedition (following alpinism protocols A, B, and C). This campaign utilised similar environmental and footwear protocols to Campaign 1. An important addition was

Fig. 2.3 Illustration of the tested footwear models. From left to right: Model A (up to 4000 m), Model B (up to 6000 m and ice climbing), Model C (extreme mountaineering and Arctic crossings), Model D (short daily non-extreme hikes), and Model E (long non-extreme hikes).

the recording of the temperatures of the middle and little toes, in particular to check that the big toe is actually most susceptible to the effect of vasoconstriction.

Campaign 3 was specifically designed to investigate a worst-case scenario of passive cooling (i.e., no physical activity). In this campaign, both heart rate and metabolic rate were continuously monitored to comprehensively observe the effects of high temperatures on human energy balance.

In campaign 4, both the ambient temperature and the activity level were systematically varied. In this campaign, the temperature of the toes was accurately measured, including the big, middle, and little toes. Of note, no metabolic rate data were collected in this case, as metabolic activity was primarily monitored via heart rate only.

Campaign 5 focused on investigating the role of different insulation levels of the boots, both under static (non-moving) and dynamic (moving) conditions.

In order to accurately assess the thermal conditions to which the participants were exposed, the insulation values of clothing (I_{cl}) and footwear were also assessed individually. These measurements were carried out in accordance with the ISO 15831:2004 (ISO, 2004) standard using a thermal manikin. The operating conditions and methodology of the manikin are described in detail in Section 2.2.2.

Table 2.2 Summary of Experimental Campaigns

Campaign	Purpose	Testers	Boots & Protocols	Data Collected
1 - Explorative	Explore thermoregulation in three scenarios (two moderate, one extreme). Validate protocol and compare with literature.	3 testers	Model A at -15°C (alpinism A); Model B at -20°C (alpinism B); Model C at -30°C (alpinism C)	Mean skin temp. and RH; big toe temp. and RH; thermographies; metabolic and heart rates
2 - Real Expedition	Apply validated protocols to a larger sample during a simulated alpinism expedition.	8 men	Model A (-15°C); Model B (-20°C); Model C (-30°C)	Same as Campaign 1
3 - Worst Case	Simulate worst-case scenario: no movement, no metabolic generation. Observe rapid cooling.	6 men 4 women	Model A at -17°C (still); Model C at -30°C (still)	Mean skin temp. and RH; big toe temp. and RH; thermographies; heart rates
4 - Temp & Activity	Investigate the impact of temperature and activity level. Movement done slowly to prevent shivering.	6 men	Model A at -17°C and -10°C (still and walking)	Mean skin temp.; big toe temp.; heart rates
5 - Boot Insulation	Compare different insulation levels under same environmental and activity conditions.	9 men	Model D and E at -13°C (still and walking)	Mean skin temp. and RH; big toe temp. and RH; thermographies; heart rates

2.2 Manikin Tests

2.2.1 Purpose of the study

As has been observed in human testing, the exertion associated with mountaineering is high enough to induce significant sweat production, even in cold environments. Due to the high hydrophobicity of the materials involved and the presence of an outer impermeable or semi-permeable gaiter, the sweat produced by the body has difficulty leaving the system. This is usually the main reason for the decrease in thermal insulation. The presence of moisture not only impairs thermal performance, but also has a direct effect on the wearer's perception of comfort. If sweat evaporation cannot keep pace with sweat production, the accumulated moisture not only leads to a rapid drop in temperature, but also disrupts the interaction between skin and fabric, resulting in an unpleasant stickiness. In extreme cases, condensation in a garment with low vapour permeability can contribute to a rapid loss of body heat after activity, significantly increasing the risk of hypothermia, especially in cold and wet conditions. However, the interplay of evaporation and condensation that forms the water cycle in such a system is far more complicated than it appears at first glance.

The experimental campaign with a thermal manikin was specifically designed to investigate the effects of internal humidity on the thermal insulation of a closed system such as a boot from a quantitative point of view (i.e. the user's perception of comfort is not taken into account here). The main objective was to analyse the different phases of this internal water cycle and their influence on heat loss within the human-boot system. This was achieved by manually adding controlled amounts of water into the socks of the thermal manikin to simulate different sweating rates. In contrast to previous work (Bogerd et al., 2012; West et al., 2023) conducted on thermal foot manikins, this study focuses on the entire foot area to comprehensively observe the effects of phase change and water migration on the overall thermal properties of the system.

Part of the work described in this chapter has been previously published in (Bianca et al., 2025).

2.2.2 Materials and Methods

The measurements were carried out with the “Newton” thermal manikin (Thermetrics, Seattle, WA) shown in Figure 3.4.2. The manikin consists of 30 thermal zones, the temperature of which can be controlled individually using a software (ThermDAC Control Software, Thermetrics). The temperature sensors are located in each zone and protected by an epoxy coating. The temperature of each thermal zone was set to 34°C.

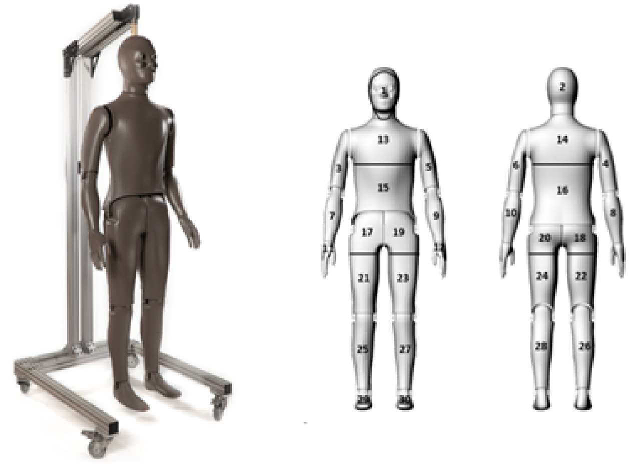

Fig. 2.4 “Newton” Manikin (Thermetrics, Seattle, WA) and its standard thermal zones schematic

The model simulates a male body with the following physical characteristics: 178.5 cm height (body circumferences 90.8 cm chest, 73.2 cm waist, 91.8 cm hips), and 1.8109 m^2 body surface area (BSA) . The energy needed to keep the manikin at a constant surface temperature is an indicator of heat loss to the environment.

The manikin was placed in a standing position in a climatic chamber with controlled temperature and humidity in a wind tunnel, where six fans generate a wind speed of 0.4 m/s. Wind speed, temperature, and humidity data were additionally monitored with the use of sensors placed in front of the manikin. As the study focuses on the foot-shoe system, the sensors were placed at a height of 20 and 44 cm above the ground and 30 cm away from the manikin.

As the aim of the study was to determine how moisture affects the thermal properties of the boots themselves, the whole clothing ensemble was selected and standardized in advance for the entire test procedure, with only the amount of water in the socks

changing to simulate the sweat produced by an athlete.
The clothing consisted of the same clothing configuration adopted in protocol A for the experimental campaign "*alpinism*" as detailed in Appendix A.
The characteristics of the socks are detailed in Table 2.3:

Model	**Fiber type**	**Structure**	**Weight (g)**
Ankle-socks	94% cotton 3% polyamide 3% elastane	Single jersey, ribbed cuff	15.25 ± 0.06

Table 2.3 Material composition, structure, and weight of the ankle socks used in the test.

The choice of sock material warrants specific discussion, as the use of cotton does not fully reflect typical cold-weather or mountaineering practice, where wool or synthetic blends are more commonly adopted due to their superior moisture management properties. In the present study, cotton socks were deliberately selected as a controlled reference material rather than as an optimal solution for cold protection. Cotton is characterised by high hygroscopicity and a strong tendency to retain liquid water within the fibre structure. This behaviour was intentionally exploited to amplify moisture-related phenomena at the foot-footwear interface, such as sweat accumulation, evaporation, and condensation, thereby making the coupled heat and mass transfer processes more observable under experimental conditions. In this sense, the selected sock material represents a conservative or worst-case scenario with respect to moisture retention, allowing the effects of water accumulation on thermal insulation to be clearly identified and quantified.
While the absolute magnitude of moisture accumulation and associated heat losses would be expected to differ when using wool or synthetic materials, the underlying physical mechanisms governing vapour transport, condensation, and insulation degradation remain the same. The use of cotton, therefore, supports the primary objective of this study, which is to investigate and characterise the impact of moisture on footwear thermal performance under controlled and repeatable conditions, rather than to reproduce best-practice clothing systems for cold exposure. The extension of the experimental protocol to alternative sock materials with enhanced moisture transport properties is identified as an important direction for future work.
The internal surface of the boot is fully lined with a microfleece layer. Moving outward, this layer is overlapped by a layer of Primaloft in the lower part and

toe area, given its high insulating power, polyurethane foam on the lateral sides, and honeycomb-structured polyurethane foam coupled with a polymeric mesh in the upper tongue area. The outermost layer of the boot consists of a waterproof membrane-laminated polyester fabric. A more detailed picture of the boot's composition is shown in Figure 2.5.

Fig. 2.5 Material composition of the specific mountaineering boot model chosen for the thermal manikin tests (which corresponds to Model A).

The thermal conductivity and thickness properties of the materials, obtained through testing in accordance with UNI EN ISO 9920:2007 " *Ergonomics of the thermal environment — Estimation of thermal insulation and water vapour resistance of a clothing ensemble*" (ISO, 2007b) and UNI EN ISO 5084:1998 "*Textiles. Determination of thickness of textiles and textile products*" (ISO, 1997) standards, are reported in Table 2.4.

Sweat production was simulated with different amounts of water loaded onto the socks (0g, 5g, 15g, and 30g). The amount of water was indicated based on works that measured the regional sweating rate (Coull et al., 2021; Kuklane et al., 1998; Smith and Havenith, 2011; Taylor et al., 2009) and on previous studies on human participants simulating real-life activity with the same level of insulation worn (Bianca et al., 2024). In addition, for the larger amount of water (i.e., 30g), the different stages of the process of evaporation and condensation were investigated through a test of extended duration.

Area	**Property**	**Value**
Gaiter	Thermal Cond. (W/mK)	0.042
	Thickness (mm)	1.18
Upper side	Thermal Cond. (W/mK)	0.0389
	Thickness (mm)	3.97
Lower side	Thermal Cond. (W/mK)	0.0216
	Thickness (mm)	2.53
Tongue (upper)	Thermal Cond. (W/mK)	0.042
	Thickness (mm)	2.49
Tongue (middle-lower)	Thermal Cond. (W/mK)	0.031
	Thickness (mm)	3.25
Toecap	Thermal Cond. (W/mK)	0.026
	Thickness (mm)	3.76
Insole	Thermal Cond. (W/mK)	0.039
	Thickness (mm)	4.98

Table 2.4 Thermal conductivity and thickness for different regions of the boot.

2.2.2.1 Experimental Protocol

The socks were loaded by soaking in a water bath and then spun, removing free liquid, to avoid dripping. The spin speed was set at 800 rpm for five minutes. Afterwards, the socks were weighed, and water was added to reach the desired weight. This process was repeated until the target weight was achieved without any dripping. Socks and boots were weighed before and after the tests to observe their weight change. Each measurement of heat flux from the manikin was repeated three times until the power consumption was constant within $\pm 2\%$ for 10 minutes, as specified in ISO 15831:2004 "*Clothing. Physiological effects. Measurement of thermal insulation by means of a thermal manikin*" (ISO, 2004). The average environmental conditions were the following: ambient temperature ($T_{a,1}$) 10.0 ± 0.5 °C, relative humidity (RH_1) $50.0 \pm 1.8\%$, and wind speed (w_s) 0.4 ± 0.3 m/s. A longer test was carried out overnight with the greatest amount of water (30g) to analyse the whole process of water evaporation from the boot until all the water loaded in the socks was evaporated from the system. Based on the observation of different phases in the long-term test, four tests with incremental duration were carried out, at the end of which the weights of socks and shoes were measured in order to track the progression of moisture dynamics through the system over time. An isothermal test ($T_{a,2} = T_{manikin} = 34 \pm 0.6$ °C, $R_{H,2} = 12 \pm 0.7\%$, $w_s = 0.4$ m/s), with the highest amount of water loaded in the previous tests (30g), was carried out to avoid the contribution of convective, conductive and radiative heat transfer and to allow the test to be based solely on the evaporative heat flow. The test was repeated three times until the results were below the acceptable threshold for deviation (i.e., ±2% for 10 minutes). The relative humidity was chosen to give the same partial vapour pressure as the previous test conditions (i.e., creating the same driving force for evaporation), but at a different ambient temperature. The data were smoothed using a Savitzky-Golay filter. This method was proposed by Savitzky and Golay in 1964 and aims to reduce noise using local polynomial least squares approximations (Liu et al., 2016; Savitzky and Golay, 1964). The filter is controlled by two different parameters: the window size and the polynomial degree. Small window sizes and high polynomial degrees can result in noisy signals (flexible smoothing), while large window sizes and low polynomial degrees can result in distorted signals (rigid smoothing). A window size of 30 acquisitions, corresponding to a time span of 5 minutes, and a polynomial degree of 3 were selected for the data smoothing in this work.

2.2.2.2 Theoretical Background

Calculations have been performed according to the method proposed by Havenith et al. (Havenith et al., 2013, 2008).

1. **Dry Heat Loss**: This value was acquired for the clothed manikin in dry conditions

$$\mathrm{H_{dry}(Wm^{-2})} = \text{heat loss from the thermal zone} \tag{2.7}$$

2. **Apparent Heat Loss**: The “apparent heat loss” refers to the change in heat loss with respect to the dry test when the system is wet, as evaporation, increased wet conduction, and condensation may occur simultaneously.

$$\mathrm{E_{app}(Wm^{-2}) = H_{wet} - H_{dry}} \tag{2.8}$$

Since the temperature of the wet layer could not be controlled, a correction for the effective temperature of the socks was performed. In this way, Dry heat loss used in Eq. 2.7 was corrected for the effective temperature difference between skin and environment in the wet tests according to previous works (Toma et al., 2021; Wang et al., 2010).

$$\mathrm{T_{sk} = 34 - 0.0132 \cdot H_l \cdot A} \tag{2.9}$$

With $\mathrm{H_l}$ and A representing the heat loss in the foot area ($\mathrm{Wm^{-2}}$) and the surface area of the considered zone ($\mathrm{m^2}$). This led to the correct Eq. 2.7 as:

$$\mathrm{H_{dry,wet}} = \frac{\mathrm{T_{skin,WET} - T_{Ambient}}}{\mathrm{34 - T_{Ambient}}} \cdot \mathrm{H_{DRY}} \tag{2.10}$$

3. **Evaporative Heat Loss**: The latent heat loss was evaluated considering the amount of water leaving the system (socks-boots) in the time period:

$$\mathrm{E_{mass}(Wm^{-2})} = \frac{\mathrm{dMass}}{\mathrm{dt}}\mathrm{(gm^{-2}s^{-1}} \cdot \lambda\mathrm{(Jg^{-1})} \tag{2.11}$$

Where λ is the enthalpy of vaporisation of water and is evaluated as:

$$\lambda\mathrm{(Jg^{-1})} = 0.001 \cdot [2.792 \cdot 10^6 - 160\mathrm{T} - 3.43\mathrm{T}^2] \tag{2.12}$$

with T in K.

4. **Evaporative Cooling Efficiency**: The evaporative cooling efficiency was estimated by the ratio between the apparent and the latent heat loss (Eq. 2.8 and Eq. 2.11):

$$\eta_{\mathrm{app}} = \frac{\mathrm{E_{app}}}{\mathrm{E_{mass}}} \tag{2.13}$$

If η_{app} assumes the value of 1, the latent heat of evaporation is close to the theoretical value. Otherwise, it may be lower than 1 if the estimated latent heat is not taken from the body but from the environment (when evaporation takes place far away from the skin) or higher than 1 if the heat loss in the wet state is greater than the value estimated by liquid evaporation due to the presence of condensed water. Moreover, this factor gives information about the different contributions of the multiple pathways that could be undertaken by water within the system.

5. **Thermal Resistance** $\mathrm{R_{cT}}$: Dry thermal resistance was evaluated as follow (Wang, 2017; Wang et al., 2010):

$$\mathrm{R_{cT}(Km^2W^{-1})} = \frac{\mathrm{(T_{sk} - T_a)A}}{\mathrm{H_{DRY}}} \tag{2.14}$$

The main objective was to compare the dry thermal resistance with the thermal resistance measured under wet conditions in order to assess how the presence of water affects the insulation performance of the footwear.

6. **Evaporative Resistance** $\mathrm{R_{eT}}$: The evaluation of evaporative resistance R_{eT} was performed according to two different methods as already done by Wang et al. (Wang, 2017; Wang et al., 2010).

$$\mathrm{R_{eT,heat\,loss}(kPa\,m^2W^{-1})} = \frac{(\mathrm{p_{sk,s}} - \mathrm{p_a})\mathrm{A}}{\mathrm{H_{EVA}}} \tag{2.15}$$

$$\mathrm{R_{eT,mass\,loss}(kPa\,m^2W^{-1})} = \frac{(\mathrm{p_{sk,s}} - \mathrm{p_a})\mathrm{A}}{\lambda \frac{\mathrm{dM}}{\mathrm{dt}}} \tag{2.16}$$

Where the saturated vapour pressure at skin temperature was predicted according to ISO 7933 "*Ergonomics of the thermal environment. Analytical determination and interpretation of heat stress using calculation of the predicted heat strain*" (ISO, 2023).
The use of two methods is necessary because the evaporation process does not always occur solely at the expense of the manikin's heat.
When a portion of the water evaporates using heat absorbed from the environment (for example, from the surrounding air or surfaces), not all the evaporation contributes to cooling the manikin. In such cases, the mass loss method may overestimate the actual evaporative heat loss, causing the two methods to diverge.
Conversely, if evaporation occurs entirely at the expense of the manikin's thermal energy, the evaporative heat loss and the latent heat associated with mass loss are equivalent, and the two methods yield similar results.
Therefore, comparing the two values provides insight into the actual energy pathways involved in evaporation and helps assess how effectively the footwear allows evaporative cooling under the tested conditions.

7. **Permeability Index** $\mathrm{i_m}$: since the boots were impermeable to external water penetration, an additional parameter was used to quantify their ability to manage moisture. The calculation follows the work by (Woodcock, 1962) and the International Standard ISO 9920:2007 (ISO, 2007b):

$$\mathrm{i_m} = \mathrm{S}\frac{\mathrm{R_{cT}}}{\mathrm{R_{eT}}} \tag{2.17}$$

Where S is a conversion factor equal to 60 (PaK^{-1}), representing the thermal to evaporative resistance of an air layer as thick as the insulation material. According to the original definition, (Woodcock, 1962) using the ratio between the evaporative and the convective heat transfer coefficient, theoretically, the permeability index should range between 0 and 1. A value of 0 implies a system with no evaporative transfer, a value of 1 means a system with no resistance to evaporative transfer, given the same thermal insulation. However, a value of 1 means the clothing has the same vapour resistance (Evaporative Heat Transfer Coefficient) as an air layer of the same thickness with a lower thermal resistance compared to that of the garment. However, as the resistances in Eq. 2.14 also include a radiative component of heat transfer through clothing, the index tends to range between 0 and 0.6 (Goldman, 1974; Havenith et al., 1990; Huang, 2006).

8. **Water Vapour Absorption (WVA)**: Since a wet layer (the sock) was imposed between the skin and the boot, water sorption was supposed to happen from the sock to the shoe. This amount was evaluated as water vapour absorption (WVA) (Schols et al., 2004).

$$\mathrm{WVA(gh^{-1})} = \frac{\mathrm{M_t - M_0}}{\Delta \mathrm{t}} \tag{2.18}$$

Where $\mathrm{M_t}$ is the mass of the boot after the test, and $\mathrm{M_0}$ is the mass of the boot before the test.

2.2.2.3 Statistical

The statistical analysis was performed with Python (version 3.12.0). The most used libraries were:

- *scipy.stats*: P. Virtanen, R. Gommers, T. E. Oliphant, M. Haberland, T. Reddy et al., and SciPy 1.0 Contributors. (2020) SciPy 1.0: *Fundamental Algorithms for Scientific Computing in Python.* Nature Methods, 17(3), 261-272.
- *statsmodel.api*: Seabold, S., & Perktold, J. (2010). *statsmodels: Econometric and statistical modeling with Python.* In the 9th Python in Science Conference.

2.3 Result and Discussion

2.3.1 Human Tests Results

The *explorative* experimental campaign confirmed that the big toe is consistently the area of the foot most affected by vasoconstriction. Figure 2.6 shows the temperatures measured on the toes during the three different test protocols concerning Campaign 2 - Real Expedition protocol. The vertical dashed lines indicate the different test phases as described in the protocol details in Section 2.1.

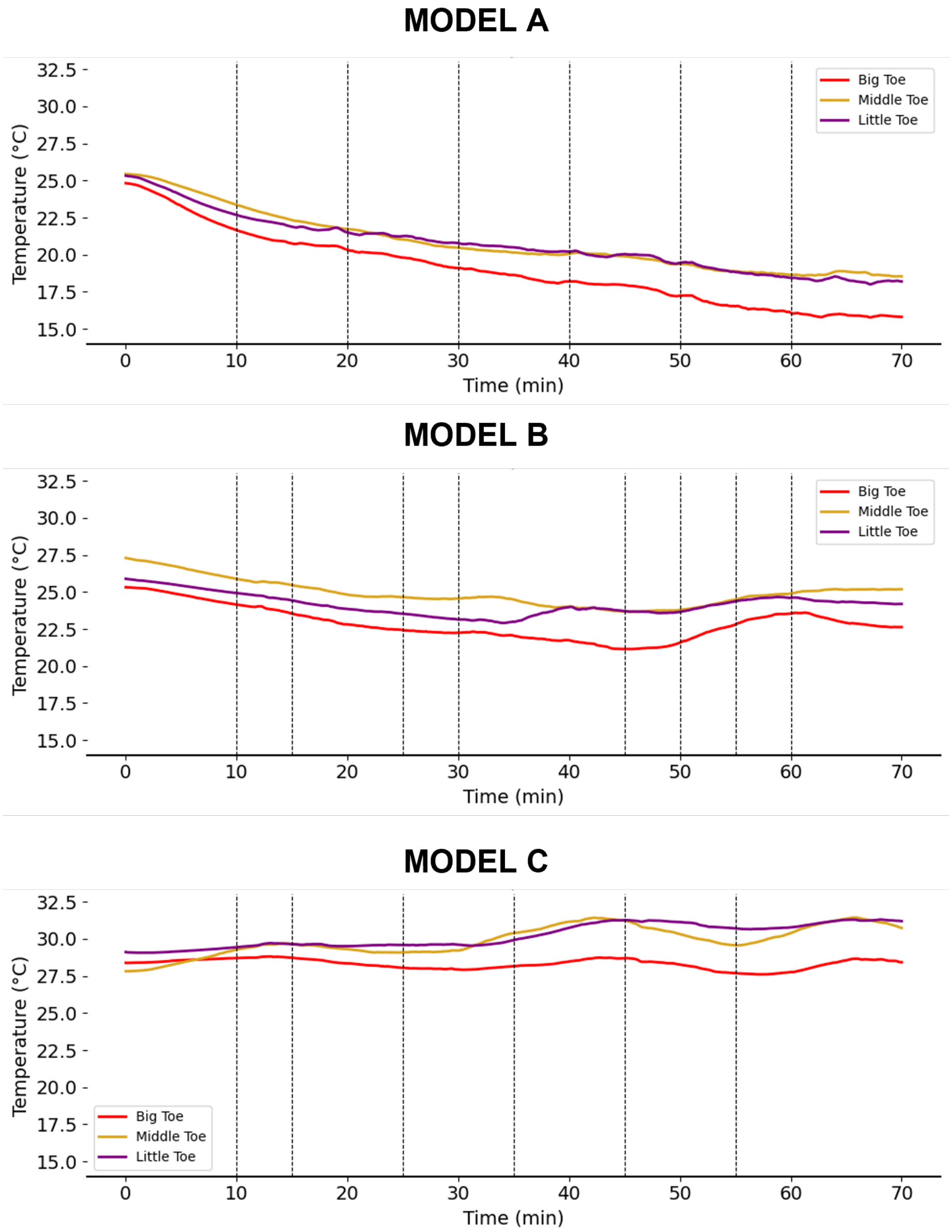

Fig. 2.6 Hallux, Middle finger, and Little finger temperature across the tests in the three different protocols.

Another relevant outcome of the first experimental campaign was the quantification of the metabolic rate associated with typical alpine activities under extreme environmental conditions. Evidence of such data in the literature appears to be limited.

The use of reliable metabolic rate values will be essential in the subsequent steps of this research, particularly to quantify the required level of insulation in the studied conditions. Indeed, the level of physical activity has been confirmed to be a crucial factor influencing thermoregulatory responses.

Figure 2.7 illustrates the metabolic rate measured during protocols B and C, while protocol A was comparable to protocol B in terms of physical exertion and has therefore been omitted.

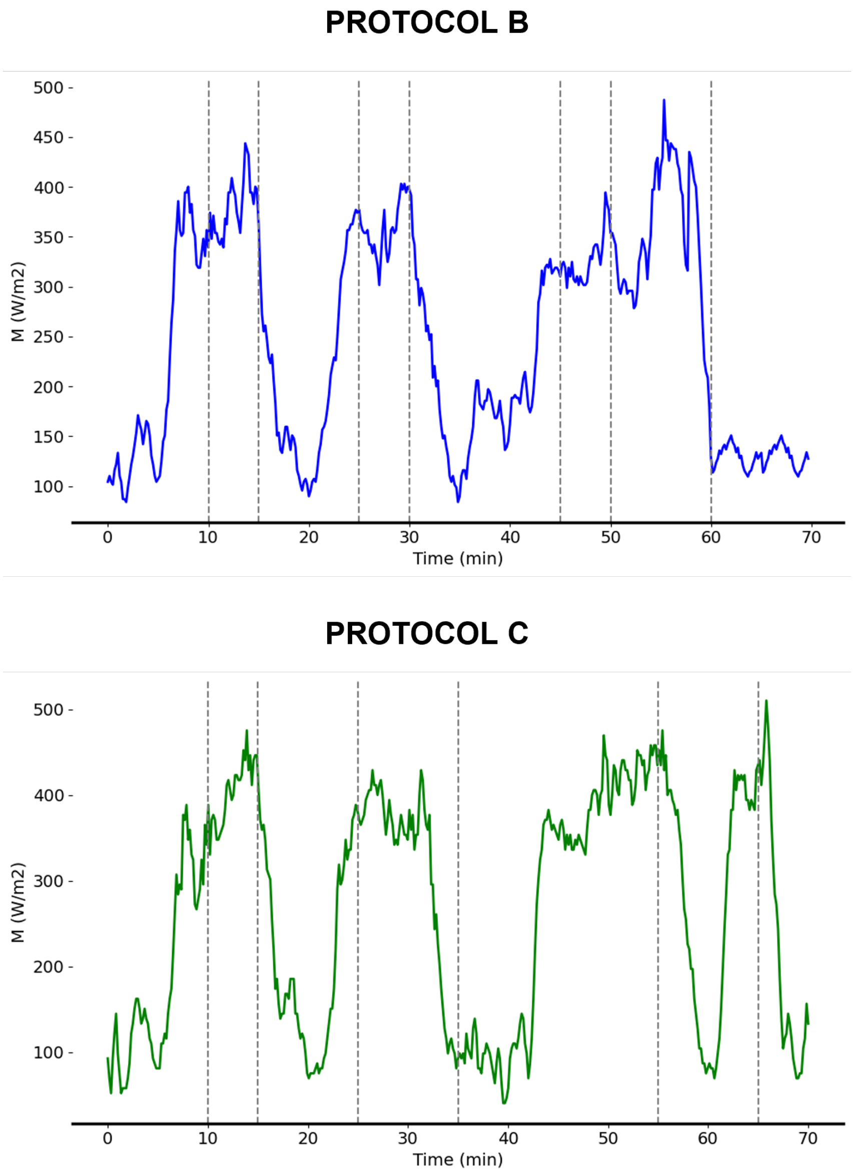

Fig. 2.7 Plot of the metabolic rate, averaged across the three subjects involved in each experimental campaign.

The insulation values determined were compared with the IREQ (Insulation REQuired) value defined in the International Standard ISO 11079:2007 "*Ergonomics of the thermal environment. Determination and interpretation of cold stress when using required clothing insulation (IREQ) and local cooling effects*" (ISO, 2007a), which takes into account the environmental conditions and the activity level. IREQ represents the clothing insulation required under specific environmental conditions to maintain the body in thermal equilibrium while keeping body and skin temperatures within acceptable limits. It can be identified as a measure of cold stress, integrating the effects of environmental conditions. It also serves as a method for analysing the impact of the thermal environment and metabolic activity on the human body (in line with the project's core concept), a means to specify clothing insulation requirements precisely, and a tool to monitor and measure the heat balance parameter for design improvement and optimisation.

To determine the IREQ value, the metabolism for the different activities was assessed in accordance with the standard ISO 8996:2021 (ISO, 2021). Following the standard, the metabolic rate (MR) of a single activity was first estimated using the procedure *"Evaluation of the metabolic rate at level 2, Observation"*, already described in detail in Section 2.1.

As can be seen from Table 2.5, the insulation requirements for the different activities carried out were met. Due to the similarity of the conditions of use and test protocols, Models A and B had comparable insulation values for both clothing and footwear. The correct match between the selected garments and the environmental and activity conditions ensured that the observed thermoregulatory responses could be interpreted with greater certainty. In other words, the appropriate insulation minimised confounding factors and allowed us to isolate and better understand the physiological response to cold exposure and physical exertion under controlled conditions.

As expected, the only condition in which the isolation requirements were not met was the one in which participants were asked to stand still. This scenario, characterised by minimal metabolic heat production, resulted in a higher risk of reaching critical temperature thresholds. For this reason, it represented the most thermally challenging situation and required more in-depth investigation to fully understand the associated physiological responses and potential safety concerns.

Table 2.5 Values of IREQ evaluated according to ISO 11079:2007 compared to the insulation worn in protocols A/B and C. All the values are expressed in [Km^2W^{-1}]

Test	Activity	IREQ	Clothing	Boots
MODEL A/B	Rest	$0.682 < IREQ < 0.729$	0.202	0.207
	Walking	$0.233 < IREQ < 0.279$		
	Climbing	$0.098 < IREQ < 0.124$		
MODEL C	Rest	$0.915 < IREQ < 0.977$	0.446	0.404
	Walking	$0.341 < IREQ < 0.388$		
	Climbing up a ladder	$0.217 < IREQ < 0.264$		

2.3.1.1 Effect of Different Physical Activities

An analysis was carried out to investigate the effect of physical activity on thermoregulation, keeping the insulation level of clothing and the ambient temperature constant. The data used for this analysis were collected under comparable conditions, differing only in activity level, specifically from Campaign 3 – Worst Case Scenario, and Campaign 4 – Temp & Activity (see Table 2.2). Figure 2.8 clearly shows the influence of physical activity on thermoregulation. The temperature of the big toe consistently approached the critical threshold at rest, while a significant initial drop in temperature was observed during exercise, followed by a stabilisation phase, which is probably due to physiological adaptation mechanisms to the cold.

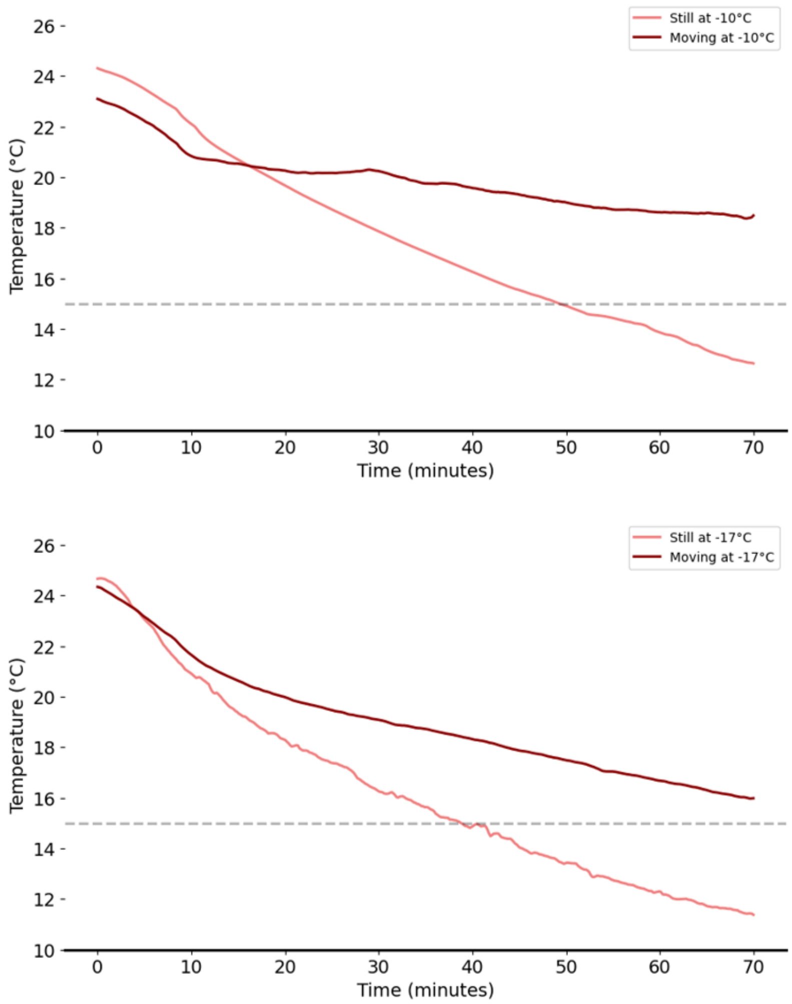

Fig. 2.8 Big Toe temperature comparison (mean across participants) between still and moving protocols at -10 °C (top) and -17 °C (bottom). The gray dashed line indicates the 15 °C threshold.

Considering the variability between campaigns and the non-normal distribution of the data, a permutation t-test was performed using the minimum big toe temperature reached by each participant as a benchmark measure. The results are summarised in the violin plot Figure 2.9.

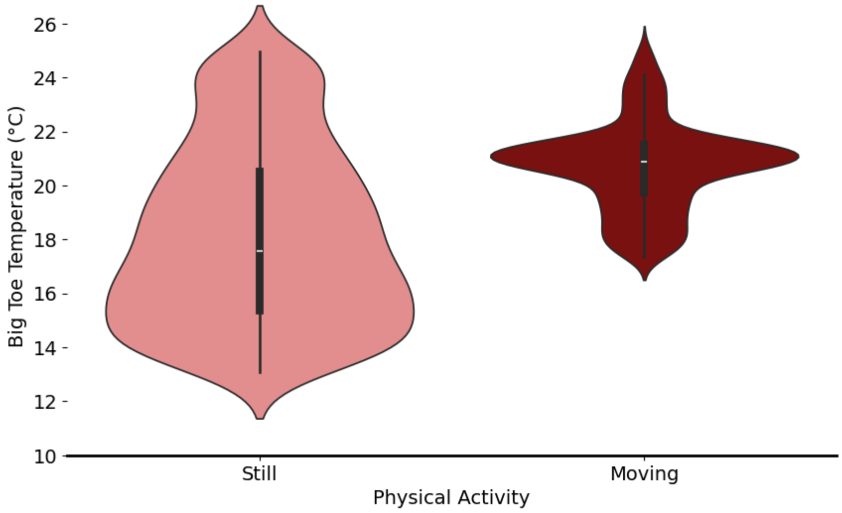

Fig. 2.9 Big Toe temperature comparison in two different protocols.

As shown in Figure 2.8 that compares the big toe time series, the effect of physical activity on thermoregulation was statistically significant at -10°C (p = 0.047), while the effect was less significant at -17°C (p = 0.177). This difference is probably due to the fact that physical activity at -10°C improves blood circulation and helps to keep the big toe temperature higher despite some peripheral vasoconstriction. In contrast, at -17°C, vasoconstriction is more pronounced in both groups (still and moving) and severely restricts blood flow in the extremities. Under these more extreme conditions, the vascular response to cold dominates, emphasising the maintenance of core temperature and reducing the relative effect of physical activity on peripheral temperature.

In view of the strong coincidence of several factors that could weaken the statistical significance of the test, both the median and the standard deviation of the minimum big toe temperatures were calculated for the two conditions.

In the still condition, the median of the minimum value was 13.91°C with a standard deviation of 4.63°C, while in the exercise phase the median increased to 18.68°C and the standard deviation decreased to 4.23°C. This observation suggests not only that physical activity in general helps to maintain higher toe temperatures, but also that the participants' thermal response was more consistent in the moving situation. In contrast, stillness resulted in a broader range of responses, likely reflecting individual differences in peripheral vasoconstriction and cold tolerance. The same concept is reflected in the violin plots in Figure 2.9, which show a greater deviation and a lower

mean value in the case of stillness compared to the counterpart moving condition. In addition, the same graph clearly shows that the distribution of values is much more concentrated than in the case of standstill, which appears broader and more distributed in the lower part (lower values, strong vasoconstriction).
These results reinforce the idea that physical activity plays a stabilising role in peripheral thermoregulation under cold stress, although statistical significance is not achieved due to sample variability and limited power.

2.3.1.2 Effect of Different Ambient Temperatures

An analysis was carried out to assess the effects of ambient temperature on thermoregulation, keeping both clothing insulation and activity level constant. The data used for this comparison were collected under equivalent conditions, differing only in ambient temperature, specifically from Campaign 3 – Worst Case and Campaign 4 – Temp & Activity (see Table 2.2). Figure 2.10 clearly shows the influence of the ambient temperature on the thermoregulatory response.

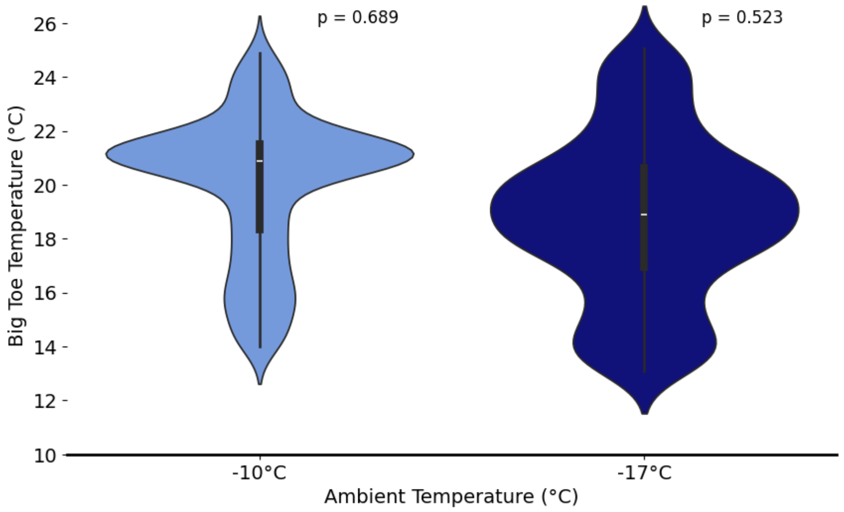

Fig. 2.10 Big Toe temperature comparison in two different ambient temperatures.

The highest mean big toe temperature was observed at -10 °C both at rest and during exercise, suggesting that milder environmental conditions led to warmer peripheral temperatures overall. This confirms the previously discussed trend that colder environments elicit a more pronounced vasoconstrictive response, with a wider distribution of values that are more concentrated at the lower range.

Although it is generally assumed that lower ambient temperatures cause more pronounced peripheral cooling through increased vasoconstriction, the shown results suggest that the thermoregulatory response is not strictly linear, but progressively increases with decreasing ambient temperature, possibly reaching a saturation threshold beyond which further cooling causes only minimal additional constriction. At –10 °C, the mean minimum big toe temperature was 13.91 °C (SD = 4.25), while at –17 °C it dropped to 12.95 °C (SD = 4.23). Though the difference was not statistically significant, this trend is consistent with the concept of non-linear physiological adaptation: Once maximum vasoconstriction is reached, further decreases in ambient temperature lead to diminishing effects. This interpretation is consistent with the literature, which suggests that thermoregulatory responses such as vasoconstriction are driven by threshold-based control mechanisms with potential saturation at extremes (Cheng et al., 1995; Cheung, 2015).

2.3.1.3 Effect of Different Boots Insulation

Although the thermal resistance values of Model D and Model E did not differ significantly (as shown in Figure 2.11), the distribution of big toe temperatures under the two activity conditions (standing and walking) showed subtle but potentially significant differences.

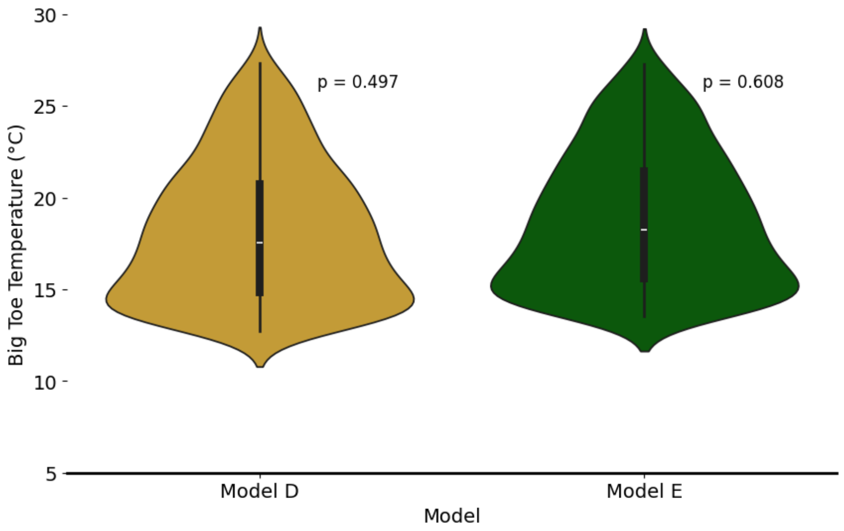

Fig. 2.11 Big Toe temperature comparison with two different boot models.

While the permutation tests yielded no statistically significant results ($p = 0.497$ for the standing condition and $p = 0.608$ for the walking condition), the descriptive statistics indicate a slightly better thermoregulatory performance for Model E. Specifically, Model E showed a higher mean value of the minimum big toe temperature reached (13.50°C vs. 12.72°C) and lower between-subject variability (standard deviation of 1.72°C vs. 2.47°C). This lack of significance is likely due to the high similarity between Model D and Model E, which is also reflected in their very close insulation values ($R_{cT} = 0.193$ vs. $0.195\ m^2KW^{-1}$).
To further interpret these differences, an additional analysis of the mean skin temperature measured during the same protocols was performed. This allowed us to verify whether the global heat load experienced by the participants was comparable between the two boot configurations. The results showed no statistically significant difference in skin temperature ($p = 0.846$ for the resting condition and $p = 0.765$ for the walking condition), with almost identical median values (26.02 °C for Model D and 26.13 °C for Model E) and similar standard deviations (0.85 °C vs. 1.05 °C).
These results support the interpretation that the overall thermal load was similar and that the observed differences in big toe temperature were most likely due to local differences in insulation effectiveness, particularly in the retention of peripheral heat. Although the differences were small, they suggest that local design features of the insulating elements may influence the maintenance of peripheral temperature, especially under low activity or static conditions, where heat loss is more pronounced.

2.3.1.4 Analysis of the Thermoregulatory Response

To gain deeper insights into the human thermoregulatory response, a dedicated analysis of the temperature time series of the big toe collected in all experimental protocols was carried out. Each individual curve was segmented into time windows of six data points, corresponding to an interval of one minute, with an acquisition frequency of one data point every 10 seconds. For each segment, the difference between the average temperature of the current and previous window was calculated to identify trends, abrupt changes, or recurring patterns in the thermal response.
The results of this analysis are shown in Figure 2.12.

For clarity, the labelling of each graph follows the previously adopted convention: firstly, the boot model used in the specific protocol (e.g. A, B...); secondly, the

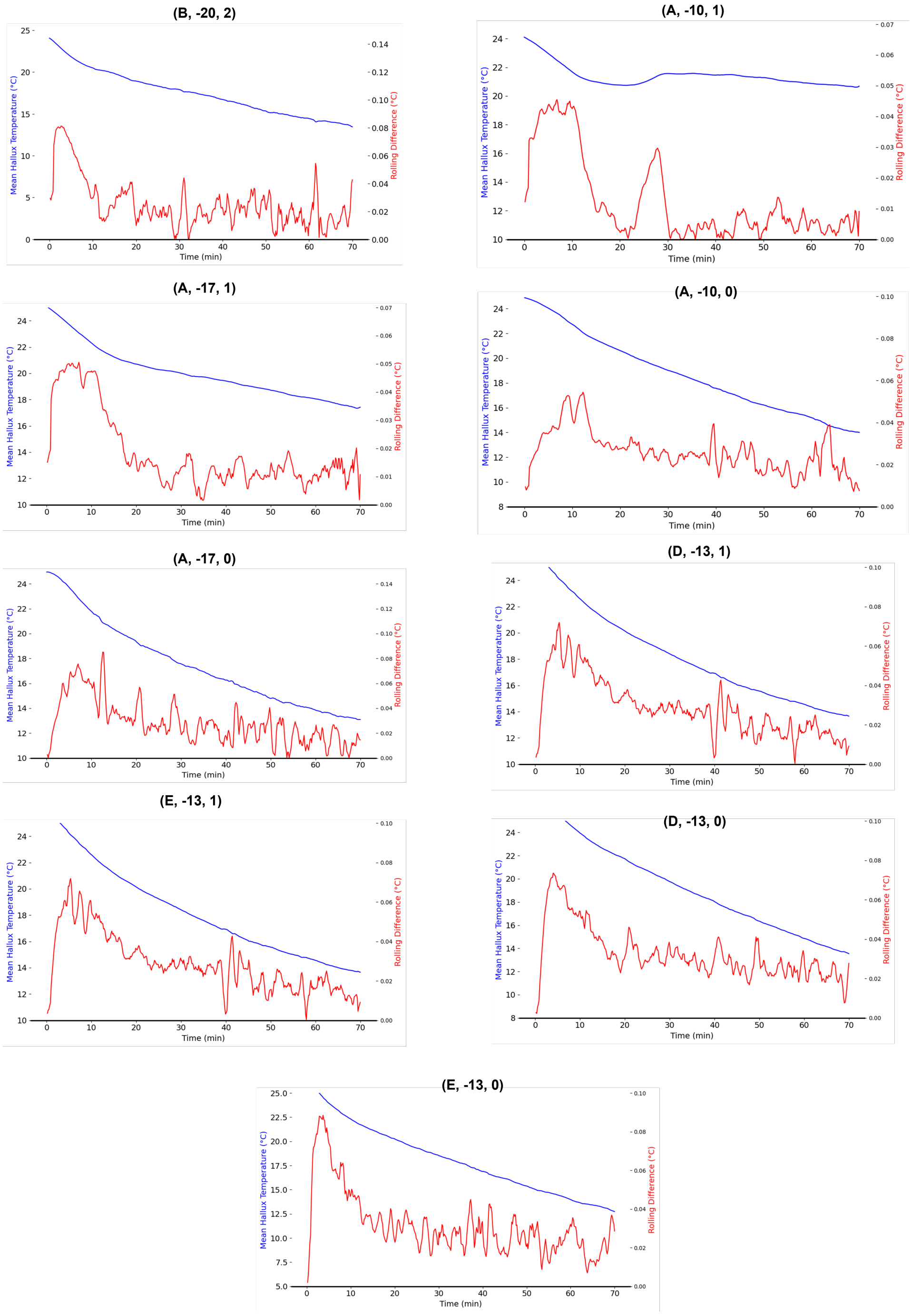

Fig. 2.12 Analysis of the temperature curves of the big toe using the time window method. The blue curve represents the mean temperature of the participants, while the red line shows the rolling difference. Each graph is labelled according to the scheme (Model, Ambient Temperature, Activity Level).

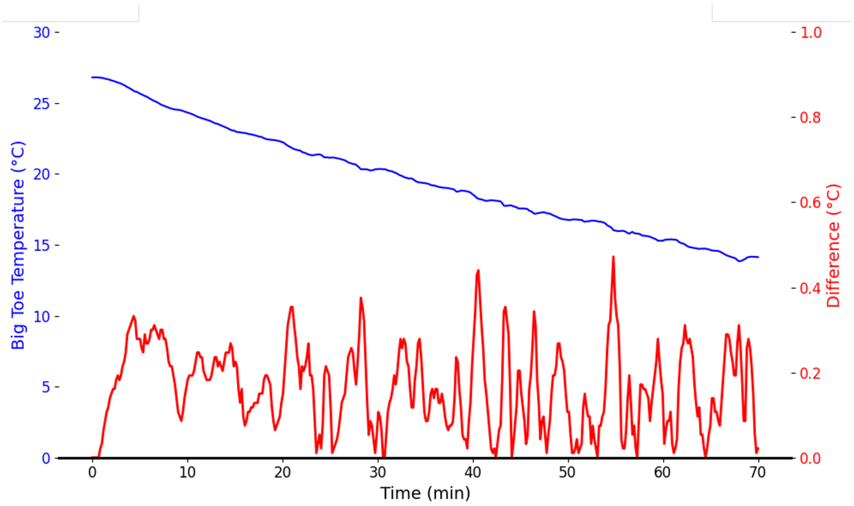

Fig. 2.13 Example of a noisy trend for a participant from the test case (A, -17, 0), possibly indicating CIVD events.

ambient temperature at which the test was performed (e.g. -20°C, -10°C...); and finally, the activity level associated with the protocol (1 = rest, 2 = light effort, 3 = high effort).

To enhance readability, the scale of the y-axis was adapted for both the big toe temperature and the rolling difference for each protocol. This choice was made to better emphasise the dynamics within the curve and pattern recognition, rather than allowing a direct comparison of absolute values between conditions (these have already been explored in detail in the previous sections).

In all conditions, a notable spike was consistently observed in the first ten minutes. This feature was interpreted as an effect of initial cold-induced vasoconstriction (CIVC), a well-known thermoregulatory response triggered by sudden cold exposure. In some protocols, such as (A, -17, 0), the harshest protocol combination, this response appeared to be more erratic and exhibited considerable variability. An even clearer example of such behaviour is shown in Figure 2.13.

This specific trend has been attributed to another important physiological mechanism involved in the cold response: cold-induced vasodilation (CIVD) (Daanen and van Ruiten, 2000; Flouris et al., 2008; O'Brien, 2005; Youssef et al., 1996). In such cases, after an initial drop in skin temperature due to vasoconstriction, the body attempts to preserve tissue integrity in the extremities by temporarily increasing blood flow through dilatation of AVAs (arteriovenous anastomoses), direct connections between small arteries and veins that bypass the capillary bed. This process can lead to a cyclical rise and fall in skin temperature that typically begins about ten minutes after exposure to cold.

This analysis proved to be valuable not only for a better understanding of the physiological thermoregulation mechanisms under the specific environmental and footwear conditions studied, but also for revealing recurring patterns in the temperature curves. Despite the variability in absolute temperature values due to different boundary conditions, the time series consistently showed similar trends. This recurring behaviour suggests an underlying regularity in the thermal response and opens the door for a data-driven approach.

In particular, the presence of identifiable patterns supports the development of predictive models capable of estimating the evolution of big toe temperature over time based on known input conditions such as ambient temperature, footwear characteristics, and physical activity.

2.3.2 Thermal Manikin Results

The results of the sweat production at the dorsum of the foot and big toe in the high-exertion condition (i.e., the "*alpinism*" protocol) are shown in Figure 2.14. As the sensors measured relative humidity (RH), the values were converted into absolute humidity (AH), expressed in g/m^3, to facilitate interpretation. The conversion was performed using the following standard psychrometric formula proposed by (Alduchov and Eskridge, 1996):

$$\mathrm{AH} = \frac{6.112 \cdot \exp\left(\frac{17.67 \cdot \mathrm{T}}{\mathrm{T}+243.5}\right) \cdot \frac{\mathrm{RH}}{100} \cdot 2.1674}{273.15 + \mathrm{T}} \tag{2.19}$$

where T is the local skin temperature in °C, and RH is the relative humidity in %.

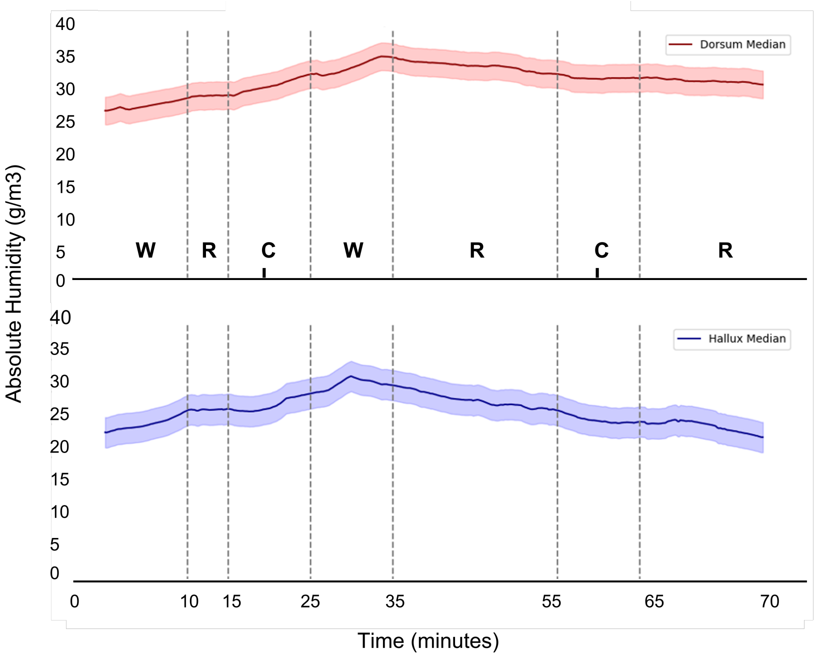

Fig. 2.14 Absolute humidity at the dorsum and big toe during the "alpinism" protocol (Protocol B). The shaded ribbon represents the 90% confidence interval.

As expected, the amount of moisture produced during physical activity was significantly higher compared to the stillness condition ($p < 0.05$). Although pre-test hydration levels were not strictly controlled, participants were instructed to maintain consistent daily habits, including hydration routines, to reduce variability in individual thermoregulatory responses.

Considering that the sweat accumulation was substantial, as supported by literature values (Coull et al., 2021; Kuklane et al., 1999; West et al., 2019), a further investigation was conducted to evaluate the impact of moisture on thermal insulation. Thermal manikin tests were therefore performed with wet and dry configurations to quantify the effect of moisture on the thermal resistance of the footwear system.

The heat losses in the foot area of the manikin, measured at 10°C and 50% relative humidity, are shown in Figure 2.15.

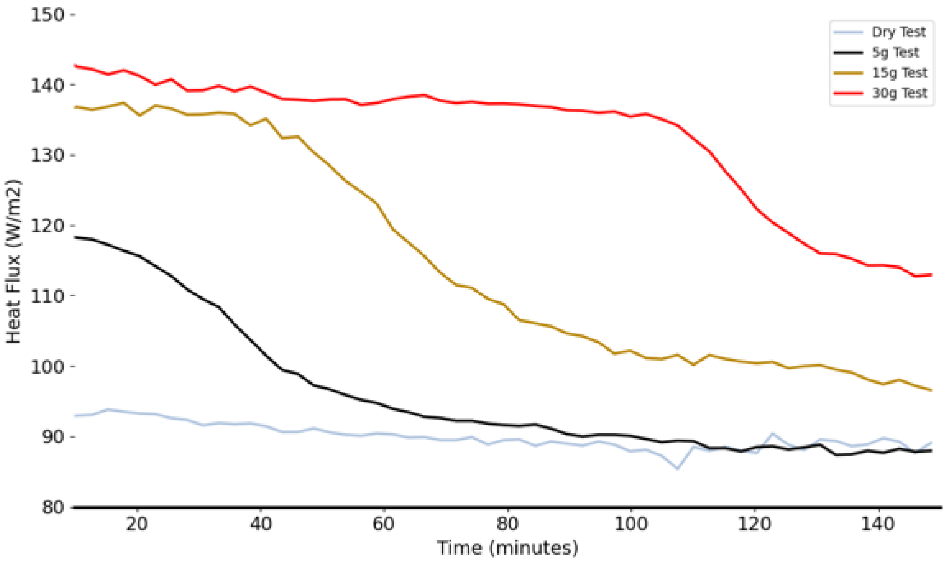

Fig. 2.15 Average Heat Flux for the different water contents in the different phases for the foot area.

At first glance, a net increase in heat loss was observed in the wet tests, as the amount of water in the sock was higher. However, this aspect is not the only effect of moisture: different amounts of water indeed are associated with a different shape of the heat loss curve. A clustering algorithm was applied to highlight the various phases. The method was based on the K-Means approach, which identified three clusters, namely three different phases in the curves: a first plateau (stable phase), which is more extended as more water is loaded onto the socks, a declining phase, and a second plateau (second and final stable phase). The curve relating to the test with the lowest amount of water (i.e., 5g) did not show the first plateau but an immediate drop to a lower, stable value comparable to the curve of the dry test. In the experiment involving 5g of water loaded into the socks, the presence of only a few grams of free water prevents the establishment of a constant evaporation rate, leading to the formation of the initial plateau phase.
In addition, the decreasing phases of the 15g and 30g curves were analysed to highlight their slopes with a linear regression: The 30g test showed a steeper fall phase than the 15g which has rather similar values to the 5g curve ($R^2_{30g} = 0.9843$, $m_{30g} = -0.3937$; $R^2_{15g} = 0.9554$, $m_{15g} = -0.294$; $R^2_{5g} = 0.9495$, $m_{5g} = -0.2537$).

Table 2.6 shows the amount of water loaded in the socks, the weight of the socks and boots at the end of the tests, as well as the percentage of evaporated water. The data correspond to the average of three tests. The high percentage of water remaining in the boots at the end of the test highlights their low permeability index .

Loaded (g)	**In socks at the end (g)**	**In boots at the end (g)**	**In socks (%)**	**In boots (%)**	**Evaporated (%)**
5.86 ± 0.16	0.00 ± 0.06	4.01 ± 0.58	0	68	32
15.73 ± 0.69	1.01 ± 0.30	10.67 ± 1.76	6	68	26
30.07 ± 0.19	0.77 ± 0.91	21.00 ± 0.29	2	70	28

Table 2.6 Average water content measured at the end of each test across the three replicates.

The presence of extended plateau regions and abrupt variations in the heat flux curves can be explained by considering the spatial distribution and phase of the moisture within the system, rather than the total water content alone. During the initial plateau phase, the heat flux remains relatively stable despite the presence of moisture, as evaporation is primarily sustained by free water within the socks, which maintains a quasi-constant drying rate. This behaviour is consistent with the constant-rate drying phase described in the literature (Heinisch et al., 2019).

The subsequent steep decline in heat flux corresponds to the progressive decrease in unbound water in the socks and its displacement into the footwear layers through condensation. This transition marks a shift in the dominant heat and mass transfer mechanisms, as the location of evaporation moves away from the sock–skin interface. As a result, the thermal response changes rapidly, producing the observed transient behaviour.

In the later phases of the test, although a non-negligible amount of water remains trapped within the boots, the heat flux gradually stabilises and approaches values comparable to the dry condition. This indicates that moisture retained in the footwear does not necessarily contribute to additional heat loss once active evaporation from the sock region has finished. Instead, the system enters a dynamic equilibrium in which evaporation occurs predominantly from the boot layers at a reduced rate, with a limited impact on the overall thermal resistance.

These observations highlight that extended stabilisation phases in the heat flux curves should be interpreted as dynamic equilibria governed by the location and phase state of moisture, rather than as artefacts or measurement uncertainties. The results further confirm that the evaporation–condensation cycle plays a central role in modulating the thermal response of footwear systems, and that changes in heat loss are strongly dependent on where evaporation occurs within the system. For each phase, E_{app} was also calculated to observe the contribution of evaporative heat loss and the contributions of wicking (which transports moisture away from the skin where it evaporates at the expense of the environment (Aoyagi et al., 1996) and condensation. In the first phase, the E_{app} value for the 15g test was 47.87 W/m^2, while for the 30g test, it was slightly higher at 50.96 W/m^2. This difference highlights the increased evaporative heat loss associated with the larger water content in the 30g test. Nevertheless, there is no noticeable difference in terms of initial heat loss between the two tests, despite the water content being almost twice as high in the 30g test. Nevertheless, there is no noticeable difference in terms of initial heat loss between the two tests, despite the water content being almost twice as high in the 30g test. When water spreads in a cotton fabric, it tends to fill the hydrogen bonds on the fibre surface before filling the free volume in between the fibres. Once the water-bound fibres of the material are saturated, the free water is displaced by gravity and capillary force (Fohr, 2015). Cotton has excellent absorption properties reflected in significantly lower moisture transport (Das et al., 2007; Li et al., 2008), and the wetting density is distributed over two different areas: the intermediate fibres, which are saturated first, and the intermediate yarn. Water transport in porous media like cotton can be initially described by Fick's law of diffusion, expressed as:

$$J[\mathrm{kg}\cdot\mathrm{m}^{-2}\cdot\mathrm{s}^{-1}] = -D\frac{\partial C}{\partial x} \tag{2.20}$$

where J is the diffusion flux, D (in $\mathrm{m}^2\cdot\mathrm{s}^{-1}$) is the diffusion coefficient, C (in $\mathrm{kg}\cdot\mathrm{m}^{-3}$) is the concentration, and x (in m) represents the spatial coordinate. This law governs the movement of water molecules from regions of higher concentration to regions of lower concentration. The diffusion coefficient of water in air is approximately 0.239 cm^2/s, while in cotton, it is significantly lower, around 10^{-7} cm^2/s. This difference highlights the rapid evaporation of free water compared to the slower diffusion of bound water within the fibre matrix. However, for hydrophilic fibres such as cotton, water diffusion follows a non-Fickian behaviour. In the first stage, free water evaporation adheres to Fickian dynamics as previously described, characterised by relatively fast moisture transport. In the second stage, once free water has left the system, water trapped in the microporous fibre network and bound by hydrogen bonds dominates the process (Das et al., 2007). This results in a much slower moisture release, governed by interactions between bound water and the fibre matrix, often described by a relaxation-driven diffusion mechanism. The swelling of hydrophilic fibres during water absorption further complicates this behaviour, as the fibre matrix undergoes structural changes that influence water mobility and diffusion pathways.

In this context, free water evaporation is responsible for the first plateau in Figure 2.15, which is longer for the 30g test (compared to the 15g and 5g tests), as more free water is present in the 30g test. In this phase, free water, which has the highest mobility, evaporates from the fibre matrix, causing an initial stable phase with a higher heat loss compared to the dry test (Wissler and Havenith, 2009). Once free water has left the system, the microporous trapped water begins to interact with the hydrogen bond water, reducing the mobility of both (Ji et al., 2016). The R_{cT} values for each stage and condition are shown in Table 2.7. Considering an R_{cT} value of 0.276 (m2KW^{-1}) for the dry test, the deviations from this value are also given. Since there is no effective first stable phase for the 5g test due to the negligible amount of free water (see Fig. 2.15), the value for this condition is omitted. In summary, the sharp difference between the diffusion coefficients of water in air and cotton underlines the rapid evaporation of free water, while the hydrophilic nature of the cotton fibres introduces a non-Fickian behaviour that slows down the subsequent stages of moisture transport.

Test	$R_{cT,1ph}$	$R_{cT,2ph}$	$\Delta R_{cT,1ph-DRY}$ (%)	$\Delta R_{cT,2ph-DRY}$ (%)
5	NA	0.275	NA	-0.36
15	0.178	0.243	-35	-12
30	0.175	0.230	-37	-17

Table 2.7 Value of Thermal Resistance for each amount of water in the first (1ph) and second stable phase (2ph) added and their deviation from the Dry test for both phases

As shown in Table 2.7 during Phase 1, the presence of free water leads to a marked decrease in thermal resistance, as the high evaporation rate removes a significant amount of heat from the system. In contrast, in Phase 2, where evaporation becomes progressively slower, the change in thermal resistance is noticeably less pronounced. In order to observe the paths travelled by the water during the entire process more closely, a longer test (approx. 16 hours) was carried out in which the dry-wet heat loss of the system with the highest amount of water in the socks (30 g) was investigated. The results are shown in Figure 2.16.

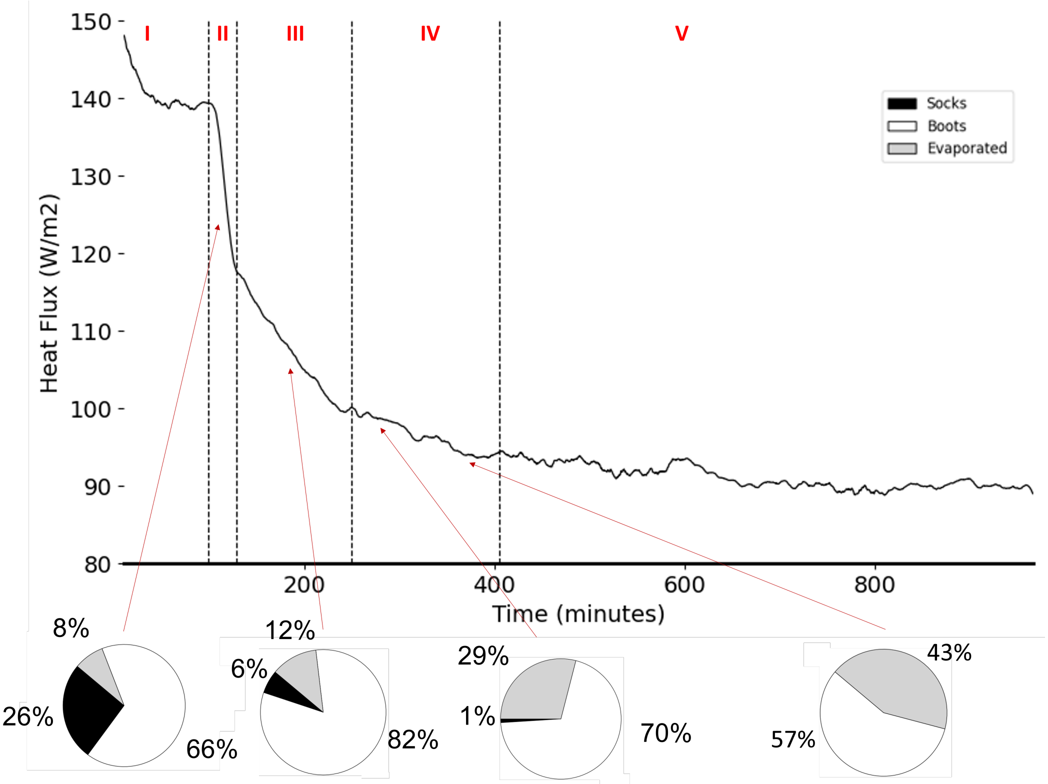

Fig. 2.16 Overnight test with 30g water-loaded socks was conducted, with identified phases shown. The test was repeated four times and halted at set time intervals. The system (socks and boots) was weighed to monitor WVA, as indicated in the four pie charts.

As with the previous results, the data was filtered and clustered, defining five clusters. In this way, five different phases were identified: an initial stable phase (i.e. the plateau phase) up to 100 minutes, a second steep decline up to 121 minutes, a third phase up to 249 minutes, a fourth phase up to 405 minutes, and finally a steady flat phase until the end of the test. This result is consistent with the data provided by Heinisch et al. (Heinisch et al., 2019) who defined the drying process as composed of different stages: an initial warm-up phase, a following phase with a constant drying rate in which the unbounded water leaves the system, and a final period of slower drying rate. As shown in the pie chart in Figure 2.16, once most free water has evaporated from the socks and entered the boots through the condensation process (i.e., 20 g after 235 minutes), evaporation from the boots occurs and transports the water out of the system. Based on the results from the 16-hour test, individual tests were subsequently carried out for each identified phase. This approach allowed for a detailed analysis of the dynamics governing each stage of water transport and heat exchange, providing a clearer understanding of the distinct mechanisms observed in different phases of the drying process.

The percentage of water in the socks, in the boots, and the amount evaporated at the end of each phase is shown in the pie chart in Figure 2.16.

Water was progressively displaced from the socks to the boots, where it hardly evaporated. In addition, another interesting aspect emerged: although there was still a non-negligible amount of water in the boots after the fourth phase (17g, 57% of the initial amount), no such remarkable changes in heat loss were observed compared to the dry test. Indeed, the thermal resistance did not change significantly from the beginning to the end of the fifth phase (when weighing showed that almost all the water had evaporated). The comparison between R_{cT} in the dry test and the value determined in the last part of the long-term overnight test is shown in Table 2.8.

Test	$R_{cT}(Km^2W^{-1})$
Dry Test	0.276
Overnight Test (5^{th} Phase)	0.255

Table 2.8 Dry Thermal Resistance values in the dry test and in the 5th phase of the overnight test

The difference between the two values is less than 8%. This result is in contrast to the findings of Kuklane and Holmer (Kuklane and Holmér, 1997), according to which the combined effect of movement and perspiration can reduce insulation properties by up to 40%. However, in their case, sweat was released from the manikin through three artificial sweat glands (one in the toes). Our tests indeed ensured a more even distribution of the water so that dripping could be ruled out. This meant that the whole foot was considered in terms of thermal insulation and not the individual foot zones, which may differ due to the composition of the boots and specific insulation (Kuklane et al., 2005). Another reason the difference is not clearly visible is that, when the water is no longer in direct contact with the warm manikin surface, it does not evaporate rapidly; therefore, the evaporation effect is less noticeable. However, given the numerous differences in the experimental setup, the results are not comparable.

The amount of evaporated water corresponding to the first plateau (i.e., after 100 minutes) can be considered completely negligible compared to the transport of water between the socks and the boots, probably due to both an absorption process in the permeable part of the boots and, mostly, to condensation in the inner part of the boots. The trend seems to be confirmed until a major reversal in the third phase, when the proportion of evaporation starts to increase. These findings are supported by the WVA value shown in Table 2.9.

Phase	WVA(gh^{-1})	**Socks** (%)	**Boots** (%)	**Evaporated** (%)
1^{st}	10.43	26	66	8
2^{nd}	8.65	6	82	12
3^{rd}	5.23	1	70	29
4^{th}	3.24	0	57	43
5^{th}	0.06	0	3	97

Table 2.9 Water Vapour Absorption (WVA) value in the five phases of the drying curve detected in the 16-hour test and the % of water in socks, boots, and evaporated amount after each weighing.

To determine which of the two processes (condensation and absorption) was primarily responsible for the movement of water mass from the sock to the shoe, a drop test was conducted to observe which of the materials used in constructing the inner surface of the boots was more permeable. Material A and B are made of polyester fleece, while material C is a polyurethane foam covered by a large polyester fabric. The results are shown in Figure 2.17.

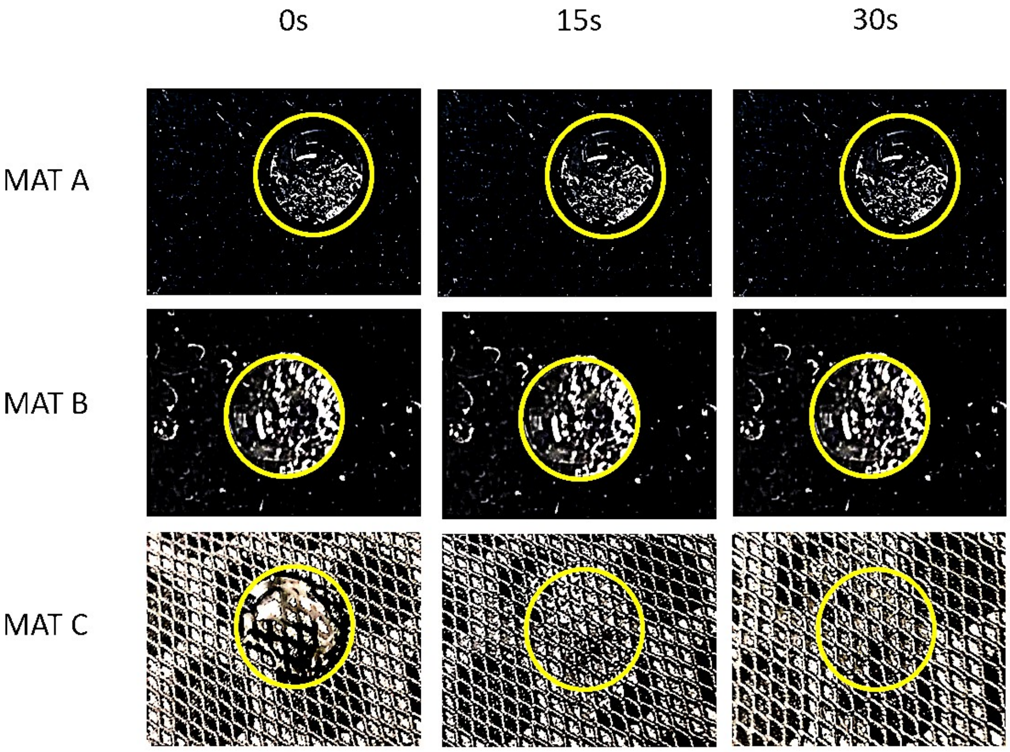

Fig. 2.17 Water droplets test results on the three different compounds that compose the inside of the boot. The water drop is highlighted in yellow.

“Mat C” completely absorbed the water droplet, while Mat A and B showed a strongly hydrophobic behaviour. However, material C represents a negligible percentage of the inner surface of the boots; therefore, the greatest contribution to water migration is made by evaporation, followed by condensation on the inner surface of the boots.

In Figure 2.18, a comparison between the 30g wet test, the dry test, and the isothermal test is shown. The grey dashed area in the graph represents the estimated contribution of the pure wet component in heat loss.

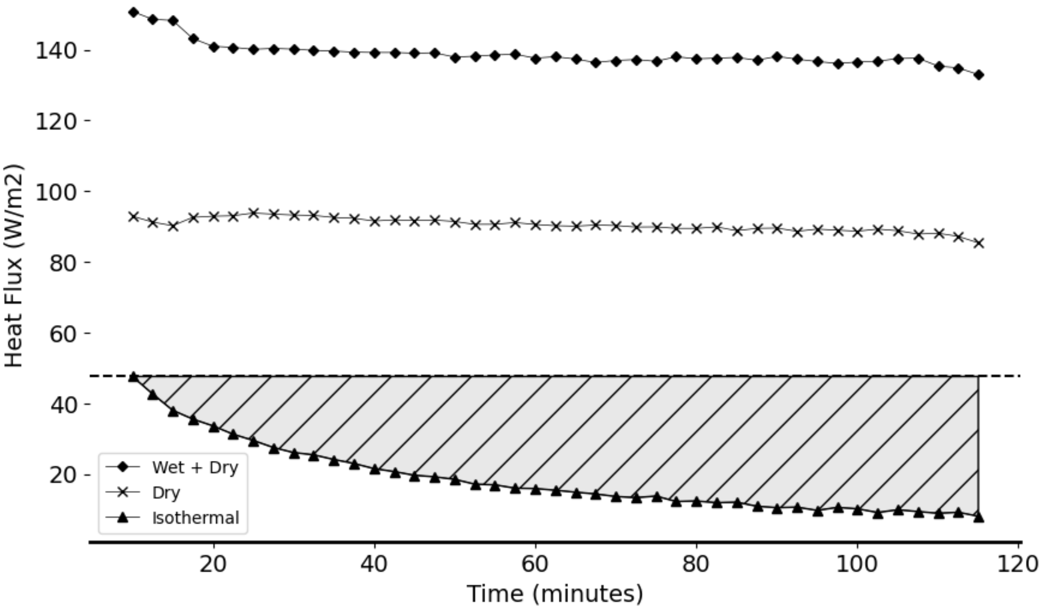

Fig. 2.18 Comparison between the first 120 minutes of the 30g wet test, dry test, and isothermal test results. The pure wet component is represented by the straight line at the top of the grey area.

By integrating the curves, the value of the energy supplied to the manikin in the observed area was estimated. The calculations of the different components of the heat exchange were as follows:

$$\int_{t_0}^{t} Q_D dt = U_D = 9.6(kJm^{-2}) \tag{2.21}$$

$$\int_{t_0}^{t} Q_{W+D} dt = U_{W+D} = 14.6(kJm^{-2}) \tag{2.22}$$

Where Q_D identifies the dry component of heat exchange while Q_W is the value of the wet and dry component that considers the contribution from the evaporative and conductive heat loss, but also the increase in heat loss due to the presence of liquid water. In Figure 2.18, this component is represented by the straight line at the top of the grey zone.

$$U_{W+D} - U_D = U_{E+K+C} = 5(kJm^{-2}) \tag{2.23}$$

U_{E+K+C} is given from the difference between the wet and dry component and the pure dry one, giving the value of the evaporative, conductive heat loss and the condensation component as well.

$$\int_{t_0}^{t} Q_E dt = U_E = 1.9(kJm^{-2}) \tag{2.24}$$

$$U_{E+K+C} - U_E = U_{K+C} = 3.1(kJm^{-2}) \tag{2.25}$$

Finally, both the evaporative heat loss (Q_E) and the heat loss due to the presence of condensed water and conduction (U_{K+C}) are evaluated.
The evaporative heat flux (evaluated with the mass loss method, E_{mass}, λ=2472 Jg^{-1} at 10°C), the apparent heat loss (E_{app}, which counts the contribution of condensation, conduction, and evaporation) and the evaporative cooling efficiency (as the ratio of the last two) were estimated for each phase; the results are shown in Table 2.10.

Phase	$E_{mass}(Wm^{-2})$	$E_{app}(Wm^{-2})$	$\eta(E_{app}/E_{mass})$	**Cumulative Water Evaporated** (%)
1^{st}	14.45	54.51	3.77	8
2^{nd}	15.11	27.50	1.82	12
3^{rd}	54.33	16.10	0.31	29
4^{th}	36.35	9.90	0.27	43
5^{th}	0.97	5.7	5.94	97

Table 2.10 Heat of evaporation, apparent heat loss and evaporation efficiency in the different phases of the long test

According to η_{app}, the value of the effective latent heat of evaporation $\lambda_{eff}(Jg^{-1})$ seems to decrease with increasing time, even if the total amount of water is almost the same in the first stages. The relationship was then also verified using a regression analysis, where η_{app} and time were used as independent variables and the water content of the boots as dependent variables. The analysis showed a good fit of the model to the selected data (R^2 = 0.985) and revealed a statistically significant correlation between the value of η_{app} and the water content of the boots (p-value < 0.05). A higher evaporative cooling efficiency does not always result in higher values of effective evaporation.

In the isothermal test, where no condensation takes place, λ_{eff} was measured as well showing a lower value compared to the theoretical one (λ = 2419 (Jg^{-1}) at 34°C, E_{app} = 21.3 (Wm^{-2}), E_{mass} = 24.19 (Wm^{-2}), η_{app} = 0.88, λ_{eff} = 2128 (Jg^{-1})).

To summarise, water starts to evaporate from the first moments, but since the materials of the boots are mostly hydrophobic and impermeable (see Figure 2.17), condensation occurs as the vapour reaches the colder inner surface of the boots (Bröde et al., 2008). As shown in Figure 2.10, if the value of η_{app} is greater than 1, this means that the latent heat calculated from the effective mass is less than the effective observed heat loss, as the losses due to condensation strongly influence the system. This statement is also confirmed by the value of the energy consumed by the manikin, which was determined by integrating the curves of the various heat flows recorded during the study (see Figure 2.18). In this way, it was possible to evaluate the amount of each contribution to heat exchange, apart from the pure conduction value, which was considered almost negligible and was embedded in the condensation contribution. The higher value of the heat loss observed (3.1 KJm^{-2}) compared to the value obtained for the evaporative heat loss (1.9 KJm^{-2}) confirms that a high rate of evaporative cooling is not synonymous with a high effective evaporative efficiency. One could wrongly say that the only process that contributes to cooling the body is the one in which water leaves the entire clothing system. This assumption could lead to an incorrect estimation of evaporative heat loss if the moisture condenses in the outer layers. In addition, latent heat transfer in highly impermeable systems such as the one considered leads to strong inaccuracies and limitations, as already emphasised in previous studies (Joshi et al., 2023). Furthermore, the results obtained confirm what was already stated by Havenith et al. (Havenith et al., 2013). The efficiency of evaporative cooling decreases as soon as the water charged in the system is moved away from the skin (i.e., the manikin), as can be seen in Table 2.10. The water vapour resistance R_{eT} was evaluated using both the heat and mass loss methods. The results are shown in Table 2.11.

Method	$R_{eT}(Pa\,m^2\,W^{-1})$
Heat Loss	187.68
Mass Loss	205.34

Table 2.11 Value of evaporative resistance evaluated with two different methods

From the value of R_{eT}, as reported in Eq. 12, the value of i_m can be calculated. The value obtained is 0.07, which relies on the lowest half of the range described in Section 2.2.2.2. According to Woodcock's study (Woodcock, 1962), with a fixed dry heat loss and insulation, the i_m of the clothing worn should be as high as possible to adapt to varied environments and situations. The hypothesis that water hardly leaves the system is consistent, as already shown by the high percentage of remaining water in Table 2.6.

2.4 Conclusion

The experimental investigation, which included both human trials and measurements on thermal manikins, provided a comprehensive overview of the thermoregulatory challenges that occur in cold alpine environments. The human studies allowed us to explore how physical activity, ambient temperature and footwear insulation interact to influence both local and systemic thermal responses. Of all the regions measured, the big toe was consistently found to be the most sensitive site, confirming its role as a key indicator of thermal discomfort and cold-related risks.

Physiological data emphasised the pivotal role of physical activity in attenuating cold-induced vasoconstriction (CIVC). Even light exercise helped maintain higher big toe temperatures and reduced inter-subject variability, suggesting a more stable and homogeneous thermoregulatory adaptation. In these protocols, temperature curves stabilised rapidly, indicating a faster achievement of thermal equilibrium between heat production and loss. While ambient temperature had a smaller effect due to competing physiological mechanisms and inter-individual variability, extremely low temperatures appeared to override vasodilatory (CIVD) responses, increasing the likelihood of peripheral cooling and frostbite.

While footwear insulation was not statistically significant in terms of differences in average skin temperature, it did show effects on toe temperature distribution, particularly with prolonged exposure or reduced insulation. This indicates a secondary, but not negligible, role in thermal protection.

The human experimental tests highlighted a significant accumulation of moisture in the toe and heel regions during physical activity, motivating a focused analysis of the influence of perspiration on the thermal insulation of footwear. While these results provide valuable insight into the coupled heat and moisture transfer processes occurring at the foot–footwear interface, limitations in the generalisability of the findings must be explicitly acknowledged.

The participant group consisted primarily of young, physically active male subjects accustomed to cold exposure. This selection was intentionally adopted to ensure participant safety, reduce inter-subject variability, and allow a controlled investigation of footwear-related effects under cold conditions. However, thermophysiological responses are known to vary substantially with sex, age, body composition, and acclimatisation status. For example, differences in peripheral blood flow regulation, sweat production, and subcutaneous fat distribution may influence both heat loss mechanisms and local thermal perception at the foot. Consequently, the absolute values of temperature, moisture accumulation, and comfort thresholds observed in this study should not be directly extrapolated to broader populations.

Nevertheless, the primary objective of the experimental campaign was not to establish population-wide comfort limits, but rather to develop and validate methodologies capable of discriminating between different levels of thermal insulation and moisture management performance in cold-protective footwear under controlled conditions. From this perspective, the selected participant group provides a consistent physiological baseline against which footwear effects can be reliably compared. The extension of these findings to more heterogeneous populations, including female participants, older individuals, and subjects with different body compositions or acclimatisation histories, represents a natural and necessary direction for future research.

It should also be noted that while the core experimental protocol focused on male participants, a limited number of female subjects were included in specific test conditions and are reported in the corresponding tables. These data were not intended to support sex-based comparisons, but are reported for completeness. Future studies should adopt a balanced experimental design to explicitly investigate sex-related differences in foot thermoregulation and footwear performance.

In this context, measurements on thermal manikins proved essential as they provide controlled and reproducible conditions to isolate the effects of moisture.

We found that loosely bound water tends to evaporate easily and then condense within the boot layers, releasing some of the lost heat through latent heat recovery. It was found that the efficiency of evaporative cooling (η_{app}) is highest at the beginning of the process, when the evaporation front remains close to the surface, and decreases significantly as the front moves outwards. This has remarkable effects: estimates of latent heat loss based on mass loss may overestimate its impact, as much of the heat recovery occurs after condensation and not directly at the skin-manikin interface.

Furthermore, as the evaporation front moves away from the surface, a significant portion of the energy required for evaporation is removed from the surrounding microclimate rather than the body, limiting the cooling effect on the subject. As a result, the effective latent heat (λ_{eff}) remains far below the theoretical values.

The tests also confirmed the crucial role of moisture retention and transfer dynamics. Although waterproof outer membranes effectively prevent the penetration of moisture from the outside, they also hinder the release of perspiration vapour from the inside. This double effect can trap moisture inside the boot, reducing both the release of evaporative heat and thermal comfort, and possibly contributing to a delayed cooling effect ("aftercooling").

Although the overall thermal resistance of the footwear system remained largely unaffected by the presence of moisture, which is likely due to the thermal mass of the footwear outweighing the relatively small addition of water, the evaporative parameters (η_{app}, λ_{eff}) showed significant sensitivity to moisture. These results emphasise the importance of moisture management in the development of footwear for cold environments.

Ultimately, the integration of human and manikin data provided a dual perspective: human trials revealed the complex physiological interplay between cold, exertion and individual variability, while manikin testing allowed controlled quantification of the effects of moisture on insulation performance. This complementary approach underlines the value of an integrated experimental framework for the evaluation of cold weather equipment, that considers both the adaptive responses of the human body and the material behaviour of footwear under real-world stress conditions.

References

Alduchov, O.A., Eskridge, R.E., 1996. Improved magnus form approximation of saturation vapor pressure 35, 601–609. doi:10.1175/1520-0450(1996)035<0601:IMFAOS>2.0.CO;2.

Aoyagi, Y., McLellan, T.M., Shephard, R.J., 1996. Residual analysis in the determination of factors affecting the estimates of body heat storage in clothed subjects 73, 287–298. URL: https://doi.org/10.1007/BF02425489, doi:10.1007/BF02425489.

Bianca, E., Dotti, F., Ferri, A., Havenith, G., 2025. Heat and mass transfer in footwear: Exploring the moisture evaporation and condensation cycle 55, 15280837251325783. URL: https://doi.org/10.1177/15280837251325783, doi:10.1177/15280837251325783.

Bianca, E., Dotti, F., Orrico, F., Ferri, A., 2024. Thermoregulation of feet in cold environments: A study on alpinism 116. doi:10.1016/j.apergo.2023.104205.

Bogerd, C.P., Brühwiler, P.A., Rossi, R.M., 2012. Heat loss and moisture retention variations of boot membranes and sock fabrics: A foot manikin study. International Journal of Industrial Ergonomics 42, 212–218.

Bröde, P., Havenith, G., Wang, X., Candas, V., Hartog, E.A., Griefahn, B., Holmér, I., Kuklane, K., Meinander, H., Nocker, W., Richards, M., 2008. Non-evaporative effects of a wet mid layer on heat transfer through protective clothing 104, 341–349. URL: https://doi.org/10.1007/s00421-007-0629-y, doi:10.1007/s00421-007-0629-y.

Cheng, C., Matsukawa, T., Sessler, D.I., Ozaki, M., Kurz, A., Merrifield, B., Lin, H., Olofsson, P., 1995. Increasing mean skin temperature linearly reduces the core-temperature thresholds for vasoconstriction and shivering in humans. Anesthesiology 82, 1160–1168. URL: https://doi.org/10.1097/00000542-199505000-00011, doi:10.1097/00000542-199505000-00011.

Cheung, S.S., 2015. Responses of the hands and feet to cold exposure. Temperature 2, 105–120. URL: https://doi.org/10.1080/23328940.2015.1008890, doi:10.1080/23328940.2015.1008890.

Coull, N.A., West, A.M., Hodder, S.G., Wheeler, P., Havenith, G., 2021. Body mapping of regional sweat distribution in young and older males 121, 109–125. URL: https://doi.org/10.1007/s00421-020-04503-5, doi:10.1007/s00421-020-04503-5.

Daanen, H.A., van Ruiten, H.J., 2000. Cold-induced peripheral vasodilation at high altitudes–a field study 1, 323–329. doi:10.1089/15270290050502390.

Das, B., Das, A., Kothari, V.K., Fanguiero, R., Araújo, M.D., 2007. Moisture transmission through textiles 7, 100–110. URL: https://www.degruyter.com/document/doi/10.1515/aut-2007-070204/html, doi:10.1515/aut-2007-070204.

Flouris, A.D., Westwood, D.A., Mekjavic, I.B., Cheung, S.S., 2008. Effect of body temperature on cold-induced vasodilation 104, 491–499. doi:10.1007/s00421-008-0798-3.

Fohr, J.P., 2015. Heat and Moisture Transfer between Human Body and Environment. URL: https://www.wiley.com/en-us/Heat+and+Moisture+Transfer+between+Human+Body+and+Environment-p-9781848218932.

Goldman, R.F., 1974. Clothing design for comfort and work performance in extreme thermal environments 36, 531–544. doi:10.1111/j.2164-0947.1974.tb01599.x, arXiv:4530541.

Havenith, G., Bröde, P., Hartog, E., Kuklane, K., Holmer, I., Rossi, R.M., Richards, M., Farnworth, B., Wang, X., 2013. Evaporative cooling: Effective latent heat of evaporation in relation to evaporation distance from the skin 114, 778–785. doi:10.1152/japplphysiol.01271.2012, arXiv:23329814.

Havenith, G., Heus, R., Lotens, W.A., 1990. Resultant clothing insulation: A function of body movement, posture, wind, clothing fit and ensemble thickness 33, 67–84. URL: https://doi.org/10.1080/00140139008927094, doi:10.1080/00140139008927094.

Havenith, G., Richards, M.G., Wang, X., Bröde, P., Candas, V., Hartog, E., Holmér, I., Kuklane, K., Meinander, H., Nocker, W., 2008. Apparent latent heat of evaporation from clothing: Attenuation and “heat pipe” effects 104, 142–149. URL: https://journals.physiology.org/doi/full/10.1152/japplphysiol.00612.2007, doi:10.1152/japplphysiol.00612.2007.

Heinisch, T., Bajzík, V., Hes, L., 2019. New methodology and instrument for determination of the isothermal drying rate of cotton and polypropylene fabrics at constant air velocity 14, 1558925019873482. URL: https://doi.org/10.1177/1558925019873482, doi:`10.1177/1558925019873482`.

Huang, J., 2006. Thermal parameters for assessing thermal properties of clothing 31, 461–466. URL: https://www.sciencedirect.com/science/article/pii/S0306456506000507, doi:`10.1016/j.jtherbio.2006.03.001`.

ISO, 1997. Bs en iso 5084:1997 textiles. determination of the thickness of textiles and textile products.

ISO, 2004. BS EN ISO 15831:2004 Clothing. Physiological effects. Measurement of thermal insulation by means of a thermal manikin. URL: https://www.iso.org/standard/28720.html.

ISO, 2007a. BS EN ISO 11079:2007 Ergonomics of the thermal environment. Determination and interpretation of cold stress when using required clothing insulation (IREQ) and local cooling effects. URL: https://bsol-bsigroup-com.ezproxy.biblio.polito.it/Bibliographic/BibliographicInfoData/000000000030118491.

ISO, 2007b. ISO 9920:2007 - Ergonomics of the thermal environment — Estimation of thermal insulation and water vapour resistance of a clothing ensemble. URL: https://www.iso.org/standard/39257.html.

ISO, 2008. BS EN ISO 9886:2004 Ergonomics. Evaluation of thermal strain by physiological measurements. URL: https://www.iso.org/standard/34110.html.

ISO, 2019. BS EN ISO 10551:2019-Ergonomics of the physical environment. Subjective judgement scales for assessing physical environments.

ISO, 2021. BS EN ISO 8996:2021 Ergonomics of the thermal environment. Determination of metabolic rate. URL: https://bsol-bsigroup-com.ezproxy.biblio.polito.it/Bibliographic/BibliographicInfoData/000000000030366784.

ISO, 2023. BS EN ISO 7933:2023 Ergonomics of the thermal environment. Analytical determination and interpretation of heat stress using calculation of the predicted heat strain. URL: https://bsol-bsigroup-com.ezproxy.biblio.polito.it/Bibliographic/BibliographicInfoData/000000000030436561.

Ji, P., Jin, J., Chen, X., Wang, C., Wang, H., 2016. Characterization of water state and distribution in fibre materials by low-field nuclear magnetic resonance 6, 11492–11500. URL: https://pubs.rsc.org/en/content/articlelanding/2016/ra/c5ra21018f, doi:10.1039/C5RA21018F.

Joshi, A., Psikuta, A., Annaheim, S., Rossi, R.M., 2023. Modelling of heat and mass transfer in clothing considering evaporation, condensation, and wet conduction with case study 228, 109786. URL: https://www.sciencedirect.com/science/article/pii/S0360132322010162, doi:10.1016/j.buildenv.2022.109786.

Kuklane, K., 2009. Protection of feet in cold exposure 47, 242–253. doi:10.2486/indhealth.47.242, arXiv:19531910.

Kuklane, K., Geng, Q., Holmér, I., 1998. Effect of Footwear Insulation on Thermal Responses in the Cold 4, 137–152. doi:10.1080/10803548.1998.11076386, arXiv:10602614.

Kuklane, K., Holmér, I., 1997. Reduction of footwear insulation due to walking and sweating, in: Problems with cold work. URL: https://www.semanticscholar.org/paper/Reduction-of-footwear-insulation-due-to-walking-and-Kuklane-Holm%C3%A9r/7c9e96cd2b1e00769daed422fe14ea9b73fdc646.

Kuklane, K., Holmér, I., Anttonen, H., Burke, R., Doughty, P., Endrusick, T., Hellsten, M., Shen, Y., Uedelhoven, W., 2005. Inter-laboratory tests on thermal foot models, in: Tochihara, Y., Ohnaka, T. (Eds.), Elsevier Ergonomics Book Series. Elsevier. volume 3 of *Environmental Ergonomics*, pp. 449–457. URL: https://www.sciencedirect.com/science/article/pii/S1572347X05800710, doi:10.1016/S1572-347X(05)80071-0.

Kuklane, K., Holmér, I., Giesbrecht, G., 1999. Change of footwear insulation at various sweating rates 18, 161–168. doi:10.2114/jpa.18.161, arXiv:10584395.

Li, W., Xu, W., Cui, W., Wang, X., 2008. A novel method to analyze the moisture liberation of textile fabrics 9, 312–316. URL: https://doi.org/10.1007/s12221-008-0050-0, doi:10.1007/s12221-008-0050-0.

Liu, Y., Dang, B., Li, Y., Lin, H., Ma, H., 2016. Applications of Savitzky-Golay Filter for Seismic Random Noise Reduction 64, 101–124. URL: https://doi.org/10.1515/acgeo-2015-0062, doi:10.1515/acgeo-2015-0062.

O'Brien, C., 2005. Reproducibility of the cold-induced vasodilation response in the human finger 98, 1334–1340. doi:10.1152/japplphysiol.00859.2004.

Savitzky, A., Golay, M.J.E., 1964. Smoothing and Differentiation of Data by Simplified Least Squares Procedures. 36, 1627–1639. URL: https://doi.org/10.1021/ac60214a047, doi:10.1021/ac60214a047.

Schols, E., Eijnde, W., Heus, R., 2004. A method for assessing thermal comfort of shoes using a "sweating" foot 92, 706–9. doi:10.1007/s00421-004-1143-0.

Smith, C.J., Havenith, G., 2011. Body mapping of sweating patterns in male athletes in mild exercise-induced hyperthermia 111, 1391–1404. URL: https://doi.org/10.1007/s00421-010-1744-8, doi:10.1007/s00421-010-1744-8.

Taylor, N., Machado-Moreira, C., Heuvel, A., Caldwell, J., Taylor, E., Tipton, M., 2009. The roles of hands and feet in temperature regulation in hot and cold environments , 405–409URL: https://ro.uow.edu.au/hbspapers/190.

Toma, R., Kuklane, K., Fojtlín, M., Fišer, J., Jícha, M., 2021. Using a thermal manikin to determine evaporative resistance and thermal insulation – A comparison of methods 50, 1493–1515. URL: https://doi.org/10.1177/1528083719900672, doi:10.1177/1528083719900672.

Wang, F., 2017. Measurements of clothing evaporative resistance using a sweating thermal manikin: An overview 55, 473–484. URL: https://www.jstage.jst.go.jp/article/indhealth/55/6/55_2017-0052/_article/-char/ja/.

Wang, F., Kuklane, K., Gao, C., Holmér, I., 2010. Development and validity of a universal empirical equation to predict skin surface temperature on thermal manikins 35, 197–203. URL: https://www.sciencedirect.com/science/article/pii/S030645651000029X, doi:10.1016/j.jtherbio.2010.03.004.

West, A.M., Oberst, F., Tarrier, J., Heyde, C., Schlarb, H., Brüggemann, G.P., Hodder, S., Havenith, G., 2023. A thermal foot manikin as a tool for footwear evaluation and development. Proceedings of the Institution of Mechanical Engineers, Part P: Journal of Sports Engineering and Technology 237, 34–46.

West, A.M., Tarrier, J., Hodder, S., Havenith, G., 2019. Sweat distribution and perceived wetness across the human foot: The effect of shoes and exercise intensity 62, 1450–1461. doi:10.1080/00140139.2019.1657185, arXiv:31422758.

Wissler, E.H., Havenith, G., 2009. A simple theoretical model of heat and moisture transport in multi-layer garments in cool ambient air 105, 797–808. URL: https://doi.org/10.1007/s00421-008-0966-5, doi:`10.1007/s00421-008-0966-5`.

Woodcock, A., 1962. Moisture Transfer in Textile Systems, Part I 32, 628–633. URL: https://doi.org/10.1177/004051756203200802, doi:`10.1177/004051756203200802`.

Youssef, A., Verachtert, A., De Bruyne, G., Aerts, J.M., 1996. Reverse engineering of thermoregulatory cold-induced vasoconstriction/vasodilation during localized cooling 9, 3372. doi:`10.3390/app9163372`.

Chapter 3

Physics-Based Approach

This chapter investigates the computational approach to analysing the interaction between the human-boot system and the external environment. In addition to the detailed description of the CAD modelling process and the rationale behind the geometric choices, particular attention is given to the validation and analysis of the CFD simulations, which were systematically supported by experimental campaigns. The overall goal of this work was to create a digital framework capable of reproducing the thermal manikin test defined in ISO 15831:2004. In this way, it was possible to reproduce the assessment of the thermal insulation of footwear, a key parameter for evaluating protective performance, under virtual conditions. This approach made it possible to estimate the insulation properties of a prototype at the design phase, before its physical production. Such a strategy not only reduces the time and cost of iterative prototyping but also enables the creation of a physics-based digital twin of the human-shoe-environment system suitable for predicting performance under different operating conditions.

3.1 Purpose of the study

The aim of this approach is to define an initial quantitative parameter for differentiating the thermal performance of footwear. The most common method for evaluating the thermal insulation of garments, and also of footwear, is described in ISO 15831:2004 "*Clothing, Physiological effects: Measurement of thermal insulation using a thermal manikin*" (ISO, 2004). Although ISO 20344:2021 "*Personal protective equipment: Test methods for footwear*" (ISO, 2021) is also available (and described in Section 1.2.2), it was considered unreliable for this purpose, as it provides a rough analysis of thermal behaviour that does not allow for accurate differentiation between models.

However, the equipment required to perform tests according to ISO 15831 is expensive and generally not available to industrial laboratories. As a result, the development of prototypes in companies is often cumbersome and superficial, especially in the early design stages when a product is still far from large-scale production and more cost-effective evaluation methods are favoured. In this context, finding a way to evaluate and compare the thermal performance of a prototype before production, even if only minor changes are made to the composition, would significantly streamline the design and prototyping phases.

This study not only allowed us to replicate the human test protocol previously described in Section 2.1, but also a digital twin of the ISO 15831 testing procedure using CFD simulations in Ansys Fluent (Manual, 2009), identifying the thermal resistance of the system (R_{cT}) as a crucial discriminating parameter, but also allowed an in-depth study of the thermal behaviour of the boot under different environmental and soil conditions. In particular, the model allowed us to isolate and analyse the contributions of the different heat transfer mechanisms to the overall heat loss.

Furthermore, to our knowledge, no such comprehensive and customisable model, capable of accounting for the heterogeneity of material composition, has been developed for the study of heat exchange between boots and the environment.

Part of the work described in this chapter has been previously published in Bianca et al. (2025a).

3.2 Governing Equations

The physical volume simulated in this work comprises the walls of the boot and some quiescent gas pockets between the foot and the boot. In these areas, the heat transfer is purely conductive, so that the temperature obeys the Fourier equation:

$$\rho \mathrm{c_p} \frac{\partial \mathrm{T}}{\partial \mathrm{t}} = \tilde{\nabla} \cdot (\mathrm{k} \tilde{\nabla} \mathrm{T}) \tag{3.1}$$

where k is the thermal conductivity of the material, ρ the density, and c_p the specific heat capacity. The inner and outer edges of the domain are described by prescribing appropriate boundary conditions, which are of different types and include:

a) prescribed temperature: condition imposed at the contact between sole and ground, and, in the manikin tests, at the contact between the manikin and the internal surface of the boots (i.e., $(T_{\mathrm{cleats}} = T_{\mathrm{ground}})$ in the sole area, and $(T_{\mathrm{inner\ boot}} = T_{\mathrm{manikin}})$ at the interface between the manikin and the boot).

b) prescribed heat flux: imposed on the internal surface of the boot to represent the heat flux released by the foot during human subject tests. Mathematically, this boundary condition can be expressed as:

$$-\tilde{\mathrm{Q}} \cdot \tilde{\mathrm{n}} = \mathrm{Q_{foot}} \tag{3.2}$$

where Q_{foot} is the prescribed heat flux density at the foot–boot interface, and $\tilde{n}$ is the outward normal vector to the boot internal surface.

c) convective heat transfer: prescribed at the external surface of the boot in contact with the surrounding air. External fluid flow was not resolved in the model. Convective exchange with ambient air was represented using a constant heat transfer coefficient, without accounting for spatial variations due to local airflow dynamics. The heat flux density at the surface is:

$$\mathrm{Q_c} = \mathrm{h_c}(\mathrm{T_{ext}} - \mathrm{T_a}) \tag{3.3}$$

where T_{ext} is the temperature of the boot surface, T_a the ambient temperature and h_c the heat transfer coefficient.

d) **simplified boundary radiation**: To account for the radiative heat transfer between the surface of the shoe and the environment, we followed the approach described by Covill et al. (2008, 2010), modeling the radiation as a heat flux boundary condition acting on the outer surface of the shoe. In this formulation, radiation is treated as a non-linear phenomenon governed by the Stefan-Boltzmann law:

$$\mathrm{Q_r} = \varepsilon\sigma(\mathrm{T}_{\mathrm{boot}}^4 - \mathrm{T}_{\mathrm{a}}^4) \tag{3.4}$$

where ε is the emissivity of the surface, σ is the Stefan-Boltzmann constant. In our model, we have a surface emissivity of 0.95, which is a typical value for textiles and fabric materials commonly used in footwear construction (Parsons, 2014).

Obviously, convective and radiative heat fluxes sum up to give the total surface heat flow rate.

At the interfaces between different materials within the boot domain, the following physical conditions are imposed to ensure continuity of the heat transfer process:

- Continuity of temperature:

$$\mathrm{T_1} = \mathrm{T_2} \tag{3.5}$$

- Continuity of heat flux:

$$-\mathrm{k_1}\frac{\partial \mathrm{T_1}}{\partial \tilde{\mathrm{n}}} = -\mathrm{k_2}\frac{\partial \mathrm{T_2}}{\partial \tilde{\mathrm{n}}} \tag{3.6}$$

Here, $\mathrm{T_1}$ and $\mathrm{T_2}$ are the temperatures on either side of the interface, and $\mathrm{k_1}$, $\mathrm{k_2}$ are the thermal conductivities of the adjacent materials.
The convective heat transfer coefficient $\mathrm{h_c}$ for the boot was evaluated from the Nusselt number (Santee and William, 2012):

$$\mathrm{Nu} = \frac{\mathrm{h_c L}}{\mathrm{k_a}} \tag{3.7}$$

where k_a is the thermal conductivity of air and L is the characteristic length to describe the considered system (which was approximated to a 0.4 m high cylinder). The air thermal conductivity was evaluated according to the following correlation (Parsons, 2014):

$$k_a = 2.41 \cdot 10^{-2} + 7.8 \cdot 10^{-5} T_a \quad Wm^{-1}K^{-1} \tag{3.8}$$

The Nusselt number represents the ratio between convective and conductive heat transfer at a boundary and is commonly correlated to fluid flow parameters such as the Reynolds number. Following (Parsons, 2014):

$$Nu = 0.24Re^{0.6} \tag{3.9}$$

The Reynolds number (Re) is calculated as the ratio between the product of the wind speed (w_s) and L, and the kinematic viscosity of air at the temperature considered, denoted ν (i.e., $1.31 \cdot 10^{-5}$ m^2s^{-1} at 10°C, $1.79 \cdot 10^{-5}$ m^2s^{-1} at 0°C):

$$Re = \frac{w_s L}{\nu} \tag{3.10}$$

In this way, the fluid velocity becomes intrinsic in the evaluation of the convective heat transfer coefficient.

In addition, earlier research (Bianca et al., 2025b) investigated coupled heat and mass transfer in footwear and showed that moisture evaporation and condensation cycles occur, but have a limited impact on thermal insulation performance under typical use scenarios (detailed study in Chapter 2, Section 2.2). This supports the assumption of dry air conditions in the present study without significant loss of accuracy.

3.3 Geometrical and physical properties

All components of the boot material were tested according to EN ISO 9920:2007 "*Ergonomics of the thermal environment — Estimation of thermal insulation and water vapour resistance of a clothing ensemble*" (ISO, 2007) to assess their thermal resistance R_{cT}. The materials were also tested according to the EN ISO 5084:1998 "*Determination of the thickness of textiles and textile products.*" (ISO, 1997) to evaluate their thickness (t in mm). Figure 3.1 shows the area in which the boot was divided. For soft polymeric foams and non-woven textiles, specific heat and density were estimated using the database provided by the software for flexible synthetic materials typically used in thermal insulation. A legend of the properties of the materials used in the different parts of the boot is shown in Table 3.1 and Table 3.2.

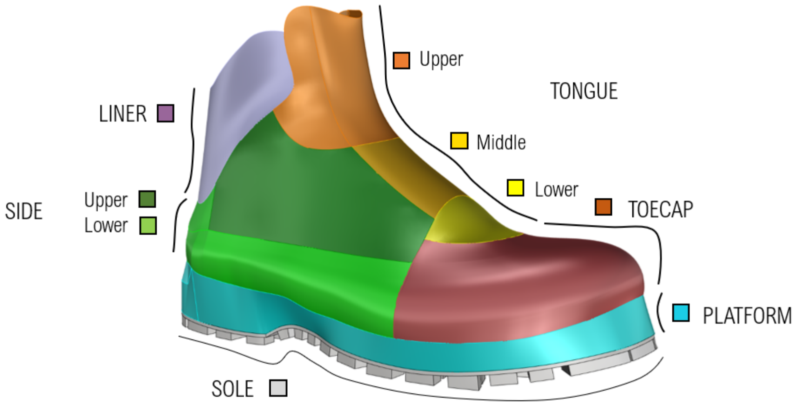

Fig. 3.1 Legend of the different areas in which the boot was split.

Area	**Property**	**Value**
Liner	Thermal Cond. ($W \cdot (mK)^{-1}$)	0.0395
	Specific Heat ($J \cdot (kgK)^{-1}$)	1600
	Density ($kg \cdot m^{-3}$)	100
Tongue (upper)	Thermal Cond. ($W \cdot (mK)^{-1}$)	0.0392
	Specific Heat ($J \cdot (kgK)^{-1}$)	1600
	Density ($kg \cdot m^{-3}$)	100
Tongue (middle)	Thermal Cond. ($W \cdot (mK)^{-1}$)	0.0360
	Specific Heat ($J \cdot (kgK)^{-1}$)	1600
	Density ($kg \cdot m^{-3}$)	100
Tongue (bottom)	Thermal Cond. ($W \cdot (mK)^{-1}$)	0.0350
	Specific Heat ($J \cdot (kgK)^{-1}$)	1600
	Density ($kg \cdot m^{-3}$)	100
Side (upper)	Thermal Cond. ($W \cdot (mK)^{-1}$)	0.0389
	Specific Heat ($J \cdot (kgK)^{-1}$)	1600
	Density ($kg \cdot m^{-3}$)	100
Side (lower)	Thermal Cond. ($W \cdot (mK)^{-1}$)	0.0216
	Specific Heat ($J \cdot (kgK)^{-1}$)	1500
	Density ($kg \cdot m^{-3}$)	60
Toecap	Thermal Cond. ($W \cdot (mK)^{-1}$)	0.0259
	Specific Heat ($J \cdot (kgK)^{-1}$)	1500
	Density ($kg \cdot m^{-3}$)	60
Fussbet	Thermal Cond. ($W \cdot (mK)^{-1}$)	0.0396
	Specific Heat ($J \cdot (kgK)^{-1}$)	1600
	Density ($kg \cdot m^{-3}$)	100
Platform	Thermal Cond. ($W \cdot (mK)^{-1}$)	0.2968
	Specific Heat ($J \cdot (kgK)^{-1}$)	1648
	Density ($kg \cdot m^{-3}$)	1200
Insole	Thermal Cond. ($W \cdot (mK)^{-1}$)	0.04
	Specific Heat ($J \cdot (kgK)^{-1}$)	1523
	Density ($kg \cdot m^{-3}$)	1140

Table 3.1 Thermal conductivity, specific heat, and density of the materials in the different areas of the boot.

Area	Property	Value
Liner	Thickness (m)	0.0143
	Surface Area (m^2)	0.026
Tongue (upper)	Thickness (m)	0.0106
	Surface Area (m^2)	0.016
Tongue (middle)	Thickness (m)	0.0113
	Surface Area (m^2)	0.007
Tongue (bottom)	Thickness (m)	0.0071
	Surface Area (m^2)	0.006
Side (upper)	Thickness (m)	0.0118
	Surface Area (m^2)	0.039
Side (lower)	Thickness (m)	0.0025
	Surface Area (m^2)	0.029
Toecap	Thickness (m)	0.0038
	Surface Area (m^2)	0.026
Fussbet	Thickness (m)	0.0038
	Surface Area (m^2)	0.034
Platform	Thickness (m)	0.0197–0.0308
	Surface Area (m^2)	0.062
Insole	Thickness (m)	0.0073–0.0091
	Surface Area (m^2)	0.059

Table 3.2 Thickness and surface area of the materials in the different areas of the boot.

The 3D model of the boot was reconstructed using CAD software based on a realistic reproduction by the Italian shoe manufacturer S.C.A.R.P.A. S.p.A.. Due to the inherent complexity of the footwear geometry, certain design details such as laces, lace holes and the outer gaiter (whose contribution to thermal insulation is minimal given the thin fabric and waterproof laminated membrane) were intentionally omitted to simplify the model. This simplification was necessary to make the numerical simulations computationally feasible while maintaining focus on the primary heat transfer mechanisms within the boot structure.

As the boot is a complex system made up of many different materials and has a non-uniform composition across its entire surface, the system was reconstructed by dividing each area of the boot into a different solid based on its composition. In this way, each region was designed separately according to composition and then assembled into the final assembly. This approach allowed the actual properties and thicknesses of the materials and composite layers to be mapped. The latter was measured after assembly, where potential compression can occur as a result of the joining of the different parts. Adhesives and sewing threads were not explicitly modelled in the current simulations. While these components can locally affect heat transfer by creating thermal bridges or insulating discontinuities, their overall impact on the bulk thermal resistance of the boot is expected to be limited.

The domain was discretized with a tetrahedral mesh consisting of about 300,000 cells, and the heat transfer problem was solved using a finite volume approach (Manual, 2009), and second-order discretization schemes. Due to the highly heterogeneous nature of the boot geometry (including multiple solid domains, varying material properties, and complex interfacial contact regions) the mesh was generated using a non-uniform strategy: finer cells were applied in regions with high temperature gradients (e.g., foot-insole interface, external surfaces exposed to airflow), while coarser elements were employed elsewhere to optimize computational efficiency. Mesh quality was assured by evaluating key quality metrics: the minimum orthogonal quality was found to be approximately 0.079, which is above the commonly accepted threshold of 0.05 for reliable thermal simulations (Frey and George, 2000), minimizing its impact on overall numerical accuracy (Oden and Carey, 1984). Furthermore, skewness and orthogonality metrics were monitored to ensure compliance with best practices for finite element and thermal analyses. Figure 3.2 shows details of the surface mesh. The choice of the selected grid was driven by a preliminary analysis on a simplified geometry, which showed that five cells on the smallest thickness (i.e., in our case the toecap region) will result in an error less than 3% on the evaluated heat flux, representing a good compromise between computational costs and accuracy.

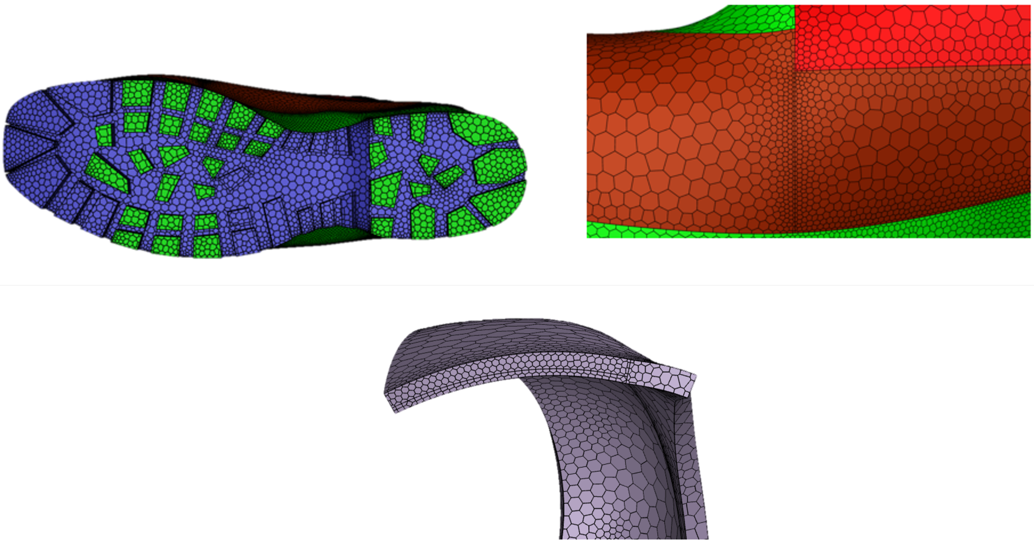

Fig. 3.2 Detail of the computational mesh in the sole area and at the interface between different material areas of the boot, where finer cells were used to resolve high thermal gradients. A detail of the toe cap area is shown with 5 layers of cells through its thickness.

3.4 Results and Discussion

3.4.1 Human tests simulations

Once the geometry was created, the first simulations carried out had the objective of reproducing the conditions of human tests performed in a climatic chamber using the same mountaineering boot model (Bianca et al., 2024). These tests were conducted at a controlled ambient temperature of –17 °C, a relative humidity of 50%, and a wind speed of 0.4 m/s. Participants were instructed to remain motionless for the entire duration of the test (i.e., 70 minutes) and wear standardised clothing that met the insulation needs of the specified environmental conditions. Thermal images of the outsole, toe cap, and side area of the shoe were taken throughout the test to monitor the distribution of surface temperature over time.

The first part of the work served as model verification and validation. The boundary conditions for this simulation included the ambient temperature (T_a) set at a value of T_{a1} = -17 °C according to previous human tests, convective heat transfer coefficient (h_{c1}) of 4.56 W/m^{2}K corresponding to a wind speed of 0.4 ms^{-1}, and internal heat flux within the boot corresponding to the blood flow described by Çengel (Cengel,

2002) for a person sitting and resting, that is 60 Wm^{-2} (Covill et al., 2010). The foot surface was estimated to be 7% of the total body surface (West et al., 2019) and, considering an average body surface area of 1.9 m^2, the imposed heat flow rate on the inner walls of the boot was estimated to be 7.98 W.

An important aspect of this simulation was the identification of the cleats in contact with the ground, in the case of flat ground. This was determined by analyzing more than 300 thermal images taken every 10 minutes during human tests. These thermal images, which can be seen in Figure 3.3, were crucial in selecting the cleats that remained in contact with the ground throughout, allowing an accurate representation of conductive heat transfer in these areas. In the simulation, the temperature of these cleats was set to T_{a1} whereas the coefficient h_{c1} was used to model heat transfer in the remaining portion of the sole.

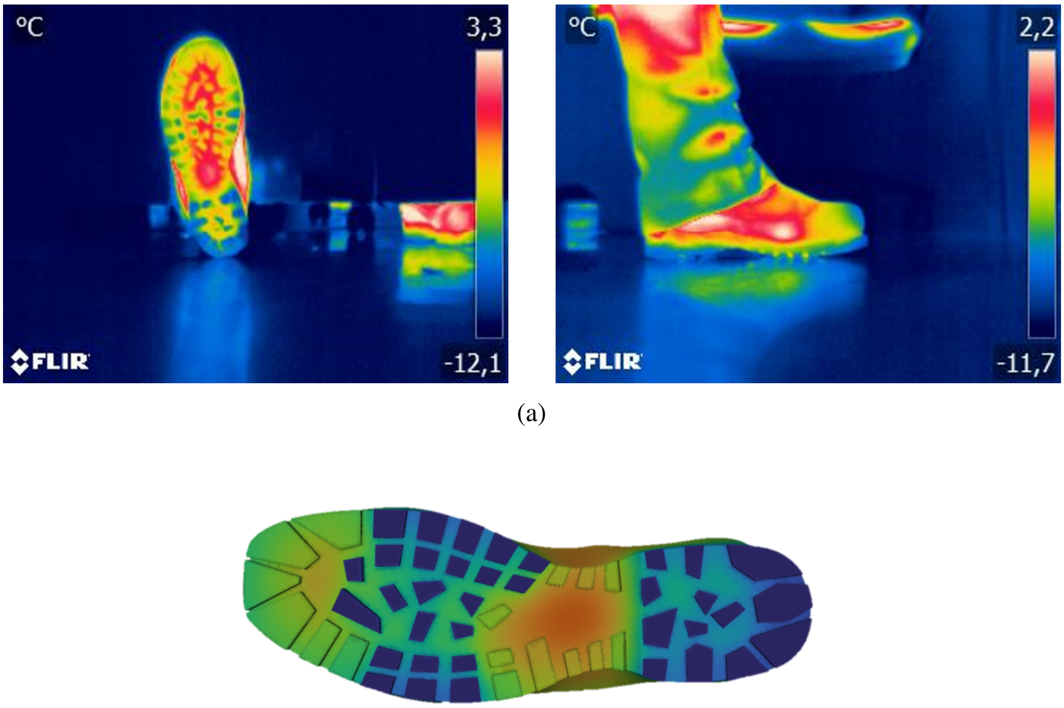

(a)

(b)

Fig. 3.3 Thermal data from tests and simulations: (a) thermal images acquired in climatic chamber and (b) contour plot of the static temperature of the sole (the blue cleats indicate the areas where the temperature was fixed to ambient temperature).

The same thermal images were used to record the average surface temperature of the toecap and compare it with the same temperature data resulting from the simulations. In fact, the toecap area was considered one of the most critical parts of the boot in terms of thermal comfort. Since the aim of this part of the work was to compare the evolution of the boot temperature over time with the experiments, this set of simulations was conducted in a transient mode.

Figure 3.4 shows the comparison between the simulation results and the experimental data from human tests. The experimental data points represent the average values of the mean surface temperature measured via thermal imaging across all participants, while the error bars indicate the minimum and maximum temperatures observed during the tests.
Initially, the model was evaluated considering only convective and conductive heat transfer, under the assumption that radiative exchange could be neglected. However, in order to improve the accuracy of the thermal simulation, additional simulations were performed by also incorporating radiative heat transfer as a surface boundary condition. The inclusion of radiation led to a closer agreement between simulated and experimental results, as evident in the time evolution of the area-weighted surface temperature in the toecap region. This improvement confirms the relevance of radiative effects in the thermal exchange between the boot and the environment, and supports the accuracy of the material properties implemented in the simulation.

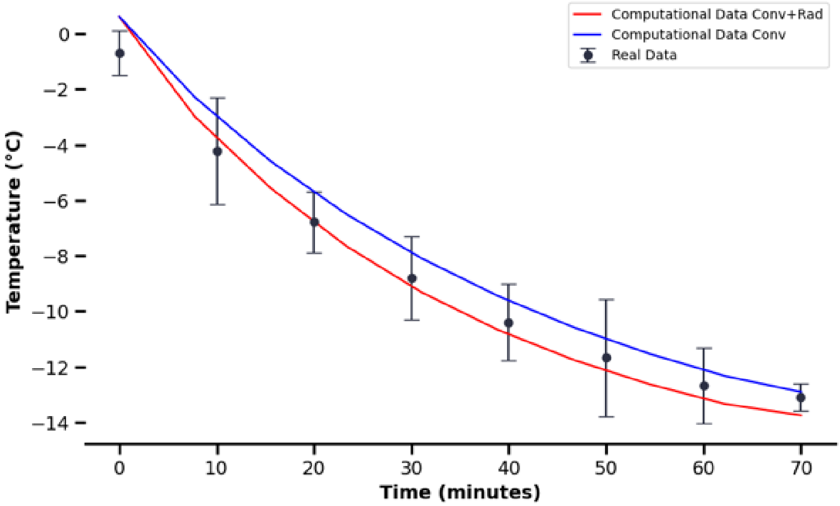

Fig. 3.4 Comparison between the computational and the experimental data of the area-weighted toecap surface temperature.

Figure 3.5 shows the temporal trend of the absolute error in the estimation of the surface temperature of the toecap both for the simulation that only takes convective heat into account and for the simulation that also takes radiant heat transfer into account. The lowest value of the absolute error of the second configuration confirms the increased accuracy in the second set.

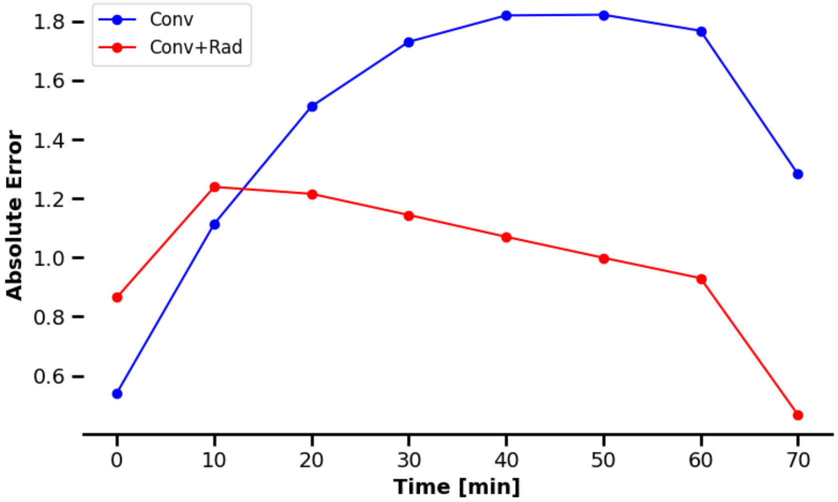

Fig. 3.5 Time evolution of the absolute error between simulated and experimental temperature data over the 70-minute test period, with measurements taken every 10 minutes.

The contour plot of temperature in Figure 3.6 clearly shows that the regions most affected by cooling are the area of the toecap and the lower part of the shoe upper in contact with the platform and the sole. The cooling in the toecap and the lower part of the shoe upper (i.e., the area named SIDE Lower in Fig. 3.1) is generally primarily due to convective heat transfer, while the sole experiences additional conductive heat loss through contact with the ground.

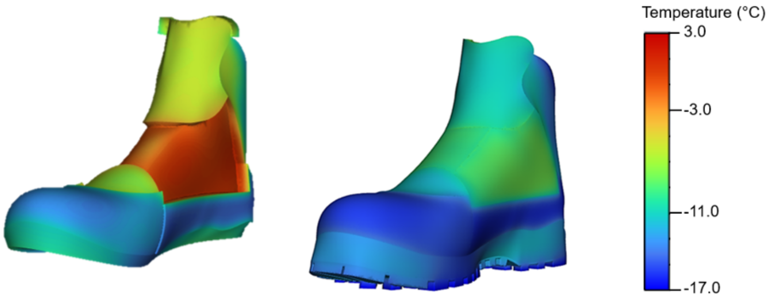

Fig. 3.6 Contour plot of temperature at the end of the 70 minutes test (the inside surface of the boot on the left side and the outside on the right side).

Indeed, the cleats that come into contact with the ground act as thermal bridges, with the heat flow increasing near these areas. Furthermore, the lowest value of the surface temperature seems to be in the sole and toecap area, which is a further indication of their crucial role in heat dissipation.

3.4.2 Virtual model of the thermal manikin test

Once the experimental data on human tests were correctly reproduced, the focus of the work was on evaluating the reliability of the R_{cT} values generated by the simulations, using the same boot model and computational mesh. The boundary conditions of the simulations were modified in order to mimic the procedure of Newton Thermal Manikin tests, according to UNI EN ISO 15831:2004 (ISO, 2004). The ambient temperature was set to the value of $T_{a,2}$= 10°C and the external heat transfer coefficient to 4.41 $W \cdot m^{-2} K^{-1}$ corresponding to 0.4 ms^{-1} wind speed. The main changes were those related to the foot, which was set at a constant temperature of 34 °C. In addition, a gap of quiescent air was introduced between the manikin's foot and the boot to reproduce the imperfect contact between the two elements experienced during the measurements. Figure 3.7 shows the three different attempts made: the first without an air gap, the second model where the foot is completely surrounded by air, and the third where the air has been removed from the lacing area, assuming boot-foot contact in this region.

Fig. 3.7 Different configuration of the system (MODEL A on the left, MODEL B in the middle, and MODEL C the right one), the blue part represents the air gap, the pink one the feet.

The thermal resistance R_{cT} was calculated as the ratio between the temperature gradient (between the foot and ambient temperature) and the heat flux from the foot (Q_{foot} in $W \cdot m^{-2}$) as follows:

$$R_{cT}(m^2KW^{-1}) = \frac{(T_{foot} - T_a)}{Q_{foot}} \tag{3.11}$$

The results obtained from the numerical simulations were compared with those obtained in the experimental campaign. The tests on the manikin were carried out in accordance with the aforementioned ISO standard, for which the ambient temperature must be set at 10 °C and an air velocity of 0.4 ms^{-1}. The manikin was dressed in standardised clothing that corresponded to that used in the human tests, with the exception of the socks, which were deliberately not worn. This allowed the thermal resistance value measured in the foot area to represent the insulation provided by the boot alone, without additional layers. The initial simulations concerned the system where the boot was filled with the foot, that is, Model A of Figure 3.7. The result of this set of simulations showed a significantly lower R_{cT} value compared to the experimental one measured with the manikin. It was this discrepancy that led us to hypothesise that an air gap between the boot and the foot was responsible for the higher thermal resistance. Consequently, two prototypes with different air gap distributions were generated (Model B and Model C in Figure 3.7). A comparison of the simulations performed on these models with the experimental results is summarised in Table 3.3.

	Heat Flux (W/m^2)	**Thermal Resistance** R_{cT} (m^{2}K/W)	**Deviation from real value** (%)
Newton	-87	0.276	——
Model A	-96	0.253	-9.97%
Model B	-71	0.338	+18.67%
Model C	-84	0.287	+3.45%

Table 3.3 Comparison of simulations with the experiments performed on Newton manikin.

The relative deviation from the experimental value was calculated using the following equation, as previously done by Tian et al. (Tian et al., 2016):

$$\text{Deviation} = \frac{\text{Simulated Value} - \text{Experimental value}}{\text{Experimental value}} \times 100 \tag{3.12}$$

Model A and Model C have similar deviations (in absolute value) from the experimental results, but Model C is more representative of a real-life scenario because of the presence of the air gap. Thus, Model C has been used as the reference boot model for subsequent simulations, with the objectives of calculating global thermal resistance $\mathrm{R_{cT}}$ and assessing thermal performance under varying environmental conditions.

Three different ground types were assumed to compare how the system would behave under different environmental conditions. The first, labeled "*stiff*", refers to the configuration where only the selected cleats are in contact with a stiff ground, and a fixed temperature boundary condition is applied to these cleats. The second type of soil is recent snow, where the entire platform and sole are assumed to be surrounded by snow, so a conductivity boundary condition is applied over the whole sole and platform (i.e., 1 cm of cells around the platform and sole area were modeled). The third ground type, labeled "*soil*," has the same thermal conductivity as "*Fairbanks sand*," which is typical for the Alaska region. As before, it was assumed that the entire sole and platform were surrounded by soil. The thermal conductivity values for the last two ground types are as follows: 0.078 $\mathrm{W \cdot (mK)^{-1}}$ for new and recent snow (Sturm et al., 2002) and 4.43 $\mathrm{W \cdot (mK)^{-1}}$ for Fairbanks sand (Zhang and Wang, 2017). An additional configuration was also created where the boot was supposed to be completely surrounded by air (i.e., with a thermal conductivity of 0.026 $W \cdot (mK)^{-1}$). For each soil configuration, six different environmental scenarios were examined, including ambient temperatures of -10 °C, 0 °C, or 10 °C, and wind speeds of 0.4 ms^{-1}, 1 ms^{-1}, or 10 ms^{-1}. Wind speeds were chosen as follows: 0.4 ms^{-1} to replicate the conditions of the manikin tests according to ISO 15831, 1 ms^{-1} to represent a higher but realistic value under normal conditions, and 10 ms^{-1} to simulate the scenario of a mountaineering expedition in extreme conditions. Since R_{cT} is an integral and stationary global resistance to heat transfer, this set of simulations was conducted in stationary mode.

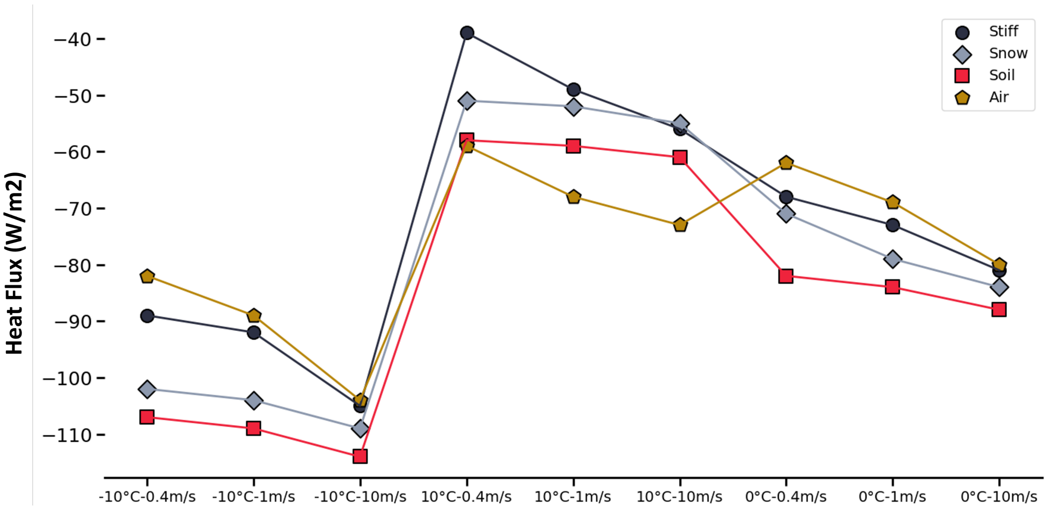

Fig. 3.8 Heat flux under different test conditions. Markers indicate discrete simulated conditions (combinations of air temperature and wind speed), while connecting lines are shown only as a visual guide to facilitate comparison across ground-contact scenarios and to highlight trends with changing convective and radiative contributions. Lines do not imply a continuous variation between tested points.

Figure 3.8 reports the total heat flux for the six different environmental conditions investigated. It should be noted that the heat flux values were obtained from a finite set of discrete simulated boundary conditions. The lines in Fig. 3.8 are therefore included purely to guide the eye and support readability when comparing ground-contact cases; they do not represent an interpolation model nor a physically continuous transition between conditions.

As can be seen, changing the soil type under the same environmental conditions (such as ambient temperature and wind speed) appears to have a significant impact on heat exchange. When the boot sole is immersed in recent snow, the worst thermal performance is observed, followed by soil conditions (that is, Fairbanks sand) and stiff conditions. This means that conductive heat transfer from the sole has the largest impact on thermal performance.

However, changes in environmental conditions affect mainly the convective contribution of the system, since variations in wind speed and air temperature influence the convective heat transfer coefficient h_c, which is used as a boundary condition on the outer surfaces of the boot.

The difference in the thermal behaviour of different parts of the boot can be seen in Figure 3.9a, where contour graphs of local heat flux are shown, highlighting the areas of the boot that are the most affected by increased heat flux toward the environment under the different simulated conditions.

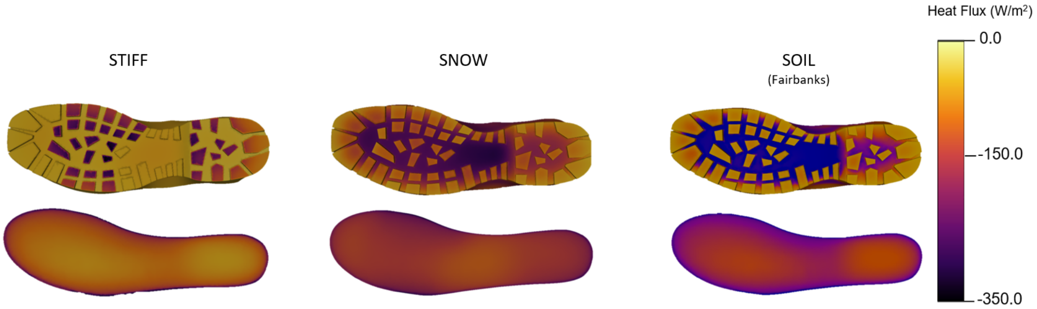

(a)

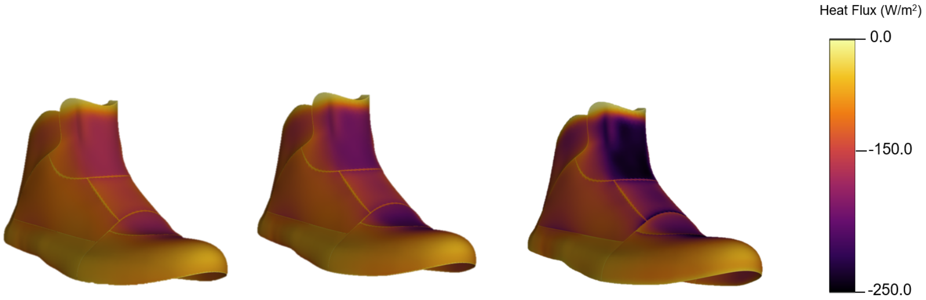

(b)

Fig. 3.9 Comparison of simulated heat flux contour plots under different boundary conditions. (a) Sole and insole contour plots obtained at fixed ambient conditions (air temperature of 0 °C and wind speed of 0.4 $\mathrm{m\,s^{-1}}$), highlighting the effect of ground contact and conductive heat transfer for three cases: selected cleats touching the ground (left), boot partially immersed in snow (middle), and boot immersed in Fairbanks soil (right).
(b) Upper boot contour plots simulated on stiff ground, showing the effect of varying convective conditions at a fixed ground type, for air temperature of 0 °C and wind speeds of 0.4 $\mathrm{m\,s^{-1}}$ (left), 1 $\mathrm{m\,s^{-1}}$ (middle), and 10 $\mathrm{m\,s^{-1}}$ (right).

Figure 3.9a shows the contour plots of the sole and insole, with the left side showing the simulations where only the cleats are in contact with the stiff and flat ground, the central one showing the simulations where the sole is immersed in fresh snow, and the right side showing the simulations where the sole is immersed in Fairbanks sand. In the last two cases, the heat flux is significantly higher. This confirms that the conductive contribution is mainly responsible for the variation of the heat flux values between the simulations.

On the other hand, Figure 3.9b compares three simulations in which the convective contribution changes due to variations in wind speed. In this case, although no significant changes are observed at the bottom, as the results belong to simulations with a stiff bottom, the upper part of the boot shows increased heat exchange, especially in areas such as the tongue and upper toecap.

A more comprehensive representation of the convective and conductive contributions in the different configurations under different environmental conditions can be found in Table 3.4, which shows the percentage values of the overall heat transfer rate for different areas of the boot. Although the tongue, sides, and lower area are mainly affected by an external convective heat transport, heat conduction is the predominant transport phenomenon in the lower area. Looking at the boot in its different components also allows for a closer look at the areas of the boot that exchange more heat with the environment. In fact, even if the lower area is normally considered the most critical, as it corresponds to the toes, the contribution to heat exchange appears to be lower than for the other parts due to the presence of a highly insulating material.

Moreover, the table shows that the configurations where the shoe is immersed in snow and Fairbanks sand have significantly higher values for conductive heat flux than the configuration where only some cleats are in contact with the stiff ground, while in the 'Air' configuration, the boot is surrounded by an airflow that does not make significant conductive contribution. This shows that the conductive contribution from the sole is substantial and greater than the convective one from the other parts of the boot.

Table 3.4 Contribution of the different areas to the heat transfer in the tested conditions, different ambient temperature (°C) and wind speed (ms^{-1}) compared to the total value (W).

Ground	T_a	w_s	**Percentage (%)**				**Total (W)**
			Tongue	**Side**	**Lower**	**Sole**	
Stiff	10	0.4	12	19	15	54	-5.53
		1	13	18	14	55	-5.9
		10	13	18	13	57	-6.79
	0	0.4	12	18	13	57	-8.42

Continued on next page

Table 3.4 – *Continued from previous page*

Ground	T_a	w_s	**Percentage (%)**				**Total (W)**
			Tongue	**Side**	**Lower**	**Sole**	
		1	12	18	14	57	-8.79
		10	13	17	13	57	-9.83
	-10	0.4	11	17	14	58	-10.71
		1	12	16	14	58	-11.11
		10	13	18	14	55	-12.14
Snow	10	0.4	11	17	13	59	-6.17
		1	12	17	13	58	-6.31
		10	13	18	14	55	-6.62
	0	0.4	15	22	17	47	-6.72
		1	13	18	13	57	-10.18
		10	10	15	11	64	-12.27
	-10	0.4	10	15	11	64	-12.27
		1	11	16	11	62	-12.56
		10	12	17	14	59	-13.19
Soil	10	0.4	10	15	11	65	-7.01
		1	10	15	11	64	-7.14
		10	13	16	11	60	-7.57
	0	0.4	9	15	10	66	-9.94
		1	10	15	11	64	-10.16
		10	12	16	11	61	-10.6

Continued on next page

Table 3.4 – *Continued from previous page*

Ground	T_a	w_s	**Percentage (%)**				**Total (W)**
			Tongue	**Side**	**Lower**	**Sole**	
	-10	0.4	10	15	10	66	-12.88
		1	10	15	11	64	-13.16
		10	12	16	11	61	-13.81
Air	10	0.4	13	19	15	54	-5.5
		1	13	18	14	55	-5.88
		10	13	17	13	57	-6.81
	0	0.4	13	18	13	56	-7.65
		1	13	18	14	55	-8.4
		10	13	17	13	57	-9.74
	-10	0.4	12	19	14	55	-9.13
		1	13	18	13	57	-10.75
		10	13	18	13	57	-12.52

In order to better understand the relative influence of key environmental factors on heat flux, a statistical analysis was conducted. The factors considered were ambient temperature (–10 °C, 0 °C, and 10 °C), wind speed (0.4, 1.0, and 10.0 ms^{-1}), and ground conditions (Air, Snow, Soil, and Stiff). As shown in Table 3.5, ambient temperature remains the dominant factor, with the average heat flux ranging from –95.9 Wm^{-2} at –10 °C to –55.5 Wm^{-2} at 10 °C. This temperature gradient leads to a substantially higher thermal loss at lower ambient conditions. Wind speed and terrain type also influence heat flux, but to a lesser degree. At 10 ms^{-1}, the average heat loss is –82.2 Wm^{-2}, compared to –69.8 Wm^{-2} at 0.4 ms^{-1}. Among ground conditions, Snow and Soil lead to the highest losses (–84.3 and –83.2 Wm^{-2}, respectively), while Air results in the lowest heat flux values (–61.3 Wm^{-2}). These patterns are confirmed by variance analysis (Table 3.6). Ambient temperature accounts for 62.2% of the total heat flux variance, making it by far the most influential factor. Terrain explains 13.9% of the variance, while wind speed contributes only 0.98%, suggesting that under the studied conditions, wind plays a minor role compared to temperature and ground contact. To explore possible interaction effects, the average heat flux was also calculated for each combination of ground×wind (Table 3.7). The results suggest non-linear and condition-specific trends: for instance, Snow and Soil show a progressive increase in heat loss with higher wind speeds, whereas Air remains relatively insensitive to changes in wind, likely due to the absence of conductive contact with the ground.

Table 3.5 Average of the Heat Flux for each variable

Parameter	**Category**	**Avg Heat Flux** (Wm^{-2})
Temperature	–10 °C	–95.9
	0 °C	–73.1
	10 °C	–55.5
Wind Speed	0.4 ms^{-1}	–69.8
	1.0 ms^{-1}	–72.6
	10.0 ms^{-1}	–82.2
Ground	Air	–61.3
	Snow	–84.3
	Soil	–83.2
	Stiff	–70.4

Table 3.6 Variance of the Heat Flux for each parameter

Parameter	**Variance (%)**
Temperature	62.2
Ground type	13.9
Wind speed	1.0

Table 3.7 Average of the Heat Flux for different combinations of ground type and wind speed

Ground type	**0.4** ms^{-1}	**1.0** ms^{-1}	**10.0** ms^{-1}
Air	–56.7	–55.7	–71.7
Snow	–81.0	–83.7	–88.3
Soil	–77.7	–83.3	–88.7
Stiff	–63.7	–67.7	–80.0

3.5 Conclusions

In this chapter, the validation of the numerical approach was demonstrated by comparing the simulation results with tests on human subjects and thermal manikins. The agreement between the simulated and experimental $\mathrm{R_{cT}}$ values confirmed the reliability of this method for quantifying the thermal performance of the system. The model successfully captured all relevant heat transfer mechanisms, emphasising the air gap between the boot and the foot as a crucial factor. Optimising the geometry, in particular, matching the internal air volume to the experimental results, highlighted the importance of constructing a realistic representation of the physical conditions inside the boot rather than relying on oversimplifications.

Despite efforts to maximise accuracy in terms of material composition and geometry, certain simplifications were necessary to achieve a balance between model complexity, accuracy and computational cost. For example, convective heat transfer was modelled using an effective heat transfer coefficient instead of explicitly simulating airflow. In addition, elements such as the external gaiter and the laces were excluded from the geometry. Moreover, the air layer was modelled as quiescent gas pockets, ignoring the effect of microcirculation. Although these assumptions may affect the system to some extent, they were considered acceptable given the strong agreement with the experimental data and the adaptability of the model in an industrial prototyping context.

The main objective of this study was achieved: a computational system capable of integrating custom material compositions into a new prototype and generating a quantitative parameter (thermal resistance) that can be used to differentiate between models based on their thermal performance. Not only can the model be used to investigate how the thermal behaviour of the system changes when the composition of certain areas is altered, but it also enables analysis under different environmental scenarios, including realistic conditions reminiscent of mountaineering expeditions. In addition, the model allowed a detailed investigation of the contributions of the different heat transfer mechanisms. It was found that conductive heat transfer through the sole dominated in most scenarios (i.e. across different ground types), while convective heat transfer was more influenced by wind speed than by large variations in ambient temperature.

Following the successful development of this second approach to assessing the thermal performance of cold weather footwear, the study moved on to the final objective of the project: to use the calculated thermal resistance of the boot to predict more physiological responses, such as the temperature drop in specific areas of the body (particularly the skin) under specific environmental conditions.

References

Bianca, E., Buffo, A., Vanni, M., Ferri, A., 2025a. Optimizing thermal insulation in footwear: A numerical simulation approach with cad modeling. International Journal of Thermal Sciences 218, 110110.

Bianca, E., Dotti, F., Ferri, A., Havenith, G., 2025b. Heat and mass transfer in footwear: Exploring the moisture evaporation and condensation cycle 55, 15280837251325783. URL: https://doi.org/10.1177/15280837251325783, doi:10.1177/15280837251325783.

Bianca, E., Dotti, F., Orrico, F., Ferri, A., 2024. Thermoregulation of feet in cold environments: A study on alpinism 116. URL: https://www-sciencedirect-com.ezproxy.biblio.polito.it/science/article/pii/S0003687023002430?dgcid=author, doi:10.1016/j.apergo.2023.104205.

Cengel, Y.A., 2002. Heat Transfer: A Practical Approach. McGraw-Hill.

Covill, D., Guan, Z., Bailey, M., Pope, D., 2008. Finite Element Analysis of the Heat Transfer in Footwear (P186), in: Estivalet, M., Brisson, P. (Eds.), The Engineering of Sport 7, Springer. pp. 247–254. doi:10.1007/978-2-287-09413-2_30.

Covill, D., Guan, Z.W., Bailey, M., Raval, H., 2010. Development of thermal models of footwear using finite element analysis 1, 1–14. URL: http://sdj.sagepub.com/lookup/10.1243/09544119JEIM860, doi:10.1243/09544119JEIM860.

Frey, P.J., George, P.L., 2000. Mesh Generation: Application to Finite Elements. Wiley.

ISO, 1997. BS EN ISO 5084:1997 textiles. determination of the thickness of textiles and textile products.

ISO, 2004. BS EN ISO 15831:2004 Clothing. Physiological effects. Measurement of thermal insulation by means of a thermal manikin. URL: https://www.iso.org/standard/28720.html.

ISO, 2007. ISO 9920:2007 - Ergonomics of the thermal environment — Estimation of thermal insulation and water vapour resistance of a clothing ensemble. URL: https://www.iso.org/standard/39257.html.

ISO, 2021. BS EN ISO 20344:2021 Personal protective equipment. Test methods for footwear. URL: https://bsol-bsigroup-com.ezproxy.biblio.polito.it/Bibliographic/BibliographicInfoData/000000000030382286.

Manual, U., 2009. Ansys fluent 12.0. Theory Guide 67.

Oden, J.T., Carey, G.F., 1984. Finite Elements: Mathematical Aspects. Prentice Hall.

Parsons, K., 2014. Human Thermal Environments: The Effects of Hot, Moderate, and Cold Environments on Human Health, Comfort, and Performance, Third Edition. 3 ed., CRC Press. doi:`10.1201/b16750`.

Santee, W.R., William, M., 2012. Evaluation of the thermal environment, in: Military Quantitative Physiology: Problems and Concepts in Military Operational Medicine.

Sturm, M., Perovich, D.K., Holmgren, J., 2002. Thermal conductivity and heat transfer through the snow on the ice of the Beaufort Sea 107, SHE 19–1–SHE 19–17. URL: https://onlinelibrary.wiley.com/doi/abs/10.1029/2000JC000409, doi:`10.1029/2000JC000409`.

Tian, M., Wang, Z., Li, J., 2016. 3D numerical simulation of heat transfer through simplified protective clothing during fire exposure by CFD 93, 314–321. URL: https://www.sciencedirect.com/science/article/pii/S001793101530017X, doi:`10.1016/j.ijheatmasstransfer.2015.09.027`.

West, A.M., Tarrier, J., Hodder, S., Havenith, G., 2019. Sweat distribution and perceived wetness across the human foot: The effect of shoes and exercise intensity 62, 1450–1461. doi:`10.1080/00140139.2019.1657185`, `arXiv:31422758`.

Zhang, N., Wang, Z., 2017. Review of soil thermal conductivity and predictive models 117, 172–183. URL: https://www.sciencedirect.com/science/article/pii/S1290072916315228, doi:`10.1016/j.ijthermalsci.2017.03.013`.

Chapter 4

Data-Based Approach

In this chapter, two complementary modelling strategies are investigated. The first was based on the SARIMAX approach, which is a classical statistical framework for time series predictions. Its performance was compared with that of a recurrent neural network (LSTM), which was developed specifically for capturing non-linear and non-stationary dynamics. The comparison not only highlights the limitations of conventional autoregressive models in representing physiological cooling processes, but also shows the potential of deep learning in recognizing subject-specific and transient patterns.

To make the prediction framework applicable to new scenarios without the need for individual measurements, the data-driven model was combined with a thermoregulation model capable of estimating mean skin temperature as a function of activity and environmental conditions. In this way, the prediction of toe temperature can be extended to conditions of practical interest, bridging the gap between experimental observations and future applications in evaluating the performance of footwear and the safety of users in cold environments.

Part of the work described in this chapter has been previously published in Bianca et al. (2025).

4.1 Purpose of the study

Due to the strong correlation between mean skin temperature and big toe temperature, various approaches for predicting toe temperature from skin temperature data have been explored. As a first step, multiple linear regression was performed to assess the potential of a simple statistical model to predict big toe temperature based on the available characteristics. The analysis revealed low accuracy and poor generalisability, indicating the presence of non-linear and time-dependent dynamics. These results justified the application of more complex and comprehensive models capable of capturing the complex thermal behaviour over time.

On of the most significant approaches relied on a statistical time series model, SARIMAX, which can capture autoregressive dynamics while including exogenous regressors such as ambient temperature, physical activity and thermal resistance of footwear (Elshewey et al., 2023; Kim et al., 2022). The reason for this choice was the model's ability to account for temporal dependencies and explicitly incorporate external factors that influence toe temperature. Although SARIMAX provides a suitable framework for such dependencies, the assumptions and structure of the model are not fully compatible with the goal of predicting individual, transient cooling dynamics. For this reason, alternative approaches capable of modelling non-linear and non-stationary temporal patterns were sought, leading to the introduction of recurrent neural networks (De Saa and Ranathunga, 2020; Guan et al., 2019; Lai and Dzombak, 2020).

Given the strong temporal dependencies in the dataset, RNNs proved to be suitable candidates (Nketiah et al., 2023). A major limitation of standard RNNs is the *vanishing gradient problem*: during backpropagation over time, gradients can decay exponentially, leading to negligible weight updates and difficulties in capturing long-term dependencies. This problem is effectively addressed by Long Short-Term Memory (LSTM) networks (Lipton et al., 2015; Mienye et al., 2024), a type of RNN capable of preserving information over longer time periods. LSTM units differ from classical RNN cells in that they contain a memory cell and a series of gating mechanisms- input, output and forget gates- that regulate the flow of information. These gates allow the network to selectively retain, update or discard information at each time step, mitigating vanishing and exploding gradients and enabling the modelling of complex temporal dynamics.

Beyond the specific case of predicting toe temperature, time series models based on recurrent neural networks have been widely used to monitor physiological parameters. Examples include the prediction of stress levels using LSTM networks and wearable sensors (Acikmese and Alptekin, 2019), the detection of stress using CNN-LSTM architectures (Tanwar et al., 2022), the prediction of body temperature (Han et al., 2024; Liang et al., 2021), and the non-contact monitoring of body temperature by combining machine learning and computer vision (Rida et al., 2023). These studies demonstrate the versatility of recurrent architectures in capturing complex, time-dependent physiological dynamics, which supports their suitability for personalised thermal monitoring applications.

4.2 Autoregressive Time Series Model (SARIMAX)

4.2.1 Data Preparation for Autoregression

The dataset used for the autoregressive modelling was structured as a multivariate time series containing the measured big toe temperature as the dependent variable and three exogenous regressors: the ambient temperature (T_{amb}), physical activity (PA), and footwear thermal resistance (R_{cT}). These variables were selected based on their direct physiological or environmental significance for heat exchange at the extremities.

Each experimental trial resulted in a sequence of 70 minutes, which were sampled at 10-second intervals, resulting in a total of 420 values each. All sequences were concatenated across participants and experimental conditions to form the input for the SARIMAX model. As autoregressive models typically assume stationarity of the underlying process, preparatory transformations such as differencing and detrending were applied to reduce the influence of global trends in the data. However, due to the non-stationary nature of the cooling trends, perfect stationarity could not be achieved.

For the model estimation, the data set was split into training and test. The training dataset included the majority of available sequences (80%), while a subset of participants and conditions was retained for testing to assess the generalisation ability of the model (20%). To encode inter-individual variability, participant identity was treated as a pseudo-seasonal component with a cycle length equal to the number of sequences per subject. This allowed the SARIMAX model to capture recurrent subject-related effects, though at the expense of introducing an artificial seasonal structure. For practical purposes, each experimental configuration was encoded as a tuple: (R_{cT}, PA, T_{amb})

4.2.2 Model Construction

The autoregressive framework was implemented using the SARIMAX formulation from the library `statsmodels` in Python. In order to determine the most suitable model structure, a grid search procedure was carried out using various parameter combinations. The non-seasonal autoregressive, differencing, and moving average

Table 4.1 Summary of experimental conditions used for autoregressive modelling. Each sequence is characterised by the dependent variable (big toe temperature) and three exogenous regressors: footwear model (R_{cT}), physical activity (PA), and ambient temperature (T_{amb}).

Condition	Footwear model (R_{cT})	PA level	T_{amb} [°C]
1	A	0 (stillness)	-10
2	A	1 (light walking)	-10
3	A	0 (stillness)	-17
4	A	1 (light walking)	-17
5	C	2 (intense activity)	-15
6	B	2 (intense activity)	-20
7	D	1 (light walking)	-13
8	E	1 (light walking)	-13
9	D	0 (stillness)	-13
10	E	0 (stillness)	-13

terms (p, d, q) were analysed in the range [0, 2]. These parameters correspond, respectively, to the autoregressive order (AR), the degree of differencing required to achieve stationarity (I), and the moving average order (MA) (Box et al., 2015). The AR term p captures the influence of past values of the series on the current observation, whereas the MA term q models the effect of past forecast errors. Differencing, indicated by d, is applied to remove trends and render the series approximately stationary.

Similarly, the seasonal components (P, D, Q, s) were analysed in the same ranges. The seasonal parameters P, D, and Q represent the seasonal counterparts of the AR, I, and MA terms, respectively, while s denotes the length of the seasonal period. In the present study, s was set equal to 70, corresponding to the 70-minute observation window, to accommodate the pseudo-seasonal structure introduced to encode inter-individual variability.

The Akaike Information Criterion (AIC), which balances model fit and complexity, was used as the evaluation criterion for model selection. Each candidate model was estimated, including the exogenous regressors (skin temperature, ambient temperature, and footwear resistance), and the configuration with the lowest AIC was selected for subsequent validation.

4.2.3 Model Validation and Evaluation

The predictive performance of the selected SARIMAX model was evaluated using standard forecast accuracy metrics. In particular, the Root Mean Square Error (RMSE) and Mean Absolute Error (MAE) between the predicted and observed big toe temperature series were calculated for each experimental condition. These metrics provide distinct information: the RMSE penalises larger deviations more heavily, while the MAE provides a robust average value of the error magnitude.

In addition, the ability of the model to capture the temporal dynamics relevant to physiological thresholds was assessed by comparing the predicted and observed times at which the big toe temperature crossed 15°C. This time-to-threshold is particularly important in the context of cold exposure as it reflects the onset of potential discomfort or risk, and is a more informative metric regarding user safety with which to evaluate the performance of the end product. Furthermore, as already defined in Section 2.1, the time required to reach the threshold in a certain condition and with a specific footwear insulation is converted into a parameter called *Duration of Safe Exposure*.

Overall, while the SARIMAX framework provided a structured and interpretable approach, forecast accuracy was limited in capturing individual-specific transient cooling behaviour, motivating subsequent exploration of recurrent neural network models.

4.3 Deep Learning Model

4.3.1 Data Preparation for Deep Learning

The data collected during the experimental campaigns (Bianca et al., 2024) were organised in temporal arrays of 70 minutes in length, corresponding to 420 time steps (with a sampling frequency of one data point every 10 seconds). Each sample array corresponds to a single test performed by a subject under a specific combination of experimental conditions. Each array was labelled according to three parameters: ambient temperature (T_a), thermal insulation of the boot model (R_{cT}), and level of physical activity (0 for stillness, 1 for light exertion, and 2 for demanding physical activity).

The data were clipped to remove anomalous values. `MinMax` scaling normalization was then applied as it was found to be more effective in dealing with noisy temporal data compared to other normalization techniques. The neural network was structured to receive the following input (X) and generate the corresponding output (Y):

- X: a three-dimensional matrix of the shape [batch size, 420, 4], where the four features are: mean skin temperature, T_a, R_{cT}, and level of physical activity (PA).
- Y: the time series of big toe temperature, shaped as [batch size, 420, 1], which represents the predicted temperature of the big toe over time.

4.3.2 Model Construction

Hyperparameter tuning was performed using Keras Tuner's Hyperband algorithm. This method, introduced by Jamieson and Talwalkar (Jamieson and Talwalkar, 2016; Li et al., 2018), differs from traditional optimisation techniques such as Bayesian optimisation in that it exploits the iterative nature of training algorithms to adaptively allocate computational resources and stop poorly performing configurations early. In contrast to Bayesian methods, which often allocate fixed budgets and treat the model as a black box, Hyperband dynamically adapts resource allocation, enabling much faster convergence. This approach is particularly beneficial when model training is computationally intensive, as it speeds up the identification of promising

hyperparameters without requiring assumptions on convergence rates, making it highly scalable and practical for real-world applications.
In our case, the tuned hyperparameters included:

- Number of LSTM layers
- Number of LSTM units per layer
- Number of fully connected (dense) layers and units, to refine the output after temporal processing
- Dropout rate optionally applied after the LSTM layers to prevent overfitting due to random deactivation of units during training
- Learning rate, which influences convergence speed and stability

The hyperparameter tuning process was implemented by defining a custom `HyperModel` class for Keras Tuner to explore different LSTM architectures and training configurations. For optimisation, the Adam optimiser was used with an adjustable learning rate sampled logarithmically between 10^{-7} and 10^{-3}. Gradient clipping was applied with a norm threshold of 1.0 to improve training stability and prevent exploding gradients that can occur in deep recurrent networks. Hyperband was used as the search algorithm with a maximum of 100 epochs per configuration (found in bespoke manual testing to provide a sufficiently balanced higher threshold to reach acceptable loss accuracy), and a reduction factor of 3. The reduction factor controls how Hyperband divides the resources among the candidate configurations. At each iteration, only the top third of the models are kept for further training, while the remaining two-thirds are discarded.
An early stop was performed for 15 epochs to terminate poor-performing trials and restore the best weights. The tuner was then run on the scaled input and output data using a validation split of 20%, and the best hyperparameters and model were selected based on the validation loss.
The best configurations identified through this process formed the basis for the final model architecture, which is described in detail in the following section.

4.3.3 Model Validation and Evaluation

To evaluate our model, a subject-centred validation strategy was chosen. In this approach, all data from a given participant were fully assigned to either the training set or the test set, meaning for all of their related environmental, phisiological, or footwear insulation. This ensures that the network is evaluated on individuals it has never seen before, allowing for a more robust assessment of its ability to generalise to new subjects. To ensure a robust evaluation of model performance, we used a Leave-One-Subject-Out (LOSO) cross-validation strategy. In LOSO, for each condition, one subject's data is retained as the test set while all other subjects' data is used for training.

Since the topic deals with time series, the performance metrics were evaluated as a function of time. Specifically, we calculated both the mean difference and the mean square difference between the model predictions and the ground truth at each time point to capture the evolution of errors over the entire time horizon.

In addition to the conventional loss metrics, we developed a custom loss function to assess the ability of the model to predict the time at which the big toe temperature falls below the critical threshold of 15°C. The mean square standard error (MSE) penalises the differences between the predicted and measured temperature values over the entire time sequence, but does not explicitly capture the accuracy of the predicted time at which the critical threshold is exceeded. As this point in time is particularly relevant for thermal comfort and risk assessment, an additional component was included in the loss function. The first step was to define a differentiable function, referred to here as a *Differentiable Threshold-Crossing* (DTC) function, which estimates the index of the first time step at which the temperature sequence falls below the defined threshold. With this operator, the problem of recognising a discrete crossing event is transformed into a continuous and differentiable operation, which allows its integration into the gradient-based training of the neural network. The DTC function provides the predicted crossing time (expressed in minutes after normalisation of the time axis), both for the ground truth and for the model output. A threshold-related loss component was then defined as the squared difference between the predicted and actual threshold crossing time. The final custom loss function combined the conventional MSE term, which ensures accurate prediction of the entire temperature curve, with this additional threshold component weighted by an adjustable coefficient α.

For each temperature sequence $y = (y_1, \ldots, y_T)$, the first time step at which the temperature falls below the threshold value τ is estimated. This is achieved by defining a masked variable:

$$m_t = \begin{cases} \mathrm{t}, & \text{if } y_t \leq \tau \\ \mathrm{T}, & \text{otherwise} \end{cases} \quad \text{for t} = 1, \ldots, \mathrm{T} \tag{4.1}$$

The crossing time is then the minimum value of the masked sequence:

$$\mathrm{t_{cross}} = \min_{t=1,\ldots,T} m_t \tag{4.2}$$

To match the assumed unit of time (minutes), the index is converted using a scaling factor κ:

$$\hat{\mathrm{t}} = \frac{\mathrm{t_{cross}}}{\kappa} \tag{4.3}$$

with $\kappa = 6$, as each time step corresponds to 10 seconds. If the measured or predicted temperature curve does not fall below the threshold value of 15°C, the crossing time is set to the maximum observation period of 70 minutes.
The loss term associated with crossing the threshold is defined as follows

$$\mathscr{L}_{\text{threshold}} = \left(\hat{\mathrm{t}}_{\text{pred}} - \hat{\mathrm{t}}_{\text{true}}\right)^2 \tag{4.4}$$

Finally, the general user-defined loss function combines the mean squared error (MSE) over the entire sequence with the threshold-related component, weighted by a factor α:

$$\mathscr{L} = \underbrace{\frac{1}{NT} \sum_{i=1}^{N} \sum_{t=1}^{T} \left(y_{i,t}^{\text{true}} - y_{i,t}^{\text{pred}}\right)^2}_{\text{MSE of predicted curve}} + \underbrace{\alpha \frac{1}{N} \sum_{i=1}^{N} \left(t_i^{\text{true}} - t_i^{\text{pred}}\right)^2}_{\text{time-to-threshold component}} \tag{4.5}$$

where:

- N is the number of sequences in the batch,
- T is the number of time steps in each sequence,

- $y_{i,t}^{\text{true}}$ and $y_{i,t}^{\text{pred}}$ denote the true and predicted temperature at time step t for sequence i,
- t_i^{true} and t_i^{pred} are the true and predicted times (in minutes) at which the temperature first falls below the threshold,
- α is a weighting factor controlling the relative importance of the two components.

This formulation ensures that the model learns to reproduce the overall temperature dynamics while explicitly aligning the prediction of the physiologically critical threshold-crossing time.

Once the model was built, trained, and tested against the experimental data, we further evaluated its classification performance using accuracy, precision, and recall metrics. These metrics were applied to assess the model's ability to correctly classify whether or not the temperature crossed the 15°C threshold in a physiologically plausible time frame.

The *Accuracy* measures the overall proportion of correct classifications, both positive and negative. It is defined as:

$$\text{Accuracy} = \frac{\text{TP} + \text{TN}}{\text{TP} + \text{TN} + \text{FP} + \text{FN}} \tag{4.6}$$

Where TP denotes true positives, TN true negatives, FP false positives, and FN false negatives. In the context of our time-series prediction problem, these terms were defined based on whether the model correctly predicted the threshold-crossing event within a tolerance of ±10 minutes. This window was chosen to account for inter-subject variability observed in the experimental trials. Table 4.2 summarizes the specific criteria used for classification:

To ensure that model evaluation was not biased by class imbalance, the *Precision* was also considered, and it was defined as the proportion of true positive predictions among all predicted positives:

$$\text{Precision} = \frac{\text{TP}}{\text{TP} + \text{FP}} \tag{4.7}$$

Classification	**Definition**
TP	The predicted curve crosses the threshold within ±10 minutes of the experimental crossing time.
TN	Neither the predicted nor the experimental curves cross the threshold.
FP	The predicted curve crosses the threshold (earlier than 10 minutes before test end), but the experimental curve does not.
FN	The predicted curve does not cross the threshold, but the experimental one does.

Table 4.2 Definition of classification outcomes for model performance evaluation.

Finally, the *Recall* (also known as sensitivity) was computed to measure the proportion of actual positive cases correctly identified by the model:

$$\text{Recall} = \frac{\text{TP}}{\text{TP} + \text{FN}} \tag{4.8}$$

To complement accuracy-based evaluation, the F1-score was used as a summary metric combining precision and recall into a single indicator of event-detection performance. The F1-score is defined as the harmonic mean of precision and recall:

$$\text{F1} = \frac{2 \cdot \text{Precision} \cdot \text{Recall}}{\text{Precision} + \text{Recall}} \tag{4.9}$$

This metric is particularly suitable for threshold-crossing detection tasks, where the number of critical events is limited and false positives and false negatives have different practical implications.

Overall, the proposed architecture integrates both continuous temperature prediction and discrete event detection, providing a comprehensive framework for assessing thermal comfort and cold protection performance.

4.4 Mean Skin Temperature from JOS-3 Model

The main aim of developing this tool is to create a system capable of predicting the performance of a prototype before its actual production. This objective aligns with the digital system described and illustrated in Chapter 3, but contrasts with the use of experimental mean skin temperature data to predict big toe temperature. Therefore, once the model is trained and validated, its application should rely on synthetic mean skin temperature data based on the same variables used in the experimental case (ambient temperature, physical activity, and footwear insulation level). This is where thermoregulation models are useful.

Thermoregulation models predict the physiological response of humans when exposed to a thermal environment. The formulation of these models is not straightforward, as they must represent the biological system, whose overall behaviour is known, but not that of each individual component (i.e., body areas) (Lopardo, 2011). Since the beginning of the last century, many advances have been made in this field, classified into qualitative, more descriptive models, and quantitative models, which allow the evaluation of specific quantities (Hardy, 1972). In particular, the model chosen to address the issue of data availability was JOS-3.

JOS-3 is a thermoregulation model that was built as a further development of the already existing JOS-2, which in turn is based on the fundamental Stolwijk model (Takahashi et al., 2021). The model represents the human body through 85 discrete nodes: a central blood node, 17 arterial nodes, 17 venous nodes, 12 superficial venous nodes, 17 nuclear nodes, 2 muscle nodes, 2 fat nodes and 17 skin nodes. These nodes correspond to 17 body segments: head, neck, chest, back, pelvis, left (L)-shoulder, L-arm, L-hand, right (R)-shoulder, R-arm, R-hand, L-thigh, L-leg, L-foot, R-thigh, R-leg and R-foot.

JOS-3 simulates the human thermoregulatory response using a finite difference method and is able to predict both global (e.g. mean skin temperature) and local thermal states of the body. Although the model can estimate foot temperature, it treats the foot as a uniform segment and does not distinguish between critical subregions, such as the toes, which are more susceptible to cold injuries such as frostbite. Although physiological mechanisms like vasoconstriction and arteriovenous anastomoses (AVA) are taken into account, the model is not suitable for direct estimation of toe temperature due to the lack of spatial resolution in the distal extremities.

For this reason, the mean skin temperature predicted by JOS-3 was used as input by the deep learning model to predict the corresponding toe temperature. The JOS-3 simulations were configured to reproduce the same conditions as the experimental trials in terms of subject characteristics (e.g., body mass, height) and clothing composition. This made it possible to evaluate thermoregulatory behaviour under different environmental conditions and activity levels.

In addition, the results of JOS-3 were validated using selected data collected during the human trials to verify the accuracy of the model under the test scenarios. The use of JOS-3 mean skin temperature was necessary once the LSTM was successfully trained, since it would have made possible to predict big toe temperature in different scenarios than the one tested, starting from the temporal series of the skin temperature.

Having successfully trained the LSTM on real data (i.e., time series of skin and big toe temperature), the use of JOS-3 opens up the possibility of creating skin temperature profiles for untested, transient scenarios. This makes it possible to derive the temperature of the big toe under a variety of untested conditions, such as new climate, activity, and clothing combinations, by using the LSTM as a surrogate model fed by the synthetic skin temperature sequences generated by JOS-3.

4.5 Results and Discussion

4.5.1 Final Model Architecture

The final LSTM model, selected by optimising the hyperparameters, consists of two recurrent layers followed by a small feedforward block. To improve training stability and avoid the systematic underestimation observed at the beginning of some predicted sequences, where the model initially assumed unrealistically low temperature values and then gradually corrected itself, the hidden and cell states of the first LSTM layer were initialised to a realistic value by mapping the first measured big toe temperature through two dense layers of 384 units and `tanh` activation (Karim et al., 2017; Kemeth et al., 2021). By providing a meaningful initial state derived from the first measurement, the network is better guided at the start of each sequence, reducing the size of this initial error and improving the fit to the measured curve. This approach ensures that the LSTM has a physically meaningful starting point, which is particularly important given the strong temporal correlation of the toe temperature data.

The first LSTM layer contains 384 units and provides sequences to enable temporal processing by the subsequent layer. The second LSTM layer has 256 units and also returns sequences. A dropout of 5% is applied after the LSTM layers to avoid overfitting. After the recurrent layers, a dense layer with 80 units and `tanh` activation refines the output before the final prediction. The output layer is a single neuron with linear activation that produces the predicted big toe temperature at each time step. Figure 4.1 shows the final structure used for big toe prediction.

The model is trained using the Adam optimiser with the previously defined custom loss function combining the mean squared error over the sequence and the threshold component. Metrics monitored during training include the mean absolute error and the threshold component, which provide insight into both the overall curve accuracy and the prediction of the critical transition time point.

Figure 4.2 illustrates the training dynamics of the final LSTM model. The total loss as well as its components (MAE and threshold error) decreased rapidly in the first epochs and gradually stabilised, indicating an effective convergence of the model.

The validation curves closely followed the training curves, indicating that overfitting

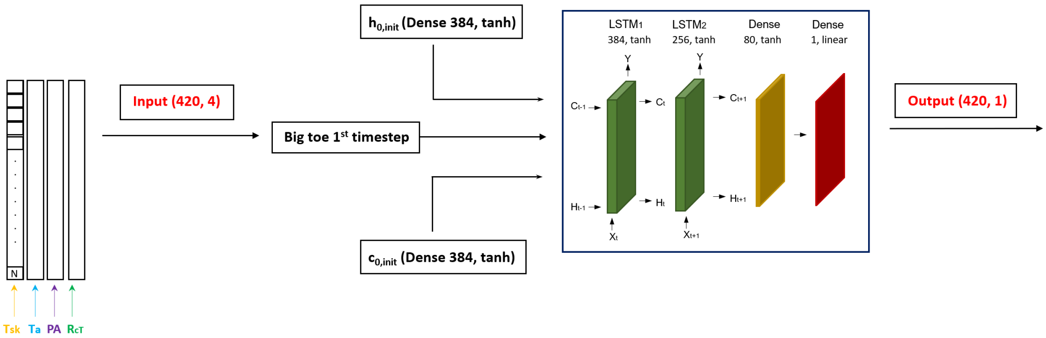

Fig. 4.1 Compact schematic of the final LSTM model for big toe temperature prediction, including hidden and cell state initialization from the first measured value.

was limited and that the network could be generalised quite well to unseen data. In particular, the component regarding the estimation of the time to reach the safety threshold eventually gets to values lower than 10 minutes, emphasising the ability of the model to capture the time of threshold crossing with reasonable precision. The learning rate scheme, shown in the right panel, demonstrates the effect of the stepwise reduction strategy: each reduction in learning rate was accompanied by a further reduction in both training and validation losses, supporting the choice of adaptive optimisation to stabilise the training process. Overall, the curves confirm the robustness of the final architecture and training procedure before we move on to evaluate the prediction performance.

4.5.2 SARIMAX and LSTM comparison

4.5.2.1 SARIMAX performance

The first approach to predicting big toe temperature using the SARIMAX model revealed several limitations inherent to its assumptions. SARIMAX assumes that the underlying process is stationary or can be made stationary by differentiation, which is rarely the case for physiological cooling trajectories that exhibit non-linear and non-stationary dynamics. Additionally, the model is fundamentally designed to capture recurrent seasonal or cyclical behaviour, whereas the evolution of toe temperature in cold environments is a transient and non-periodic process. A further limitation arises from the encoding of participant identity: inter-individual variability was artificially represented as a seasonal component, which does not correspond to

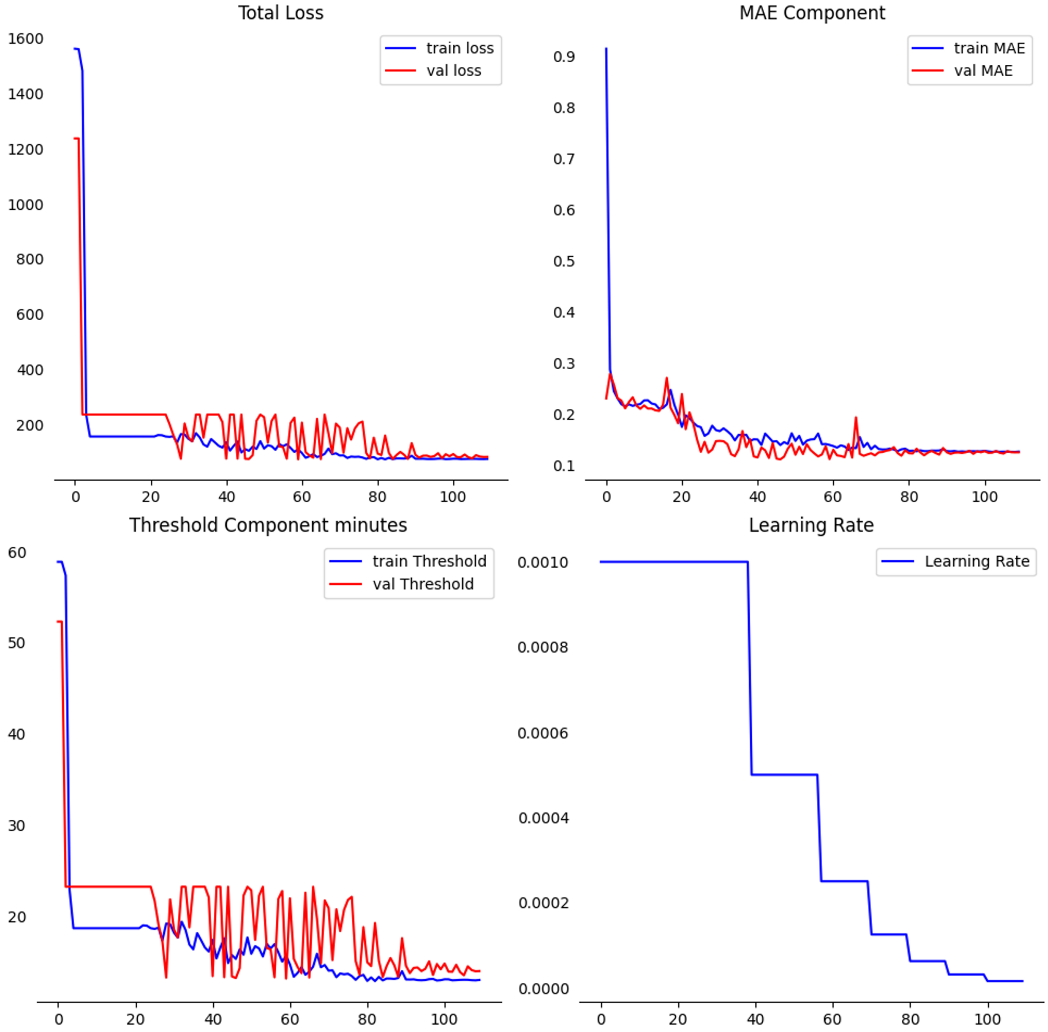

Fig. 4.2 Metrics regarding the training of the LSTM. The loss has been evaluated both overall and in its individual components to assess the behaviour of each better.

any physiological periodicity. This approach reduced interpretability and impaired generalisation to unseen subjects.
Table 4.3 highlights that mean skin temperature was the only strongly significant predictor (coef. = 1.27, $p < 0.001$).

In contrast, most terms of the moving average (MA lag-1 and lag-2 as well as the seasonal MA terms) were not significant, indicating a low ability of the model to capture short-term dependencies. The seasonal autoregressive terms at lags 70 and 140, although statistically significant, reflect the artificial seasonal structure introduced to encode inter-individual variability. In reality, subjects do not exhibit

Table 4.3 Estimated parameters of the SARIMAX model with skin temperature as exogenous regressor.

Parameter	**Coef.**	**Std. Err.**	**z**	**P> $\lvert z \rvert$**	**[0.025, 0.975]**
skin_temp	1.27	0.01	159.69	0.000	[1.26, 1.29]
ma.L1	0.05	0.04	1.29	0.197	[-0.03, 0.13]
ma.L2	0.03	0.09	0.30	0.764	[-0.14, 0.19]
ar.S.L70	-1.12	0.01	-180.10	0.000	[-1.13, -1.11]
ar.S.L140	-0.17	0.01	-26.89	0.000	[-0.18, -0.16]
ma.S.L70	0.0000	80.08	0.00	1.000	[-156.96, 156.96]
ma.S.L140	-1.00	51.56	-0.02	0.985	[-102.06, 100.06]
σ^2	0.30	15.34	0.02	0.985	[-29.77, 30.36]

periodic behaviour at these intervals, and therefore these terms have no physiological justification. Their significance arises purely from the modelling setup, not from underlying biological patterns, highlighting a key limitation of SARIMAX in representing transient and subject-specific cooling dynamics. Finally, the variance parameter σ^2 was highly unstable (estimate = 0.30, p $\approx$ 0.99), suggesting unreliable residual modeling. Overall, the table highlights both the excessive reliance on skin temperature as a linear driver and the inadequacy of the seasonal structure to represent subject-specific dynamics.

Inspection of the results, reported in Table 4.4 shows mixed performance. While certain conditions, such as (A, 1, -10) and (A, 1, -17), were correctly identified as TP with relatively low RMSE and MAE values, other scenarios showed significant deviations. In particular, the time differences ($time_{diff}$) in FN and FP cases reached values of up to 21 minutes, reflecting the limited ability of the model to accurately capture the transient cooling dynamics under varying environmental and activity conditions. Overall, these measurements illustrate that while SARIMAX can capture general trends, it struggles to provide reliable predictions for individual, short-term variations in toe temperature.

Table 4.4 Forecast performance metrics of the SARIMAX model for each condition. *obs_time* and *pred_time* indicate the observed and predicted times to reach 15°C, and *time_diff* their difference. TP = True Positive, FP = False Positive, TN = True Negative, FN = False Negative.

Condition	**RMSE**	**MAE**	**obs_time**	**pred_time**	**time_diff**	**Class.**
(A, 0, -10)	4.90	4.89	49.71	70.00	20.29	FN
(A, 1, -10)	4.24	3.77	70.00	70.00	0.00	TP
(A, 0, -17)	1.62	1.58	39.57	52.75	13.19	Other
(A, 1, -17)	1.43	1.23	70.00	63.91	-6.09	TP
(A, 2, -15)	3.57	3.54	55.80	70.00	14.20	FN
(B, 2, -20)	3.56	3.37	70.00	54.78	-15.22	FP
(D, 1, -13)	3.80	3.77	48.70	70.00	21.30	FN
(E, 1, -13)	2.85	2.85	57.83	70.00	12.17	FN
(D, 0, -13)	2.79	2.78	50.72	70.00	19.28	FN
(E, 0, -13)	2.10	2.05	54.78	70.00	15.22	FN

4.5.2.2 LSTM performance

The predictive performance of the final LSTM model was evaluated using the custom loss function previously defined, which combines the mean squared error (MSE) over the entire sequence with the threshold-related component. Training was conducted with the Adam optimiser, while the mean absolute error (MAE) and the threshold-crossing component were continuously monitored to assess both overall curve accuracy and the model's ability to predict the critical transition point.

The model generally reproduced the temporal evolution of big toe temperature with high fidelity. Table 4.5 summarises the RMSE, MAE, and predicted threshold-crossing times across all tested conditions, along with the corresponding classification outcomes.

True positives (TP) were correctly identified across a variety of ambient temperatures and activity levels, confirming the model's ability to track threshold-crossing events within the observation window. The LSTM performed consistently well across multiple combinations of the three label parameters, ambient temperature, activity level, and footwear insulation (R_{cT}), and not only under monotonic or uniform cooling trends.

Table 4.5 Evaluation metrics for the LSTM model across all tested conditions. Parameter codes are defined in the text. The asterisk (*) indicates cases where the classification was assigned to the closest category according to the timing difference criterion, even though it does not strictly match the formal definition. For instance, condition (A, 1, –17) was labelled as a false positive (FP*) because both the predicted and experimental curves crossed the threshold, but the predicted crossing occurred more than 10 minutes earlier than the ground truth. Similarly, condition (D, 1, –13) was labelled as a false negative (FN*) since both curves reached the threshold, but the predicted event was delayed beyond the ±10-minute tolerance window.

Condition	RMSE	MAE	time_{obs}	time_{pred}	**Δtime**	Class.
(A, 0, –10)	5.74	4.78	70.00	47.61	22.39	FN
(A, 0, –17)	5.15	4.15	38.09	46.28	8.19	TP
(A, 1, –10)	2.81	2.43	70.00	70.00	0.00	TN
(A, 1, –17)	6.52	5.67	69.33	58.83	11.50	FP*
(C, 2, –15)	5.52	4.58	38.76	70.00	31.24	FN
(B, 2, –20)	3.78	3.05	51.96	70.00	18.04	FN
(D, 1, –13)	4.69	3.77	29.40	58.86	29.46	FN*
(E, 1, –13)	5.85	4.88	58.81	66.66	7.85	TP
(D, 0, –13)	5.57	4.53	53.63	45.61	8.02	TP
(E, 0, –13)	6.24	5.14	51.46	50.79	0.67	TP

Overall, the network produced 4 true positives (TP), 1 true negative (TN), 1 false positive (FP), and 4 false negatives (FN), corresponding to an accuracy of 50%, a precision of 67%, and a recall of 57%. These event-based classification metrics are strongly influenced by the limited dataset size and by the strict ±10 min tolerance window adopted to define a correct threshold-crossing prediction.

To provide a more comprehensive assessment of model performance, the classification results were complemented with continuous time-based error metrics. When both the experimental and predicted temperature curves crossed the threshold (i.e., valid crossing events), the mean absolute error of the crossing time was 10.78 min, indicating good temporal alignment between predicted and observed events. In censored cases, where the threshold was reached only in the experimental data and the predicted crossing time was set to the maximum observation duration of 70 min, the mean censored error was 24.64 min.

These results indicate that, even when the threshold event was missed, the predicted temperature trajectories remained physiologically plausible and did not exhibit erratic behaviour.

In addition, a time-to-event tolerance analysis was performed by progressively relaxing the temporal tolerance used to define correct event detection. Figure 4.3 shows the variation of accuracy, precision, and recall as a function of the temporal tolerance τ applied to the predicted threshold-crossing time. A prediction is considered correct if the absolute difference between the predicted and experimental crossing times is smaller than τ. The results demonstrate that the strict ±10 min tolerance used in the main classification represents a conservative criterion; relaxing the tolerance leads to a substantial improvement in event detection performance. This confirms that the moderate accuracy observed under the ±10 min criterion primarily reflects the severity of the evaluation window and the impact of physiological variability, rather than a fundamental limitation of the predictive model.

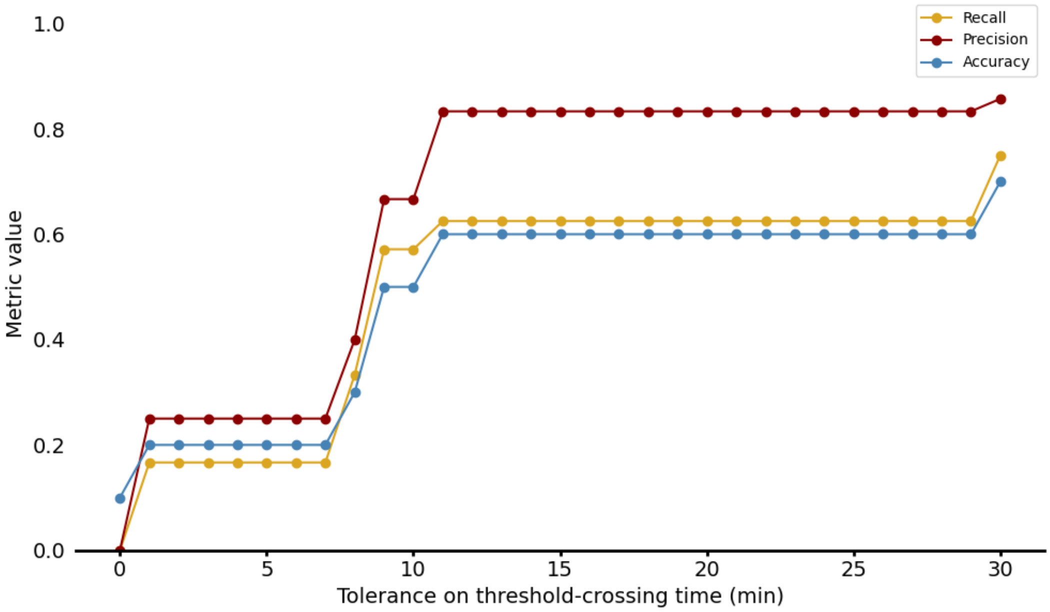

Fig. 4.3 Time-to-event tolerance curve for the threshold-crossing prediction. Accuracy, precision, and recall are shown as a function of the temporal tolerance τ applied to the predicted crossing time.

In addition to accuracy, the F1-score was calculated as a complementary performance metric. By jointly considering precision and recall, the F1-score offers a more informative assessment of threshold-crossing detection than accuracy alone, especially in the presence of class imbalance and a limited number of test cases.

The F1-score, with a value of 62%, confirms that the network achieves a reasonable balance between reliable event detection and sensitivity to true cold-risk conditions.

4.5.2.3 SARIMAX vs LSTM comparison

The classification metrics show a significant improvement of LSTM over SARIMAX in predicting whether the temperature of the big toe would reach the threshold. While SARIMAX achieved a low accuracy of 20% and a recall of only 22%, due to its frequent failure to detect threshold crossings, the LSTM achieved an accuracy of 50% and a recall of 57%, demonstrating a significantly better ability to predict critical cooling events. The precision is also higher for the LSTM (80% compared to 67%), indicating fewer false positive predictions compared to true positive predictions.

The RMSE and MAE metrics for all experimental conditions of the SARIMAX and LSTM models were assessed. For SARIMAX, RMSE values ranged from 2.81 to 6.52 and MAE values from 2.43 to 5.66, with the best performance observed in conditions (A, 0, -17) and (A, 1, -17), where the dynamics were relatively stable. Higher errors occurred under conditions with higher activity or lower ambient temperatures, reflecting the limited ability of the model to capture rapid or complex transient cooling. This is consistent with the fact that SARIMAX relies on a linear autoregressive structure and artificial seasonal encoding of subject variability.

In comparison, the LSTM model showed RMSE values between 1.42 and 4.90 and MAE between 1.23 and 4.89.

Table 4.6 presents a comparison between the two models based on the evaluation parameters used (i.e., MAE, RMSE, accuracy, precision, and recall).

Table 4.6 Comparison of SARIMAX and LSTM performance on big toe temperature prediction (regression metrics and threshold-based classification metrics).

Model	**MAE**	**RMSE**	**Accuracy**	**Precision**	**Recall**
SARIMAX	2.43-5.66	2.81-6.52	0.20	0.67	0.22
LSTM	1.23-4.89	1.42-4.90	0.50	0.80	0.57

Importantly, the LSTM provided more realistic predictions for conditions where SARIMAX could not predict threshold crossings within the observation window. Overall, these results show that the LSTM provides greater robustness in modelling individual transient cooling dynamics under varying environmental and activity

conditions, despite occasionally high point-wise errors.
Overall, the comparison shows that while SARIMAX can capture general skin temperature-dependent trends, it has problems with subject-specific temporal patterns. In contrast, LSTM demonstrates a stronger ability to model these transient, individualized responses, confirming the suitability of deep learning for predicting big toe temperature under various conditions.

4.5.3 Predictive performance of the LSTM

The analysis of the LSTM performance shows that the network responds differently depending on the nature of the cooling dynamics. The LSTM performed well in a wide range of combinations of the three labels (ambient temperature, physical activity, and R_{cT}), and not only under conditions where the temperature decrease followed a uniform and monotonic trend. Examples of accurate predictions are shown in Figure 4.4, where the agreement between measured and predicted curves demonstrates the ability of the network to reproduce both the trajectory and the threshold event.

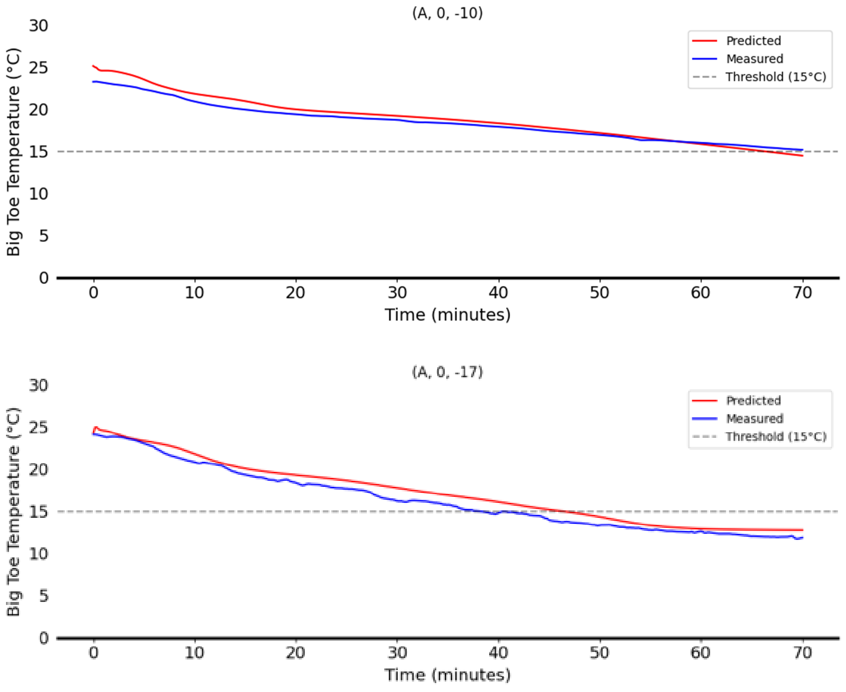

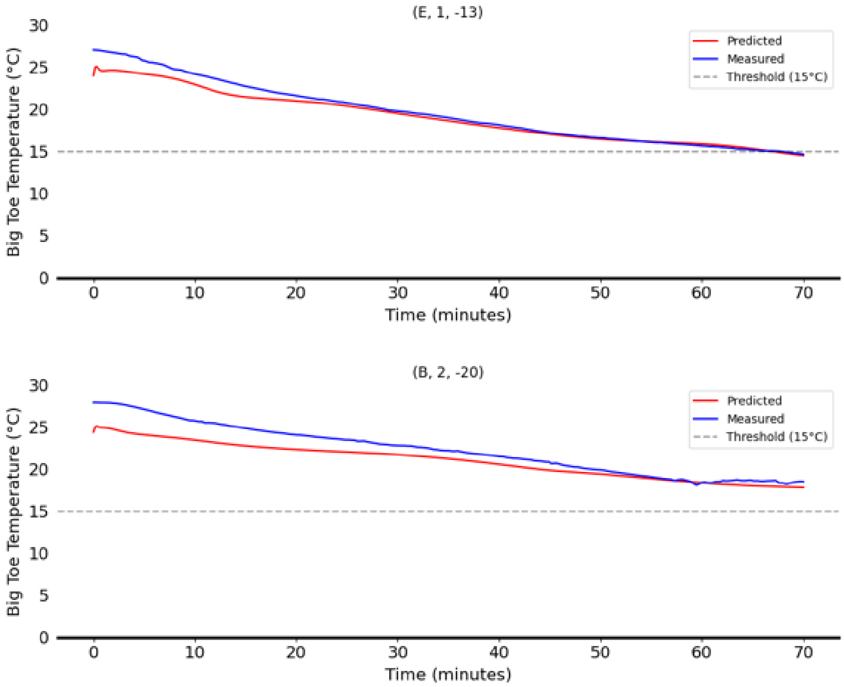

Fig. 4.4 Examples of accurate LSTM predictions (a–d).

In the first few timesteps, the initial slight temperature rise is apparent, then immediately inhibited by the network time process, as explained in Section 4.5.1. In contrast, certain cases exhibited reduced prediction accuracy, as shown in Figure 4.5.

Two specific examples are noteworthy. In the first case, corresponding to (A, 1, -10), the predicted trend did not perfectly overlap with the measured data; however, the overall behaviour was correctly identified, resulting in a True Negative, i.e., an accurate prediction that the threshold was not reached both in the measured and the predicted case. In the second case, corresponding to (C, 2, -15), the prediction was inaccurate in terms of both the shape of the temperature curve and the identification of the threshold crossing, resulting in a False Negative classification. This suggests that although the network encoded the general shape of the curve, it was less able to localise the exact time of the threshold event. Similarly, the conditions categorised as “Other” correspond to situations where the threshold crossing was recognised but delayed, leading to misclassifications despite physiologically plausible trajectories. What can be inferred from this behaviour is that the network’s performance tends to deteriorate under two specific circumstances.

First, reduced accuracy occurs in conditions that were poorly represented in the training set. This is evident in the case of Model C at (C, 2, -15), which was available

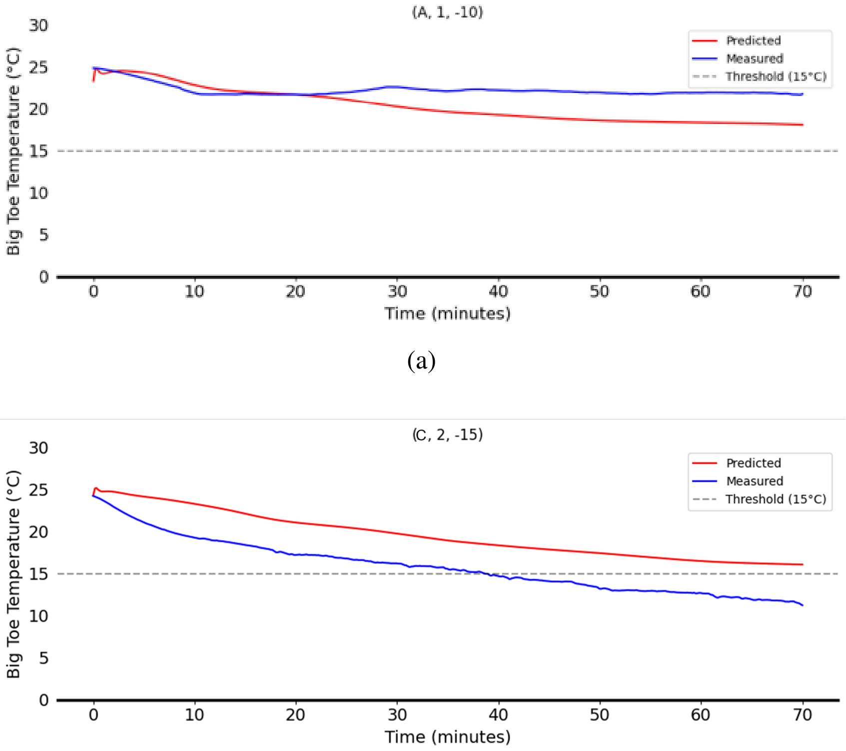

(a)

(b)

Fig. 4.5 Examples of inaccurate prediction performance. In both cases (a) and (b), the threshold crossing was not identified, but the trajectories still reproduced the main trend.

from only one experimental campaign. The network, therefore, lacked sufficient variability to learn the characteristic cooling patterns of this boot configuration, resulting in an incorrect reproduction of the temperature curve and a missed threshold event. Second, performance degradation can occur when the subject used for validation displays an atypical physiological response. This is the case for (A, 1, -10), where the cooling trend of the selected subject deviated substantially from the patterns observed in the rest of the population. Further inspection of the raw data confirmed that this participant exhibited an “unusual” cooling profile compared to others. To verify that this behaviour was subject-specific rather than model-related, the same condition was tested using a different participant, resulting in a correct prediction as shown in Figure 4.6. This confirms that the network had learned the typical behaviour, but struggled in the presence of rare or outlier physiological responses.

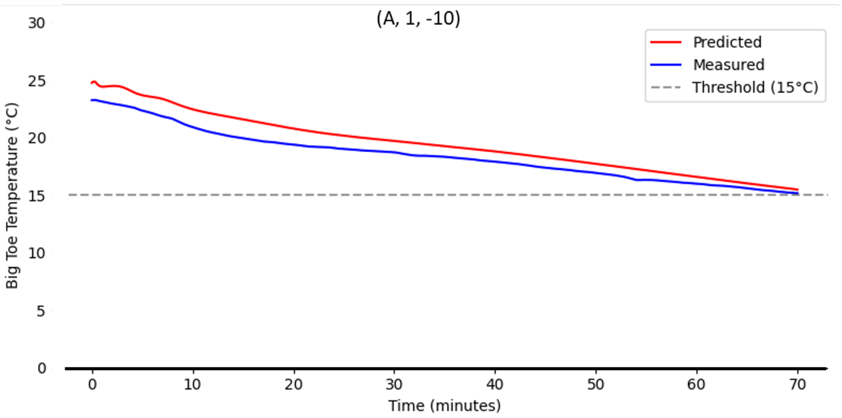

Fig. 4.6 Prediction of condition (A, 1, –10) using a different subject with a typical cooling pattern. Unlike the original case, the network correctly captures the temperature evolution and threshold timing, confirming that the previous error was due to subject-specific variability rather than model inadequacy.

Overall, these findings suggest that the LSTM model performs well when exposed to patterns that are both sufficiently represented in the training data and physiologically consistent across individuals, but its robustness may be challenged by underrepresented conditions or highly atypical subject responses.
From a practical point of view, the complementary use of accuracy, precision, and recall helps to qualify these results. Accuracy reflects the overall reliability of the model across all conditions, precision expresses the confidence of predicted threshold crossings (thereby avoiding false alarms), and recall quantifies the ability to detect all true events (thereby reducing the risk of missing critical cold exposures). Although the absolute values of these indicators remain moderate, their interpretation underlines the trade-off between minimising unnecessary alarms and ensuring robust safety margins in cold environments.

4.5.4 Temperature prediction based on JOS-3

Once the LSTM model has been trained, its main purpose is to predict the Duration of Safe Esposure, defined as the time at which the temperature of the big toe reaches the critical threshold of 15 °C. For this purpose, the network relies on the time series of mean skin temperature provided by the JOS-3 thermoregulation model.
The JOS-3 model generates the skin temperature evolution based on several key inputs. These include environmental conditions such as air temperature, mean radiant

temperature, relative humidity, and air velocity, which can be adjusted to represent different scenarios of cold exposure. The model also requires information about physical activity and posture, which influence metabolic heat production and heat distribution in the body. Another essential input is the clothing insulation of the different body segments. In our study, this is defined on the basis of the standardised clothing used in the experimental campaigns. Details of the clothing ensemble are shown in Appendix A. However, the insulation provided by the footwear, as well as the environmental conditions and physical activity, can be adjusted by the user depending on the scenario under investigation.

Based on these inputs, JOS-3 calculates the temporal evolution of the mean skin temperature, which serves as input for the LSTM network. The network then predicts the corresponding temperature curve of the big toe and estimates the time at which the critical threshold is reached, which is a quantitative measure of the cold risk.

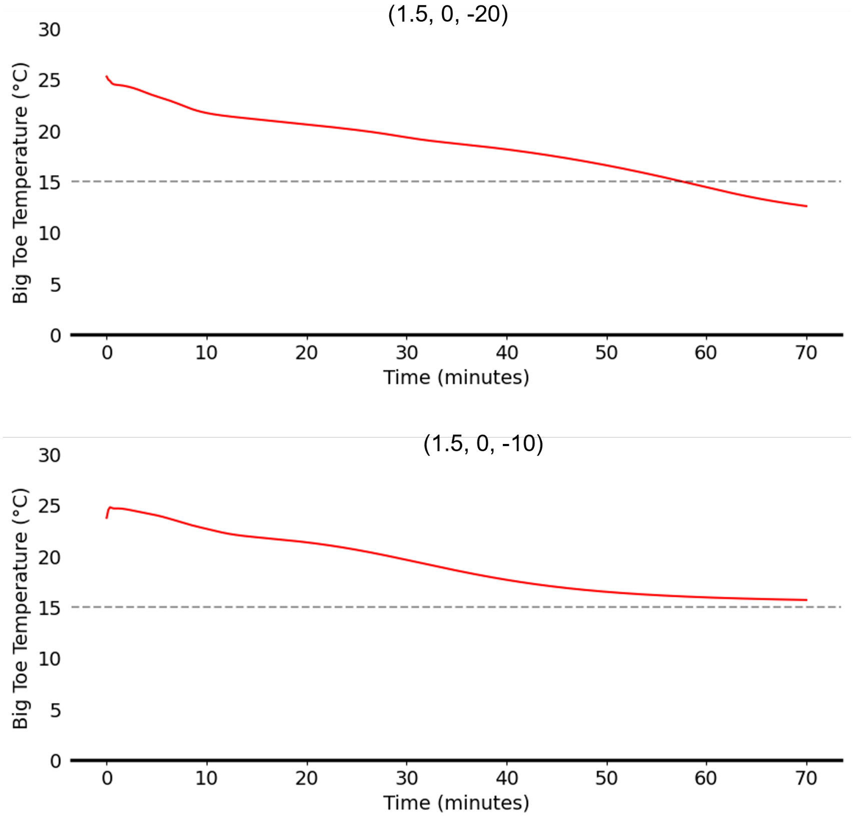

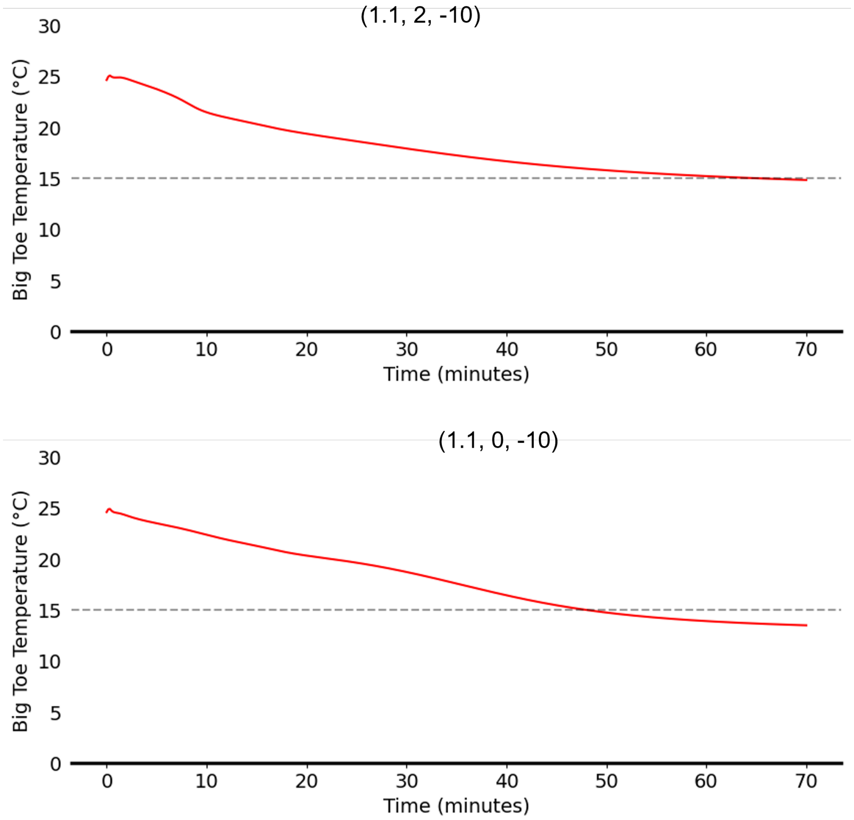

Fig. 4.7 Representative cases illustrating the LSTM model predictions under varying conditions. (a) Stillness, high boot insulation, severe temperature; time to threshold = 57 min. (b) Same insulation and activity, but ambient temperature -10°C; trajectory does not reach the threshold. (c) High activity, lower boot insulation (R_{cT} = 1.1) at -10°C; time to threshold = 64 min. (d) Stillness, low boot insulation at -10°C; time to threshold = 47 min. These examples highlight both the consistency of the model with respect to the weights of the input labels and its sensitivity to changes in environmental and physiological conditions.

The four cases shown in Figure 4.7 illustrate the ability of the LSTM model to capture both the consistency of the labelling weights and its sensitivity to different conditions. In the first case (Figure 4.7a), where the subject is at rest, the boots are well insulated and the ambient temperature severe, the model predicts a time to reach threshold of 57 minutes, which is in line with physical expectations. In the second image (Figure 4.7b), the same insulation and activity conditions prevail, but at a higher temperature of -10°C; here the curve does not reach the threshold, showing the model's ability to adapt to more extreme environmental conditions. In the third scenario (Figure 4.7c) with high activity and reduced boot insulation (R_{cT} = 1.1) at -10°C, the time to threshold increases to 64 minutes, indicating that physical activity can partially compensate for lower insulation. Finally, the fourth case

(Figure 4.7d), again at -10°C with the subject at rest and low boot insulation, shows a reduced time to threshold of 47 minutes, confirming the influence of insulation on toe cooling. Overall, these examples illustrate both the predictive consistency of the model with respect to subject and boot characteristics and its sensitivity to variations in temperature, insulation, and activity, providing robust support for the assessment of peripheral cooling risk.

To supplement the evaluation of LSTM performance, a feature saliency analysis was performed. This involved calculating the absolute value of the gradient of the predicted big toe temperature in relation to each input feature. In other words, this measure indicates how sensitive the model's prediction is to small changes in each feature, regardless of the direction of change. Figure 4.8 shows the mean absolute gradient across all time steps and all test conditions, with the error bars representing the standard deviation between conditions.

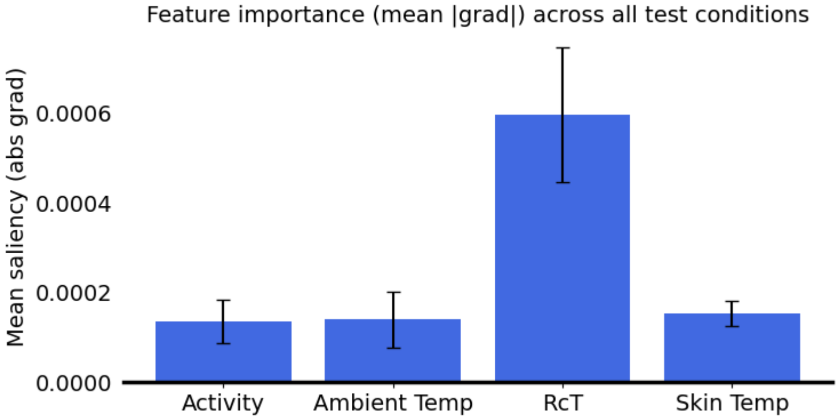

Fig. 4.8 Mean of the absolute gradients of the LSTM prediction estimated with respect to each input feature. The error bars represent the standard deviation across all test conditions.

From the plot, it can be observed that the "R_{cT}" parameter has the highest mean saliency, but also the greatest variability between conditions. The feature "skin temperature" shows a similar mean saliency but with much narrower error bars, indicating a more consistent influence across conditions. "Ambient temperature" and "activity level" have comparable saliency values, with the activity trait showing slightly less variability than ambient temperature.

Overall, this analysis highlights that the LSTM relies heavily on R_{cT}, while the consistency of skin temperature across conditions makes it a stable predictor and ambient temperature and activity have an additional, moderate influence.

4.6 Conclusions

This chapter presented the development and validation of a predictive method for big toe temperature during cold exposure, integrating data-driven and physiological modelling approaches. The work highlighted several key findings.

Firstly, the comparison between SARIMAX and LSTM models showed the limitations of classical statistical methods when applied to non-linear and transient physiological processes. While SARIMAX was able to capture some general trends, it relied heavily on mean skin temperature as an exogenous driver and could not represent inter-individual variability or transient cooling dynamics. In contrast, the LSTM model showed a higher ability to reproduce complex temporal dependencies and predict threshold events with improved accuracy, precision, and recall.

SARIMAX was intended to provide a structured and interpretable baseline against which the added value of data-driven modelling could be assessed. Its relatively low complexity, explicit treatment of temporal dependencies, and suitability for small datasets make it a common reference model in time-series forecasting. In the present work, the introduction of seasonality does not reflect an underlying physical periodicity, but serves as a mathematical proxy to encode the repeated structure of the experimental protocol and inter-individual variability within a fixed observation window.

While the LSTM model demonstrates superior predictive performance across all tested conditions, its applicability is inherently constrained by the size and composition of the available dataset. In particular, class imbalance and the limited occurrence of complex thermoregulatory events, such as cold-induced vasodilation, restrict the model's ability to fully learn and generalise these patterns. These limitations are due primarily to data availability rather than model capacity, and highlight the need for larger and more diverse datasets to support robust training of deep learning architectures. For this reason, the proposed LSTM framework should be regarded as a predictive support tool rather than a standalone decision model.

Future developments should focus on expanding the dataset to include a wider range of physiological responses and environmental conditions, improving the representation of rare events, and integrating uncertainty-aware approaches such as probabilistic neural networks or hybrid physics-informed models. These extensions would enhance both the robustness and interpretability of the digital twin concept proposed in this thesis.

Secondly, detailed evaluation of the LSTM predictions revealed that the network performs best when cooling follows a monotonic trend, while deviations occur when irregularities or sudden changes influence the temperature decrease. Importantly, even when the threshold crossing was not correctly detected, the model often reproduced physiologically plausible trajectories, confirming its robustness in capturing the dynamics of thermoregulation. This was enabled by the availability of experimental data, which also took into account how local body temperatures behaved under different environmental and footwear insulation. Consequently, the developed surrogate model for predicting the Duration of Safe Exposure is reliable enough to address the gap in thermoregulation description present in full-body-scale models such as JOS-3.

Finally, integration with the JOS-3 thermoregulation model enabled the generalisation of predictions to new environmental and activity conditions, as well as footwear insulation. By using JOS-3 outputs as input features, the system can estimate toe temperature and the associated cold exposure limit duration without the need for subject-specific measurements. This makes the approach both flexible and applicable to practical scenarios, such as evaluating footwear and defining cold risk indices for users.

Overall, the results highlight the potential of combining thermophysiological modelling and deep learning to bridge the gap between experimental data and practical applications in the field of footwear comfort and safety. This integrated approach provides a more comprehensive picture of peripheral cooling risk and supports both product design and prevention strategies in cold environments.

References

Acikmese, Y., Alptekin, S.E., 2019. Prediction of stress levels with lstm and passive mobile sensors. Procedia Computer Science 159, 658–667. URL: https://doi.org/10.1016/j.procs.2019.09.085.

Bianca, E., Boccardo, G., Buffo, A., Vanni, M., Ferri, A., 2025. A multimodal approach to predicting toe temperature: Experimental, cfd, in: Accessibility, Assistive Technology and Digital Environments, pp. 201–210. doi:`10.54941/ahfe1006027`.

Bianca, E., Dotti, F., Orrico, F., Ferri, A., 2024. Thermoregulation of feet in cold environments: A study on alpinism. Applied Ergonomics 116, 104205.

Box, G.E.P., Jenkins, G.M., Reinsel, G.C., Ljung, G.M., 2015. Time Series Analysis: Forecasting and Control. John Wiley & Sons.

De Saa, E., Ranathunga, L., 2020. Comparison between arima and deep learning models for temperature forecasting. arXiv preprint arXiv:2011.04452 URL: https://doi.org/10.48550/arXiv.2011.04452, doi:`10.48550/arXiv.2011.04452`. submitted on 9 Nov 2020.

Elshewey, A.M., Shams, M.Y., Elhady, A.M., Shohieb, S.M., Abdelhamid, A.A., Ibrahim, A., Tarek, Z., 2023. A novel wd-sarimax model for temperature forecasting using daily delhi climate dataset. Sustainability 15, 757. URL: https://doi.org/10.3390/su15010757, doi:`10.3390/su15010757`.

Guan, N., Guan, Y., Sun, x., 2019. Global temperature forecast based on arima model, in: 4th International Conference on Communication and Information Systems (ICCIS), Wuhan, China. pp. 108–112. URL: https://doi.org/10.1109/ICCIS49662.2019.00026, doi:`10.1109/ICCIS49662.2019.00026`.

Han, X., Zhang, L., Xu, S., Li, Y., 2024. Forecasting human core and skin temperatures: A long-term series approach. Big Data and Cognitive Computing 8, 197. URL: https://doi.org/10.3390/bdcc8120197.

Hardy, J.D., 1972. Models of temperature regulation-a review. Essays on temperature regulation. , 163–186.

Jamieson, K., Talwalkar, A., 2016. Non-stochastic best arm identification and hyperparameter optimization, in: Artificial Intelligence and Statistics, pp. 240–248.

Karim, F., Majumdar, S., Darabi, H., Chen, S., 2017. Lstm fully convolutional networks for time series classification. IEEE Access 6, 1662–1669.

Kemeth, F.P., Bertalan, T., Evangelou, N., Cui, T., Malani, S., Kevrekidis, I.G., 2021. Initializing lstm internal states via manifold learning. Journal of Nonlinear Science 31. URL: https://doi.org/10.48550/arXiv.2104.13101, doi:`10.48550/arXiv.2104.13101`.

Kim, T., Jang, M., Jeong, H.C., Joo, S., 2022. Short-term residential load forecasting using 2-step sarimax. Journal of Electrical Engineering & Technology 17, 751–758. URL: https://doi-org.ezproxy.biblio.polito.it/10.1007/s42835-021-00917-z, doi:`10.1007/s42835-021-00917-z`.

Lai, Y., Dzombak, D.A., 2020. Use of the autoregressive integrated moving average (arima) model to forecast near-term regional temperature and precipitation. Weather and Forecasting 35, 959–976. URL: https://doi.org/10.1175/WAF-D-19-0158.1, doi:`10.1175/WAF-D-19-0158.1`.

Li, L., Jamieson, K., DeSalvo, G., Rostamizadeh, A., Talwalkar, A., 2018. Hyperband: A novel bandit-based approach to hyperparameter optimization. Journal of Machine Learning Research 18, 1–52.

Liang, Z., Wang, X., Li, H., Li, J., 2021. Body temperature prediction with recurrent neural network and its variants, in: 2021 11th International Conference on Intelligent Control and Information Processing (ICICIP), IEEE. pp. 281–286. URL: https://doi.org/10.1109/ICICIP53737.20.

Lipton, Z., Berkowitz, J., Elkan, C., 2015. A critical review of recurrent neural networks for sequence learning URL: https://doi.org/10.48550/arXiv.1506.00019.

Lopardo, G., 2011. Un modello matematico di termoregolazione del corpo umano .

Mienye, I., Swart, T., Obaido, G., 2024. Recurrent neural networks: A comprehensive review of architectures, variants, and applications. Information 15, 517. URL: https://doi.org/10.3390/info15090517.

Nketiah, E.A., Agyeman, M.G., Oppong, A.K., 2023. Recurrent neural network modeling of multivariate time series and its application in temperature forecasting. PLoS ONE 18, e0285713. URL: https://doi.org/10.1371/journal.pone.0285713.

Rida, M., Darwish, A., Duarte, F., Haddad, R., 2023. Toward contactless human thermal monitoring: A framework for machine learning-based human thermo-physiology modeling augmented with computer vision. Building and Environment 245, 110850. URL: https://doi.org/10.1016/j.buildenv.2023.110850.

Takahashi, Y., Nomoto, A., Yoda, S., Hisayama, R., Ogata, M., Ozeki, Y., ichi Tanabe, S., 2021. Thermoregulation model jos-3 with new open source code. Energy and Buildings 231, 110575.

Tanwar, R., Kumar, R., Singh, M., Tyagi, G., 2022. Cnn-lstm based stress recognition using wearables, in: KGSWC Workshops.

Chapter 5

Conclusions

This thesis proposed an alternative, integrated framework for evaluating the thermal efficiency of cold-protective footwear, combining experimental testing, physics-based modelling, and data-driven approaches. Rather than focusing solely on static insulation metrics, the methodology aimed to capture the coupled interaction between material properties, environmental conditions, and user-related factors. This perspective enabled a more comprehensive assessment of thermal performance, particularly under extreme and transient conditions, but also highlighted the inherent complexity of linking physical measurements to perceived thermal comfort.

The experimental investigations provided original datasets on local thermal responses of the human foot in cold environments, including toe temperature and metabolic rate measurements that are rarely available in the literature for such conditions. These data contributed to improving the understanding of thermoregulatory behaviour in the extremities and supported the identification of local comfort and safety thresholds. However, the controlled nature of the experimental protocol and the limited population sample constrained the generalisability of the findings. Therefore, the experimental outcomes should be interpreted as representative of specific physiological and environmental scenarios rather than as universal descriptors of human response to cold exposure.

The development of a numerical counterpart to the thermal manikin test defined in ISO 15831 represents a significant methodological contribution of this work. By reproducing standardised test conditions in a virtual environment, the proposed digital twin offers a flexible and cost-effective tool for comparative assessment of footwear insulation during the early design stages. However, this approach necessarily relies on simplified representations of geometry, material behaviour, and boundary conditions. While these assumptions are appropriate for trend analysis and relative comparison between designs, they limit the accuracy of absolute predictions and highlight the need for careful calibration and validation when extending the model beyond standardised configurations.

The integration of data-driven models, particularly Long Short-Term Memory networks, demonstrated the potential of machine learning to link measurable physical parameters with local thermoregulatory outcomes. The LSTM-based framework enabled the prediction of toe temperature trends under different activities and environmental conditions and surpassed classical statistical models in this task. Nevertheless, the predictive capability of the model remains strongly dependent on the availability, balance, and diversity of experimental data. Rare and complex thermoregulatory events, such as cold-induced vasodilation, were insufficiently represented in the dataset, limiting the model's ability to learn these behaviours. Furthermore, the limited interpretability of the neural network and the absence of uncertainty quantification currently restrict its applicability in safety-critical or regulatory contexts.

The coupling of the data-driven model with a thermoregulation model (JOS-3) partially mitigated the dependence on extensive human testing by enabling the generation of synthetic physiological inputs. While this hybrid approach improves the practical usability of the framework during the prototyping phase, it also introduces an additional modelling layer whose assumptions and uncertainties propagate through the prediction chain. Consequently, the proposed digital twin should be regarded as a decision-support tool rather than a definitive predictor of individual thermal comfort or risk.

Looking ahead, several points for further development emerge from this work. A key direction involves the adoption of multiscale modelling strategies, in which localised models of footwear components and body segments are progressively integrated into a coherent system-level representation. Expanding the experimental database to include more diverse populations, environmental conditions, and material configurations would be essential to strengthen both physics-based and data-driven components. Finally, the integration of uncertainty-aware modelling techniques and physics-informed machine learning could enhance robustness, interpretability, and confidence in predictions, moving the proposed framework closer to practical application in design optimisation and safety assessment.

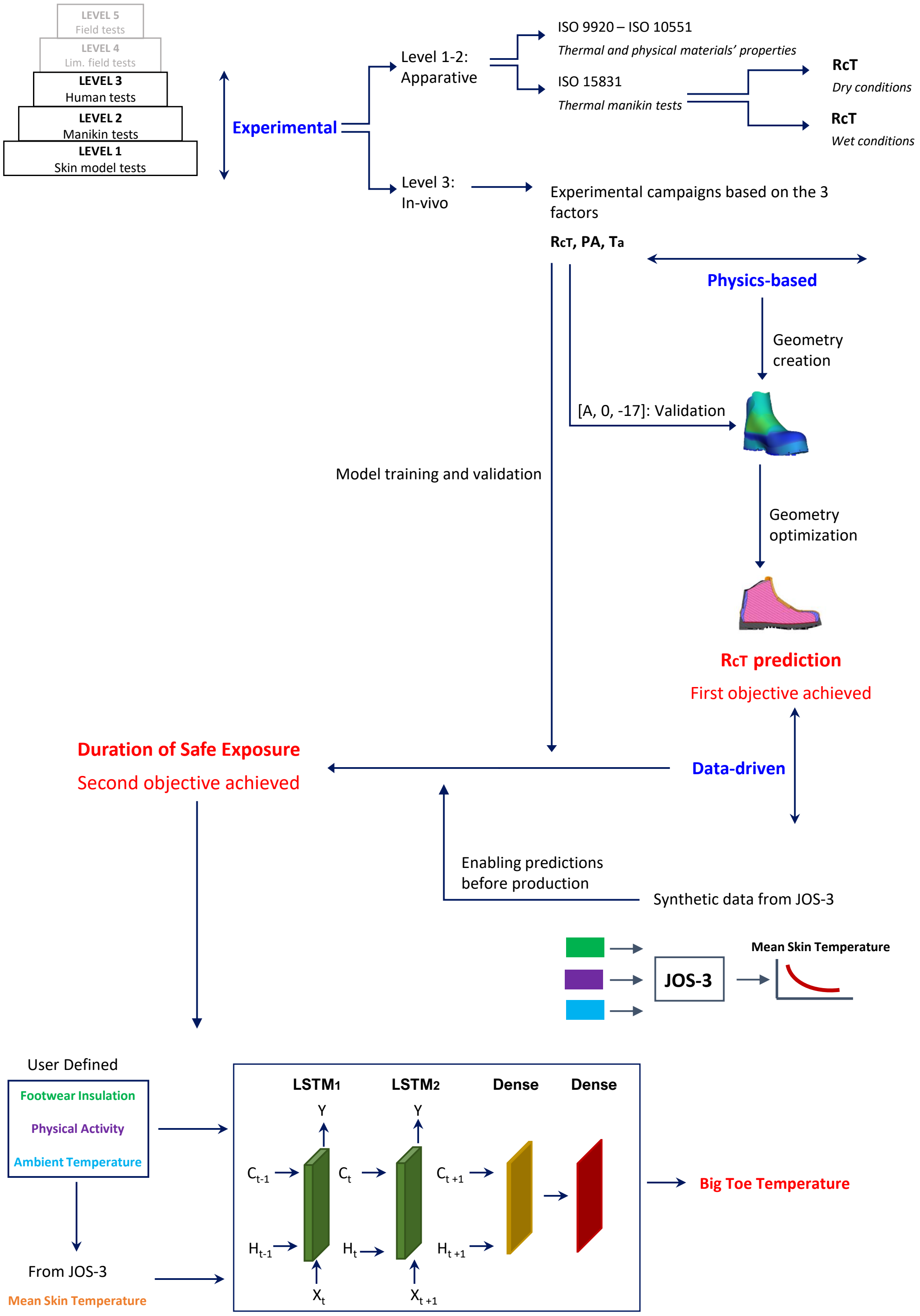

Fig. 5.1 Overview of the thesis workflow, integrating experimental, physics-based, and data-driven approaches from material- and skin-level testing to numerical modelling and digital twin development.

Appendix A

Clothing Ensemble

This Appendix specifies the garment properties and insulation values for the body areas defined in ISO 15831:2004 [1]. Test procedure are specified in Section 2.2
As defined in Section 2.1, the clothing ensemble has been kept fixed in the tests to reduce variability and better assess the effects of exogenous factors on human thermoregulation.

---

[1] ISO 15831:2004 Clothing. Physiological effects. Measurement of thermal insulation by means of a thermal manikin.

Garment	**Use**	R_{cT} **[m^2·K/W]**
	1st layer (breathability and insulation)	Chest: 1.69 Back: 2.37 Shoulders: 1.66 Arm: 1.51
	2nd layer (insulation)	
	3rd layer (wind protection)	

Table A.1 Garment upper layers used in the experimental campaigns with corresponding R_{cT}.

Garment	**Use**	R_{cT} **[m^2·K/W]**
	1st layer (breathability and insulation)	Pelvis: 2.32 Thigh: 0.96 Leg: 1.16
	2nd layer (insulation)	
	3rd layer (wind protection)	

Table A.2 Garment bottom layers used in the experimental campaigns with corresponding R_{cT}.

Garment	**Use**	R_{cT} **[m^2·K/W]**
	Gloves	Hand: 1.28 Neck: 0.35 Head: 0.66
	Buff	
	Beanie	

Table A.3 Garment accessories used in the experimental campaigns with corresponding R_{cT}.

Model	**Use**	R_{cT} **[m^2·K/W]**
	Model A - Technical ice and mixed winter mountaineering	0.202
	Model B - Extreme alpinism and ice-falls	0.208
	Model C - Extreme alpinism for heights up to 8000 m	0.446
	Model D - Short or day-hike trekking	0.193
	Model E - Long trekking excursion	0.195

Table A.4 Boot models used in the experimental campaigns with corresponding R_{cT}.

Appendix B

C.O.L.D.: Cold-weather Outwear Level Determiner

B.1 Objective of C.O.L.D.

`C.O.L.D.`[1] was developed to make the product engineering studies carried out during the three years of the PhD accessible to industrial partners. In particular, it is designed as a single graphical interface that integrates several tools.

Key features of `C.O.L.D.` include allowing the user to access **ANSYS** simulations directly from Python, using a pre-configured case model that can be modified in terms of the boundary conditions and composition of the footwear. In addition, the interface provides access to the neural network **LSTM**, developed for the prediction of big toe temperature.

These tools can be used either independently or synergistically, allowing the user to compare the results of different approaches or combine them to gain a more comprehensive understanding of the thermal performance of footwear.

B.2 Architecture and Technologies

`C.O.L.D.` is implemented in Python 3.8 (tested with version 3.10) and relies on several libraries organised by function.

---

[1] Logo design by Soumia Mahdoul - email: soumia.mahdoul@gmail.com.

Graphical interface and visualisation: the graphical user interface is created with `Tkinter` and `CustomTkinter`, chosen for their flexibility and aesthetic quality. `PIL` is used for image processing, while `Matplotlib` provides colour mapping and plotting functionalities. Threading is used to enable asynchronous GUI updates during calculations.

File management and system utilities: modules such as `os`, `time`, `subprocess`, and `config` handle the loading/saving of configurations and the execution of external scripts. Regular expressions (`re`) are used to parse file names and paths.

Data processing: `Pandas` and `NumPy` manage tabular and numerical data, while `joblib` is used to save and load pre-processed objects, such as scalers for the LSTM.

Neural network integration: the LSTM is implemented with `Keras` and `TensorFlow` and enables real-time prediction of big toe temperature based on skin temperature inputs.

External simulation tools: ANSYS Fluent is called directly from Python via the `pyfluent` API, with pre-configured case models whose boundary conditions and material compositions can be changed. The `jos3` module for predicting the mean skin temperature is also integrated.

A schematic overview of the `C.O.L.D.` architecture is shown in Figure B.1, and shows how input data, processing modules, and output visualisation are connected.

B.3 Main Functionalities

`C.O.L.D.` offers two operating modes: `Manual Mode` and `Automatic Mode`, each designed to facilitate different aspects of footwear thermal analysis.

B.3.1 Manual Mode

In `Manual Mode`, the user can enter the boundary conditions of interest to evaluate the *Duration of Safe Exposure* for a specific shoe model with a known insulation value (R_{cT}). Specifically, the user enters the ambient temperature, the level of physical activity (0 for rest, 1 for light exertion, 2 for medium/demanding activity) and the R_{cT} of the selected boot.

These inputs are passed to the JOS-3 thermoregulation model, which adjusts its internal parameters according to the user-defined conditions and predicts the mean

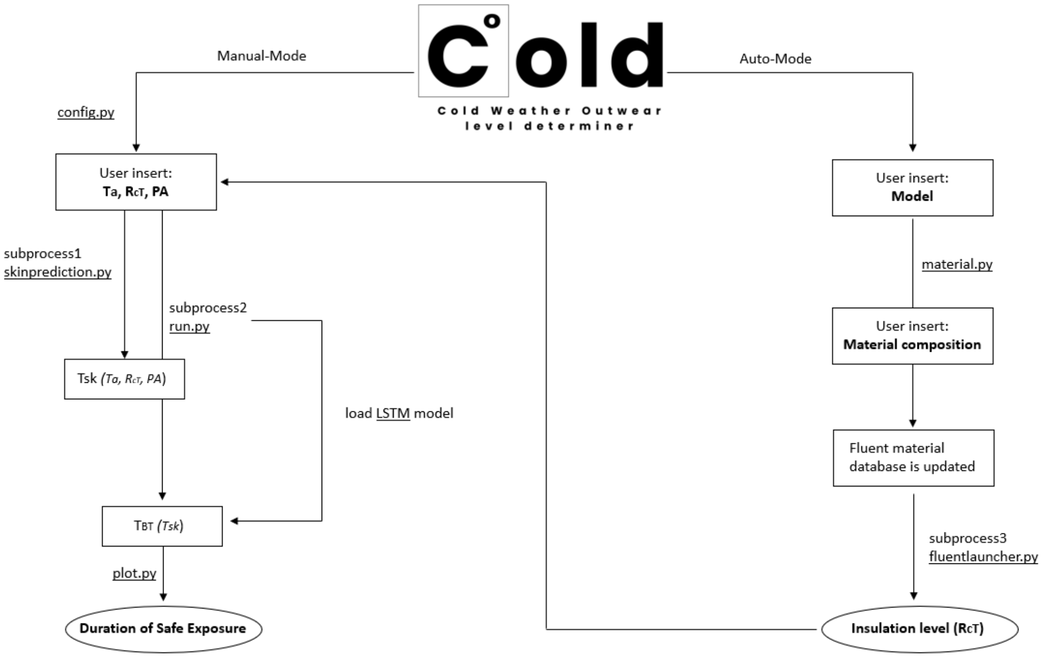

Fig. B.1 Schematic overview of the C.O.L.D. interface architecture, showing the flow of data from input through processing modules, including ANSYS Fluent and the LSTM neural network, to output visualization.

skin temperature. A subsequent Python sub-process reads the generated time series and feeds it into the LSTM neural network described in Section 4.5.1. The network then predicts the big toe temperature over a 70-minute interval, and specifies both the time to reach certain thresholds and the intervals corresponding to comfort and discomfort (defined as 25°C and 20°C at the big toe, respectively). The time required to reach 15°C is the *Duration of Safe Exposure*.

B.3.2 Automatic Mode

In `Automatic Mode`, the user first selects the boot model to be analysed and the corresponding STL file is loaded. The interface allows the configuration of the material composition of each boot region via a library containing all relevant thermal properties required by ANSYS Fluent.

Once the configuration of the prototype is complete, the application can start the simulation, which corresponds to the digital twin of the ISO 15831:2004 thermal manikin test. The simulation generates two primary outputs:

1. A pie chart dividing the boot into three main regions (top, bottom and side) and showing the percentage of the predominant heat transfer mechanism in each region (e.g. convective, conductive).
2. The overall R_{cT} value of the analysed prototype.

At this point, the simulation can either be stopped or the calculated R_{cT} can be automatically transferred to `Manual Mode` to start a second simulation allowing the user to observe the predicted big toe temperature curve for this specific boot configuration.

B.3.3 Additional Features

Both modes include interactive visualisation tools, such as graphs of temperature trends, comfort/comfort intervals, and comparisons between different scenarios. The user can export charts and reports for further analysis or documentation purposes.

B.4 User Interface Overview

The following figures illustrate the main components of the `C.O.L.D.` interface. At startup, a short disclaimer (Figure B.2) provides information on how to use the application. It also informs the user that an ANSYS Fluent license is required for `Automatic Mode`, although `Manual Mode` can also be used without a license.

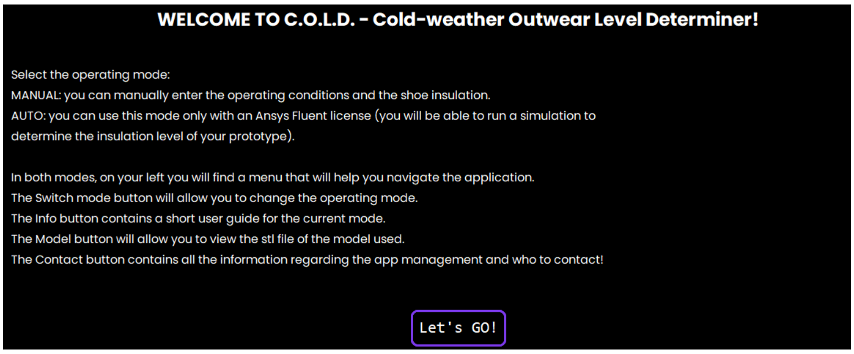

WELCOME TO C.O.L.D. - Cold-weather Outwear Level Determiner!

Select the operating mode:
MANUAL: you can manually enter the operating conditions and the shoe insulation.
AUTO: you can use this mode only with an Ansys Fluent license (you will be able to run a simulation to determine the insulation level of your prototype).

In both modes, on your left you will find a menu that will help you navigate the application.
The Switch mode button will allow you to change the operating mode.
The Info button contains a short user guide for the current mode.
The Model button will allow you to view the stl file of the model used.
The Contact button contains all the information regarding the app management and who to contact!

Fig. B.2 Initial guide that is displayed when starting `C.O.L.D.`, highlighting licensing requirements and navigation instructions

Once the guide has been accepted, the interface is ready for use (Figure B.3). The user can choose between `Manual` and `Automatic Mode`, and it is possible to switch between modes during operation without restarting the application.

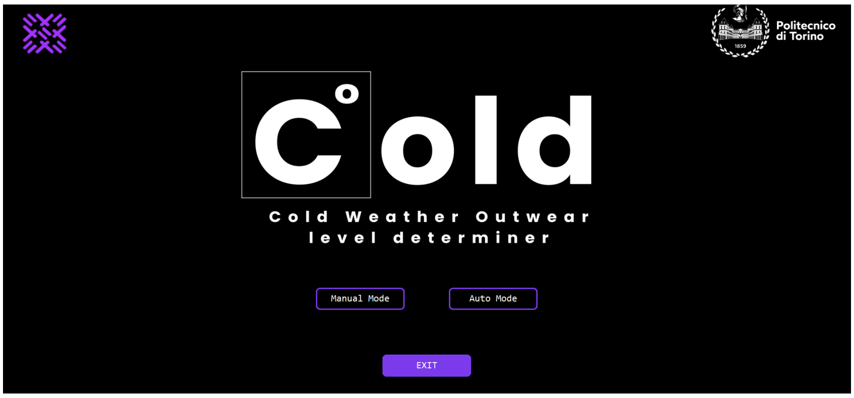

Fig. B.3 Main user interface window after the initial instructions, showing the mode selection options and the navigation menu

The menu on the left-hand side (Figure B.4) provides access to important information about the application, contact details, and the option to visualise 3D boot models using the system's standard 3D viewer.

B.4.1 Manual Mode

In `Manuel Mode`, the user inputs the boundary conditions to be analysed (Figure B.5) and starts the simulation. The results vary according to the selected conditions (Figure B.6) and indicate the time spent in the different zones: Comfort, Discomfort, and Threshold. The time it takes for the curve to reach the threshold zone represents the *Duration of Safe Exposure*.

B.4.2 Automatic Mode

In `Automatic Mode`, the user can create a custom boot prototype by selecting the STL file of the model and configuring the material composition for each area (Figure B.7). Once confirmed, the application automatically starts the simulation and returns the overall value R_{cT} of the prototype. Optionally, the user can create a pie chart showing the contribution of the different heat transport mechanisms in each boot region (Figure B.8).

Fig. B.4 Left-hand side of the user interface shows utilities, contact information and options for displaying 3D models

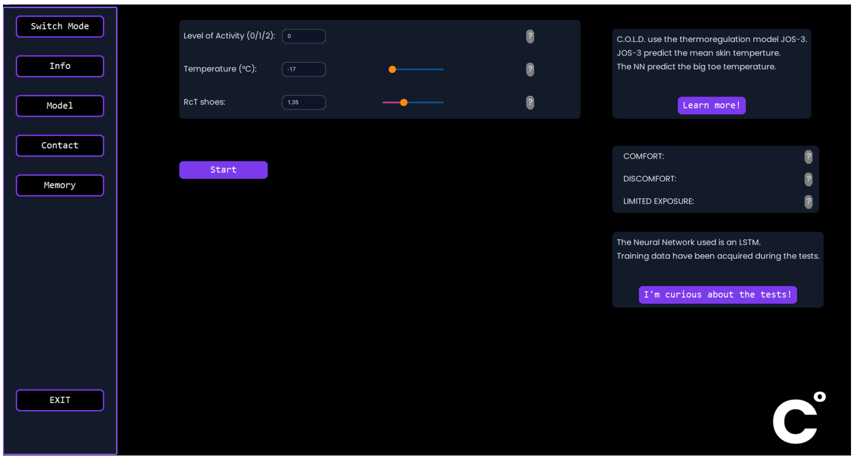

Level of Activity (0/1/2): 0

Temperature (°C): -17

RcT shoes: 1.35

C.O.L.D. use the thermoregulation model JOS-3.
JOS-3 predict the mean skin temperture.
The NN predict the big toe temperature.

COMFORT:
DISCOMFORT:
LIMITED EXPOSURE:

The Neural Network used is an LSTM.
Training data have been acquired during the tests.

Fig. B.5 Input field for manual Mode, where the user sets the ambient temperature, activity level and boot insulation.

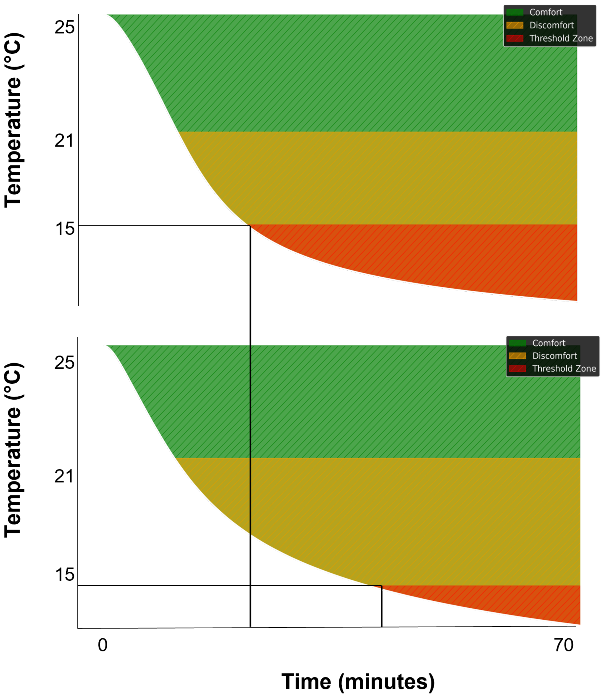

Fig. B.6 Example of results generated in Manual Mode illustrating the comfort, discomfort and threshold ranges over time

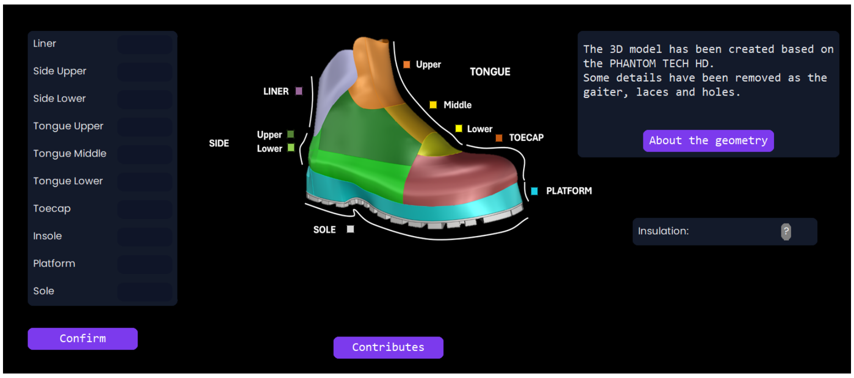

The 3D model has been created based on the PHANTOM TECH HD.
Some details have been removed as the gaiter, laces and holes.

Fig. B.7 Automatic Mode menu for assembling a boot prototype, selection of materials for each region

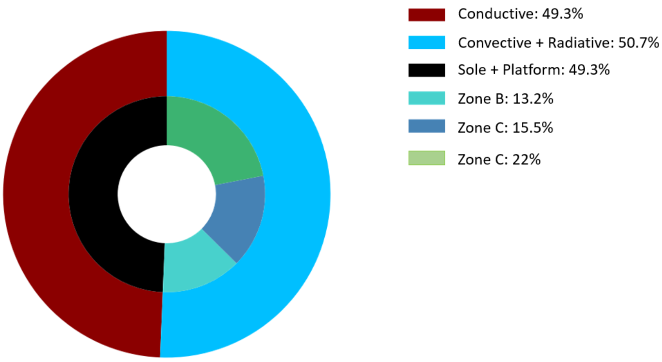

Fig. B.8 Pie chart showing the contribution of convective, conductive, and other heat transport mechanisms in each region of the boot.